Starburst Energy Feedback Seen through HCO$^+$/HOC$^+$ Emission in NGC 253 from ALCHEMI

Nanase Harada[1,2,3] , Sergio Martín[4,5] , Jeffrey G. Mangum[6] , Kazushi Sakamoto[2] , Sebastien Muller[7] ,
Kunihiko Tanaka[8] , Kouichiro Nakanishi[1,3] , Rubén Herrero-Illana[9,10] , Yuki Yoshimura[11] , Stefanie Mühle[12] ,
Rebeca Aladro[13] , Laura Colzi[14,15] , Víctor M. Rivilla[14,15] , Susanne Aalto[7] , Erica Behrens[16] , Christian Henkel[13,17,18] ,
Jonathan Holdship[19,20] , P. K. Humire[13], David S. Meier[21,22] , Yuri Nishimura[11,23] , Paul P. van der Werf[19] , and
Serena Viti[19,20]

[1] National Astronomical Observatory of Japan, 2-21-1 Osawa, Mitaka, Tokyo 181-8588, Japan; nanase.harada@nao.ac.jp
[2] Institute of Astronomy and Astrophysics, Academia Sinica, 11F of AS/NTU Astronomy-Mathematics Building, No.1, Sec. 4, Roosevelt Rd, Taipei 10617, Taiwan
[3] Department of Astronomy, School of Science, The Graduate University for Advanced Studies (SOKENDAI), 2-21-1 Osawa, Mitaka, Tokyo, 181-1855, Japan
[4] European Southern Observatory, Alonso de Córdova, 3107, Vitacura, Santiago 763-0355, Chile
[5] Joint ALMA Observatory, Alonso de Córdova, 3107, Vitacura, Santiago 763-0355, Chile
[6] National Radio Astronomy Observatory, 520 Edgemont Road, Charlottesville, VA 22903-2475, USA
[7] Department of Space, Earth and Environment, Chalmers University of Technology, Onsala Space Observatory, SE-439 92 Onsala, Sweden
[8] Department of Physics, Faculty of Science and Technology, Keio University, 3-14-1 Hiyoshi, Yokohama, Kanagawa 223–8522, Japan
[9] European Southern Observatory, Alonso de Córdova 3107, Vitacura, Casilla 19001, Santiago de Chile, Chile
[10] Institute of Space Sciences (ICE, CSIC), Campus UAB, Carrer de Magrans, E-08193 Barcelona, Spain
[11] Institute of Astronomy, Graduate School of Science, The University of Tokyo, 2-21-1 Osawa, Mitaka, Tokyo 181-0015, Japan
[12] Argelander-Institut für Astronomie, Universität Bonn, Auf dem Hügel 71, D-53121 Bonn, Germany
[13] Max-Planck-Institut für Radioastronomie, Auf dem Hügel 69, D-53121 Bonn, Germany
[14] Centro de Astrobiología (CSIC-INTA), Ctra. de Ajalvir Km. 4, Torrejón de Ardoz, E-28850 Madrid, Spain
[15] INAF-Osservatorio Astrofisico di Arcetri, Largo Enrico Fermi 5, I-50125, Florence, Italy
[16] Department of Astronomy, University of Virginia, P. O. Box 400325, 530 McCormick Road, Charlottesville, VA 22904-4325, USA
[17] Astronomy Department, Faculty of Science, King Abdulaziz University, P. O. Box 80203, Jeddah 21589, Saudi Arabia
[18] Xinjiang Astronomical Observatory, Chinese Academy of Sciences, Urumqi 830011, People's Republic of China
[19] Leiden Observatory, Leiden University, P.O. Box 9513, NL-2300 RA Leiden, The Netherlands
[20] Department of Physics and Astronomy, University College London, Gower Street, London WC1E 6BT, UK
[21] New Mexico Institute of Mining and Technology, 801 Leroy Place, Socorro, NM 87801, USA
[22] National Radio Astronomy Observatory, P.O. Box O, 1003 Lopezville Road, Socorro, NM 87801, USA
[23] ALMA Project, National Astronomical Observatory of Japan, 2-21-1, Osawa, Mitaka, Tokyo 181-8588, Japan

Abstract

Molecular abundances are sensitive to the UV photon flux and cosmic-ray ionization rate. In starburst environments, the effects of high-energy photons and particles are expected to be stronger. We examine these astrochemical signatures through multiple transitions of HCO$^+$ and its metastable isomer HOC$^+$ in the center of the starburst galaxy NGC 253 using data from the Atacama Large Millimeter/submillimeter Array large program ALMA Comprehensive High-resolution Extragalactic Molecular inventory. The distribution of the HOC$^+$(1−0) integrated intensity shows its association with "superbubbles," cavities created either by supernovae or expanding H II regions. The observed HCO$^+$/HOC$^+$ abundance ratios are ∼10–150, and the fractional abundance of HOC$^+$ relative to H$_2$ is ∼1.5×10^{-11}–6×10^{-10}, which implies that the HOC$^+$ abundance in the center of NGC 253 is significantly higher than in quiescent spiral arm dark clouds in the Galaxy and the Galactic center clouds. Comparison with chemical models implies either an interstellar radiation field of $G_0 \gtrsim 10^3$ if the maximum visual extinction is $\gtrsim 5$, or a cosmic-ray ionization rate of $\zeta \gtrsim 10^{-14}$ s^{-1} (3–4 orders of magnitude higher than that within clouds in the Galactic spiral arms) to reproduce the observed results. From the difference in formation routes of HOC$^+$, we propose that a low-excitation line of HOC$^+$ traces cosmic-ray dominated regions, while high-excitation lines trace photodissociation regions. Our results suggest that the interstellar medium in the center of NGC 253 is significantly affected by energy input from UV photons and cosmic rays, sources of energy feedback.

Unified Astronomy Thesaurus concepts: Interstellar medium (847); Astrochemistry (75); Starburst galaxies (1570); Cosmic rays (329)

1. Introduction

Starburst galaxies are great laboratories to study feedback mechanisms because they possess the most vigorous star formation. Starburst activities inject vast amounts of energy into the surrounding interstellar medium (ISM; e.g., Hopkins et al. 2012; Kim et al. 2013). For example, massive stars ($M \gtrsim 8\ M_\odot$) produce large amounts of UV photons, which can heat and ionize the gas (Tielens & Hollenbach 1985). When these massive stars end their lives, they explode as supernovae producing high cosmic-ray fluxes. Another form of starburst

feedback is the injection of mechanical energy into the ISM through turbulence or shocks. These energy sources are also major components of the ISM pressure (thermal, turbulence, magnetic, and cosmic-ray pressure; Lequeux 2005), which could hinder future star formation, although it could help star formation locally. Since the molecular gas component is the fuel for future star formation, it has been the subject of numerous studies to investigate the effect of such feedback. The most direct observable effect of feedback is the imprint of the kinematic signature on the gas properties (e.g., in the form

of shocks or outflows), which has been studied with transitions of carbon monoxide or a few other transitions with relatively bright emission (e.g., Fluetsch et al. 2019). Other properties of molecular gas can be best studied with chemistry.

Astrochemistry has been widely studied in Galactic star-forming regions in order to constrain the physical properties of the molecular gas. For example, DCO^+/HCO^+ and N_2D^+/N_2H^+ abundance ratios have been used as indicators of the ionization degree that contributes to the balance between the formation and destruction rates of these species in the steady state (e.g., Caselli 2002). Astrochemical studies toward external galaxies have been conducted for decades, especially with single-dish telescopes (e.g., Henkel et al. 1988; Mauersberger & Henkel 1991; Martín et al. 2006; Aladro et al. 2015). However, the chances to explore the potential of astrochemistry in external galaxies with a higher angular resolution were only opened up quite recently due to the development of sensitive interferometers, such as the Atacama Large Millimeter/submillimeter Array (ALMA) and the NOrthern Extended Millimeter Array.[24] Since then, spatially resolved studies of astrochemistry have been proven to be possible in a few extragalactic sources (e.g., in the active galactic nucleus (AGN) hosts NGC 1068 and NGC 1097, and the starburst galaxies NGC 253, M83, and NGC 3256; e.g., Takano et al. 2014; Viti et al. 2014; Martín et al. 2015; Meier et al. 2015; Nakajima et al. 2015; Harada et al. 2018, 2019).

NGC 253 is one of the closest starburst galaxies at a distance of 3.5 Mpc (Rekola et al. 2005, $1'' = 17$ pc). It hosts a total star formation rate of $5\,M_\odot\,\mathrm{yr}^{-1}$, of which $2\,M_\odot\,\mathrm{yr}^{-1}$ is concentrated within the central few hundred parsecs (Leroy et al. 2015). This type of central structure in galactic centers is referred to as a central molecular zone (CMZ; Morris & Serabyn 1996; Sakamoto et al. 2011). Strong radio/submillimeter continuum sources suggest multiple star clusters in the CMZ (Turner & Ho 1985; Ulvestad & Antonucci 1997; Leroy et al. 2018). Super hot cores, early stages of super star clusters, are reported by Rico-Villas et al. (2020). There are multiple signs of feedback in the CMZ of NGC 253. The kinetic temperature of the molecular gas has been measured to be very high ($T \gtrsim 300$ K for 10 pc scales; Mangum et al. 2019). Bubble-like cavities in molecular gas have been found in multiple locations. These cavities are called superbubbles, indicating either expanding H II regions or hypernovae (Sakamoto et al. 2006, 2011; Bolatto et al. 2013; Krieger et al. 2019). There are also outflows observed in X-rays (Strickland et al. 2000, 2002), Hα (Westmoquette et al. 2011), and molecules (Turner 1985; Bolatto et al. 2013; Walter et al. 2017; Krieger et al. 2019; Levy et al. 2021).

The chemistry in NGC 253 has been found to be fairly rich already in single-dish observations (Martín et al. 2006; Aladro et al. 2015), and even more so in ALMA observations (Meier et al. 2015; Ando et al. 2017; Krieger et al. 2020). To further explore this rich chemistry, a large spectral scan of the central molecular zone of NGC 253 has been performed with the ALMA large program ALMA Comprehensive High-resolution Extragalactic Molecular inventory (ALCHEMI; Martín et al. 2021), covering nearly all ALMA bands from 3 to 7 (except a few frequency ranges blocked by telluric lines).

This study makes use of the ALCHEMI survey data to examine the effects of UV photons and cosmic rays through the abundances of the reactive molecular ion HOC^+. HOC^+ is the

---

[24] An important exception is work by Meier & Turner (2005), which presented spatially resolved extragalactic astrochemistry already with the Owens Valley Millimeter Array.

Table 1
Literature Values of $[HCO^+]/[HOC^+]$ and $[HOC^+]/[H_2]$

Region	$[HCO^+]/[HOC^+]$	$[HOC^+]/[H_2]$	References
Extragalactic sources			
NGC 253	30−80	$(1.7-2.4) \times 10^{-10}$	(1), (2)
M82	44−136	⋯	(3)
NGC 1068	30−80	4×10^{-9}	(4)
Mrk 231	5−10[a]	⋯	(5)
Mrk 273	5[a]	⋯	(6)
PKS1830−211	55	1.6×10^{-10}	(7)
Galactic PDRs			
Horsehead Nebula	75−200	$(0.4-0.8) \times 10^{-11}$	(8)
Orion Bar	145−180	3×10^{-11}	(9), (10)
NGC 7023	50−120	7×10^{-12}	(10)
Galactic Center clouds			
Sgr B2	337−1541	$(0.5-2.8) \times 10^{-11}$	(11)
Galactic dense clouds			
DR21 (OH)	2600	1×10^{-12}	(12)
G34.3	4000	2×10^{-13}	(12)
L134N	>4500	$<7 \times 10^{-13}$	(12)
NGC 2024	900	2×10^{-12}	(12)
Orion KL	2100	2×10^{-13}	(12)
W3 (OH)	6000	8×10^{-13}	(12)
W51M	1300	5×10^{-13}	(12)
Galactic diffuse clouds			
B0355+508	72	6.1×10^{-11}	(13)
B0415+379	117	2.6×10^{-11}	(13)
B0528+134	>30	$<1.6 \times 10^{-10}$	(13)
B1730−130	>18	$<4.3 \times 10^{-10}$	(13)
B2200+420	70	6.5×10^{-11}	(13)

Notes.
[a] Abundance ratios are derived with the assumption of optically thin media.
References. (1) Martín et al. (2009), (2) Aladro et al. (2015), (3) Fuente et al. (2008), (4) Usero et al. (2004), (5) Aalto et al. (2015), (6) Aladro et al. (2018), (7) Muller et al. (2011), (8) Goicoechea et al. (2009), (9) Goicoechea et al. (2017), (10) Fuente et al. (2003), (11) Armijos-Abendaño et al. (2020), (12) Apponi & Ziurys (1997), (13) Liszt et al. (2004).

---

metastable isomer of HCO^+ with an energy difference of 16,600 K (Defrees et al. 1984). Unlike HCO^+, which tends to be more widely distributed, HOC^+ has high fractional abundances only in regions strongly irradiated by UV photons, X-rays, or cosmic-ray particles. Therefore, the HCO^+/HOC^+ ratio varies significantly among sources (Table 1). For example, the HCO^+/HOC^+ ratio is high in quiescent dense dark clouds, with ratios $\gtrsim 1000$ (Apponi & Ziurys 1997). By contrast, the HCO^+/HOC^+ ratios are lower in photodissociation regions (PDRs). These PDRs include Galactic diffuse clouds ($HCO^+/HOC^+ = 70-120$; Liszt et al. 2004) and the Orion dense PDR ($HCO^+/HOC^+ = 145-180$; Goicoechea et al. 2017). Starburst galaxies are also expected to contain significant numbers of PDRs. Low HCO^+/HOC^+ ratios were found in the starburst galaxy M82 ($HCO^+/HOC^+ = 44-136$; Fuente et al. 2008; Aladro et al. 2015) and in single-dish observations of NGC 253 (Martín et al. 2009; Aladro et al. 2015; $HCO^+/HOC^+ = 63-80$ and 30, respectively). An HCO^+/HOC^+ ratio of 55 was also found in the $z = 0.89$ molecular absorber toward PKS1830-211 (Muller et al. 2011). In the Galactic Center clouds of the Sgr B2 region, where we expect

Table 2
Spectroscopic Properties of the Observed Transitions of HOC$^+$, HCO$^+$, and H^{13}CO$^+$, and rms Noise Values of the Corresponding Image Cubes

Species	Transition	Rest Frequency[a] (GHz)	$E_{\rm up}$[b] (K)	$A_{\rm ul}$[c] (s^{-1})	Rms (mJy beam^{-1})	Rms (mK)	$\sigma_{\rm typ}$ (K km s^{-1})
HOC$^+$	$J = 1-0$	89.487414	4.3	2.1×10^{-5}	0.20	12.	0.75
	$J = 3-2$	268.451094	25.8	7.4×10^{-4}	1.2	7.6	0.48
	$J = 4-3$	357.921987	42.9	1.8×10^{-3}	2.2	8.2	0.52
HCO$^+$	$J = 1-0$	89.1885247	4.3	4.2×10^{-5}	0.23	14.	0.87
	$J = 3-2$	267.5576259	25.7	1.5×10^{-3}	1.4	9.7	0.61
	$J = 4-3$	356.7342230	42.8	3.6×10^{-3}	2.4	9.0	0.57
H^{13}CO$^+$	$J = 1-0$	86.7542884	4.2	3.9×10^{-5}	0.12	7.9	0.50
	$J = 3-2$	260.2553390	25.0	1.3×10^{-3}	1.0	7.3	0.46
	$J = 4-3$	346.9983440	41.6	3.3×10^{-3}	2.0	8.2	0.52

Notes. Rms values of a single channel with $\Delta v = 10$ km s^{-1} are shown.
[a] Frequency taken from the CDMS (https://cdms.astro.uni-koeln.de; Müller et al. 2001, 2005).
[b] Upper level energy of the transition.
[c] $A_{\rm ul}$: Einstein coefficient of spontaneous emission.

effects of UV photons, X-rays, or cosmic rays, the HCO$^+$/HOC$^+$ ratio was found to be 300–1500 (Armijos-Abendaño et al. 2020). Model calculations show that HOC$^+$ is also enhanced by cosmic rays (Albertsson et al. 2018). It has also been suggested that HOC$^+$ can be efficiently produced in X-ray dominated regions (XDRs; Spaans & Meijerink 2007). In the central region surrounding the AGN in NGC 1068, a low ratio of HCO$^+$/HOC$^+$ = 30–80 was found, possibly due to XDRs (Usero et al. 2004). In the AGN-driven outflows of Mrk 231 and Mrk 273, very low values of the HCO$^+$/HOC$^+$(3–2) intensity ratios, ∼10, were observed by Aalto et al. (2015) and Aladro et al. (2018), respectively. A possible reason for such a low ratio is an outflow in the case of Mrk 231, as the cavity created by an outflow allows radiation or particles to travel further. There was no obvious cause in Mrk 273. We intend to compare the spatially resolved CMZ of NGC 253 with these environments in terms of the HOC$^+$ abundance in order to elucidate the starburst feedback to the ISM.

In this paper, we analyze high-resolution observations of the emission from the molecular ions HCO$^+$ and HOC$^+$ and make use of chemical models to explain the observed abundances. This paper is organized as follows. Section 2 explains the data analysis methods. We present our results from velocity-integrated intensity images in Section 3 and spectral shapes in Section 4. The derived column densities are discussed in Section 5. In Section 6, we present our chemical model calculations that are to be compared with our observations. We discuss the implications of our results in Section 7, and we summarize our work in Section 8.

2. Observations and Data Analysis

Details of the ALMA observations, data reduction procedures, and data products are presented in the survey description paper of ALCHEMI (Martín et al. 2021). Here, we summarize the details of the ALCHEMI observations relevant to this paper. The ALCHEMI spectrally scanned mosaic covers a region of $50'' \times 20''$ (850 pc × 340 pc) in spatial extent, comprising the CMZ within NGC 253. The phase center of the observations is $\alpha = 00^{\rm h}47^{\rm m}33.26^{\rm s}$, $\delta = -25°17'17''.7$ (ICRS). Data cubes are uniformly convolved to an angular resolution of $1''.6$ corresponding to 27 pc. Continuum emission was subtracted in the image plane, on a per-pixel basis, using the publicly available

software STATCONT (Sánchez-Monge et al. 2018). From the continuum-subtracted cubes, we extracted spectral channels covering a velocity range of ±500 km s^{-1} centered on our transitions of interest to create individual spectral transition cubes with a spectral resolution of $\Delta v = 10$ km s^{-1}. The primary beam correction was applied to these cubes as a part of the ALCHEMI imaging process (Martín et al. 2021). To obtain as high signal-to-noise ratios (S/Ns) as possible and to prevent neighboring transitions close in frequency from contaminating our velocity-integrated images, we masked regions of line cubes on a per-channel basis where emission is not expected, based on spectral line cubes of CO and HCN. There reference data cubes were generated with no primary beam correction, using the same grid with the same pixel coordinates and channel velocities. Then, we smoothed them to twice coarser angular resolution, and we masked out the regions without either a 5σ detection in CO(1−0) or a 2σ detection in HCN(1−0). Although a mask using CO(1−0) should be sufficient, HCN(1−0) was used because there is a certain region in the cube where HCN(1−0) emission had a higher S/N than CO(1−0). This mask was applied to the primary beam corrected line cubes of molecular transitions that are presented in this paper (HCO$^+$, H^{13}CO$^+$, and HOC$^+$). Although 5σ used for the mask from CO(1−0) seems rather high for a cutoff if we are applying it to transitions with a similar intensity as CO(1−0), the transitions we analyze in this paper have a brightness temperature at least a factor of several lower than CO(1−0), and the use of a high cutoff in CO should not lead to significant amounts of missing HOC$^+$ and HCO$^+$ emission in our analysis. This was confirmed by a visual inspection comparing masked and unmasked HCO$^+$ and HOC$^+$ cubes. This procedure is different from the commonly used approach where 2 to 3σ cutoff is determined from the transition of which the image is made. We employ the above approach so that the low-level emission of species with weak emission can effectively be collected and neighboring lines can be excluded from image cubes. This approach should not create any bias because the CO(1−0) transition is much more extended and stronger than HCO$^+$, H^{13}CO$^+$, and HOC$^+$. The rms values per spectral channel of the transitions used in this article are listed in Table 2.
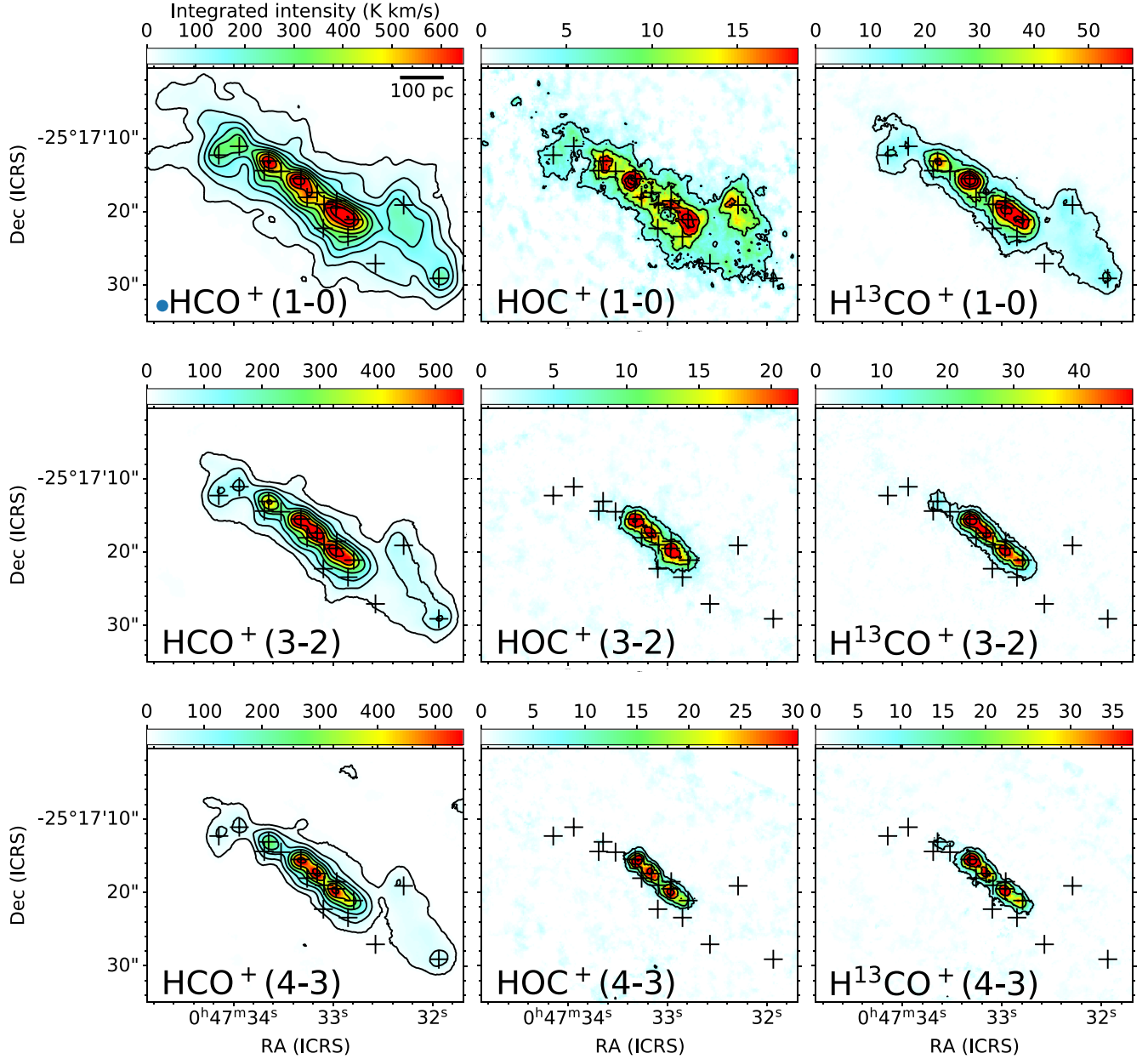
Figure 1. Velocity-integrated intensity images of the $J = 1-0$, $3-2$, and $4-3$ transitions of HCO^+, $H^{13}CO^+$, and HOC^+. The beam size of $1\overset{''}{.}6$ is shown at the bottom left corner of the first panel as a blue circle. Contour levels ($N = 1, 2, 3, ...$) are drawn for multiples of typical errors σ_{typ} listed in Table 2 for transitions $HCO^+(1-0)$: $20n^{1.7}\sigma_{typ}$, HCO^+ $(3-2)$: $20n^{2.0}\sigma_{typ}$, HCO^+ $(4-3)$: $20n^{2.0}\sigma_{typ}$, $HOC^+(1-0)$: $5n^{1.3}\sigma_{typ}$, $HOC^+(3-2)$: $10n^{1.3}\sigma_{typ}$, $HOC^+(4-3)$: $10n^{1.3}\sigma_{typ}$, $H^{13}CO^+(1-0)$: $10n^{1.7}\sigma_{typ}$, $H^{13}CO^+(3-2)$: $10n^{1.5}\sigma_{typ}$, and $H^{13}CO^+$ $(4-3)$: $10n^{1.5}\sigma_{typ}$. Gray crosses are positions analyzed in this paper (see Section 3.1 and Table 3).

3. Velocity-integrated Intensity Images and Ratios

3.1. Velocity-integrated Images

Figure 1 shows velocity-integrated intensity images of HCO^+, $H^{13}CO^+$, and HOC^+ in the $J = 1-0$, $3-2$, and $4-3$ transitions. Spectroscopic properties of these transitions are listed in Table 2. We did not include $J = 2-1$ transitions due to the poor atmospheric transmission close to the telluric water absorption near 183 GHz, although they are included in the Band 5 follow-up of our survey. The rms noise values of these images are not uniform throughout the images because we used the mask per channel (see Section 2), and the number of channels used for integration is different for each pixel. We discuss how we estimated the rms noise in these images in Appendix A. Despite the nonuniform rms values within the image, we can define σ_{typ}, typical error values for each image, assuming that the number of channels integrated is 40. Contours in moment 0 images (Figure 1) are displayed with multiples of σ_{typ}.

In this paper, we analyzed positions we named M# or A#, where # is a number. M1–10 are positions taken from Meier et al. (2015) corresponding to their clumps #1–10, and additional positions, A1–8, are also chosen for analysis. Out of these clumps, we did not include M1 due to the low S/N of the emission (position not shown with a gray cross in Figure 1) or M6 for the presence of an absorption feature (see Section 4) in our analysis.

The additional points are chosen for the following reasons. The position A1 is close to another superbubble identified by Krieger et al. (2019); A2 is placed at the base of the outflow

Table 3
Coordinates of Analyzed Positions

Position	R.A.(ICRS) 00h47m	Decl. (ICRS) −25°17′	Remarks
M2	32.29 s	19.10″	Near a superbubble and an SNR
M3	31.94 s	29.10″	
M4	32.79 s	21.10″	Near the base of an outflow (SW streamer), super hot core
M5	32.97 s	19.50″	IR Core, in a superbubble, hard X-ray source, super hot core
M7	33.32 s	15.50″	Super hot core
M8	33.65 s	13.10″	
M9	33.94 s	11.10″	Near a superbubble
M10	34.15 s	12.30″	Near a superbubble
A1	32.57 s	27.07″	Near a superbubble
A2	32.85 s	23.42″	On the outflow SW streamer
A3	32.96 s	18.53″	Shell of a superbubble
A4	33.10 s	22.27″	Shell of a superbubble
A5	33.09 s	19.01″	Shell of a superbubble
A6	33.26 s	18.05″	
A7	33.52 s	14.51″	Near a superbubble
A8	33.69 s	14.41″	Near a superbubble

Note. Superbubbles identified by Sakamoto et al. (2006) or Krieger et al. (2019); supernova remnants (SNRs) by Ulvestad & Antonucci (1997); the southwest streamer by Bolatto et al. (2013); super hot cores by Rico-Villas et al. (2020); IR core by Watson et al. (1996); X-ray sources by Müller-Sánchez et al. (2010).

(southwest streamer); A3, A4, and A5 are at the edge of the superbubble surrounding M5; and other positions are chosen somewhere in between the molecular clumps. The position A6 is close to clump 5 in Leroy et al. (2015). The positions A7 and A8 are also on the shell of superbubbles, different from the ones surrounding M5. Additional information for these positions is shown in Table 3.

To aid the discussion of the distribution of emission, we plotted the positions analyzed in this paper, along with the positions of hard X-ray sources (Müller-Sánchez et al. 2010), molecular superbubbles (Sakamoto et al. 2006; Krieger et al. 2019), and radio sources (Ulvestad & Antonucci 1997) on the moment 0 images of HCO$^+$(1−0) and HOC$^+$(1−0); (Figure 2). We make a distinction between superbubbles identified in our data and ones that are not identified in our data but are reported by Krieger et al. (2019), because the ones taken from the literature only have approximate positions (solid and dotted green circles in Figure 2).

The distribution of emission varies with species and transitions. The integrated intensity image of HCO$^+$(1−0) is consistent with that reported by Leroy et al. (2015) from earlier ALMA observations with a beam size of $1''9 \times 1''3$, equivalent to that of our data. Emission of higher-J transitions is more concentrated around the central star clusters because of the higher excitation conditions they require. Emission of H^{13}CO$^+$ is more compact than that of HCO$^+$ due to its lower abundance, which means H^{13}CO$^+$ has a lower optical depth and get less help for excitation from photon trapping. For the moment 0 image of H^{13}CO$^+$(1−0), there is a "hole" in the emission at the location of "TH2" (near position M6), one of the brightest continuum positions reported by Turner & Ho (1985) and close to the dynamical center of the galaxy. As we discuss in Section 4, the spectra obtained toward this position show that
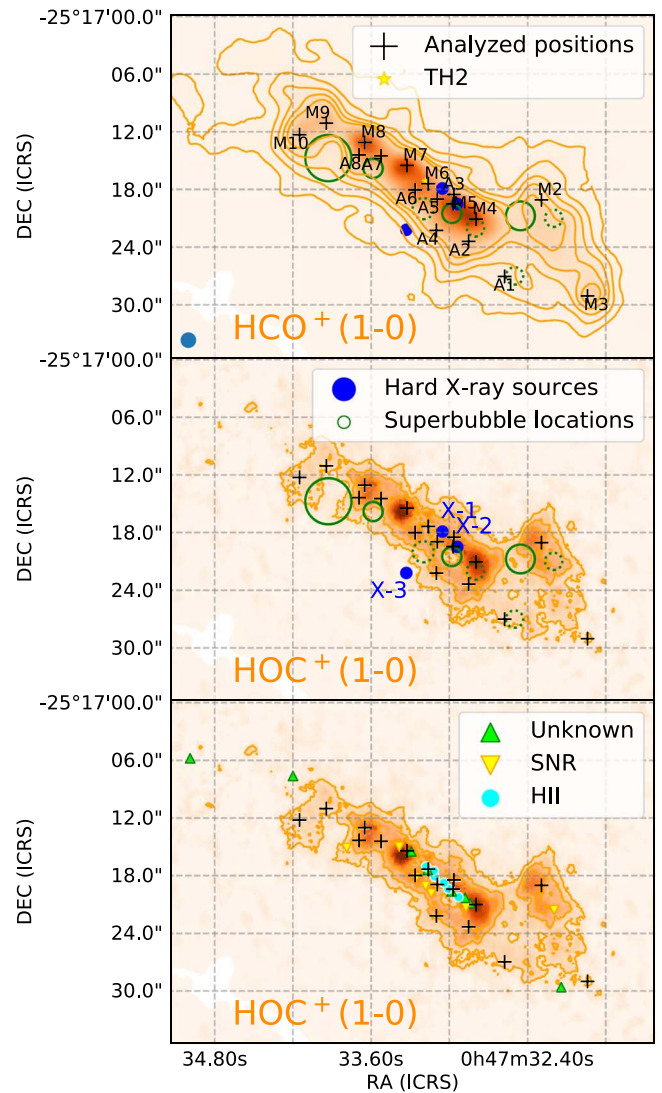

Figure 2. Positions that are analyzed in this paper: hard X-ray sources and superbubble positions are overlaid on (top) HCO$^+$(1−0) and (middle) HOC$^+$(1−0) moment 0 images. Superbubble locations are shown with green solid circles for ones that were identified in our data, while those that we do not identify in our data but were reported in Krieger et al. (2019) are shown with dotted green circles with only approximate sizes and locations. Labels of analyzed positions are shown in the top figure, while hard X-ray sources are labeled in the middle figure for the legibility. Bottom panel: radio sources from Ulvestad & Antonucci (1997) are also plotted over HOC$^+$(1−0) according to their spectral type (supernova remnants, H II regions, or unknown).

this is due to absorption against the strong continuum. The absorption of H^{13}CO$^+$(1−0) is more visible than that of HCO$^+$(1−0), likely because its emission is more compact than that of HCO$^+$ within the beam. This difference in the extent of absorption becomes more apparent in the spectra shown in Section 4. We do not resolve the continuum source, and find emission surrounding TH2 and absorption against TH2 within the beam. Nonetheless, the HCO$^+$(1−0) transition is also likely affected by absorption judging from the spectral shape (Section 4). This may be the reason why there is no obvious clump in the TH2 position in the HCO$^+$(1−0) moment 0 image (also noted in Leroy et al. 2015), although there is a molecular clump in higher-J transitions.

Emission of HOC$^+$(1−0) has a different distribution compared to that of HCO$^+$, H^{13}CO$^+$, and higher-J transitions of HOC$^+$ near positions M2, M5, and M6. There is a superbubble reported by

Krieger et al. (2019) at position M5. Unlike HCO⁺ and H¹³CO⁺, which show a relatively smooth distribution, HOC⁺ shows a hole-like structure clearly tracing this superbubble. This distribution implies that HOC⁺ is enhanced at locations with unusual physical conditions, instead of tracing dense gas in general. Even in regions with hole-like suppressed intensities in HOC⁺(1−0), the intensities of higher-J transitions do not show any decrease in those regions, indicating higher excitation temperatures in these structures. At position M2, there is an enhancement of HOC⁺(1−0) in the northern part. There is another superbubble reported by Sakamoto et al. (2006) near this position (the western-most superbubble shown in Figure 2 middle), in addition to a supernova remnant toward the southwest direction (Figure 2 bottom). At TH2 near position M6, there is also a suppression of HOC⁺(1−0) similar to that of H¹³CO⁺(1−0).

3.2. Ratio Maps

Figures 3 and 4 show velocity-integrated intensity ratio maps of HCO⁺, HOC⁺, and H¹³CO⁺ for the three transitions we observed. In addition to the mask used to create these moment 0 images, we eliminated any emission below 5σ from each velocity-integrated intensity image before ratios were taken. Note that σ here is not $\sigma_{\rm typ}$, but the rms of the velocity-integrated intensity image estimated by considering the single-channel rms and velocity width and the number of channels integrated as shown in Appendix A. The HCO⁺/H¹³CO⁺(1−0) ratio map was created to assess the optical depth of HCO⁺(1−0). The range of the HCO⁺/H¹³CO⁺(1−0) intensity ratio is 20 ± 8. If both lines are optically thin and the two species share the same excitation temperatures, their column density ratios can be obtained by dividing these intensity ratios by 1.1, the ratio between Einstein coefficients of these transitions. On average, these ratios are consistent with values of ¹²C/¹³C derived from ¹³C¹⁸O by Martín et al. (2019b) at 3″ resolution and to that from HCO⁺ at the 15″ resolution ALCHEMI data extracted only from ALMA 7 m array measurements (Martín et al. 2021). The low ratios of HCO⁺/H¹³CO⁺(1−0) may also be affected by the optical depth of HCO⁺, especially for the central clumps (see the discussion in Martín et al. 2021). The HCO⁺/H¹³CO⁺ ratios in the two higher-J transitions are similar to that for $J = 1−0$ except for emission from the edge, which may be affected by low S/N.

If the regions are optically thin, which may not be the case for the densest clumps, and if HCO⁺ and HOC⁺ share similar excitation temperatures, the HCO⁺/HOC⁺(1−0) intensity ratios multiplied by 0.5 (the ratio between the Einstein A coefficients of these transitions) can be used as the HCO⁺/HOC⁺ abundance ratios. The H¹³CO⁺/HOC⁺ ratios are less affected by the optical depth, so they are potentially better at constraining the HCO⁺/HOC⁺ ratio. However, these ratios are not proportional to HCO⁺/HOC⁺ if the ¹²C/¹³C ratio is not uniform throughout the image, as in Martín et al. (2019b). Overall, the H¹³CO⁺/HOC⁺ and HCO⁺/HOC⁺ ratios show similar distributions, indicating that the saturation of HCO⁺ is not significant for most regions. The lowest ratios are measured near the southwest part of the CMZ, at position M2. A high opacity is not expected at this position, which suggests that the HCO⁺/HOC⁺ abundance ratio is actually low. The highest ratio is seen near the position M5. Although this position is associated with a superbubble, the position inside the bubble does not have an enhanced HOC⁺, which is counter-intuitive. However, this region is also very crowded with the IR core, a hard X-ray source, and super hot cores, and thus the interpretation of the high ratio of HCO⁺/HOC⁺ is not
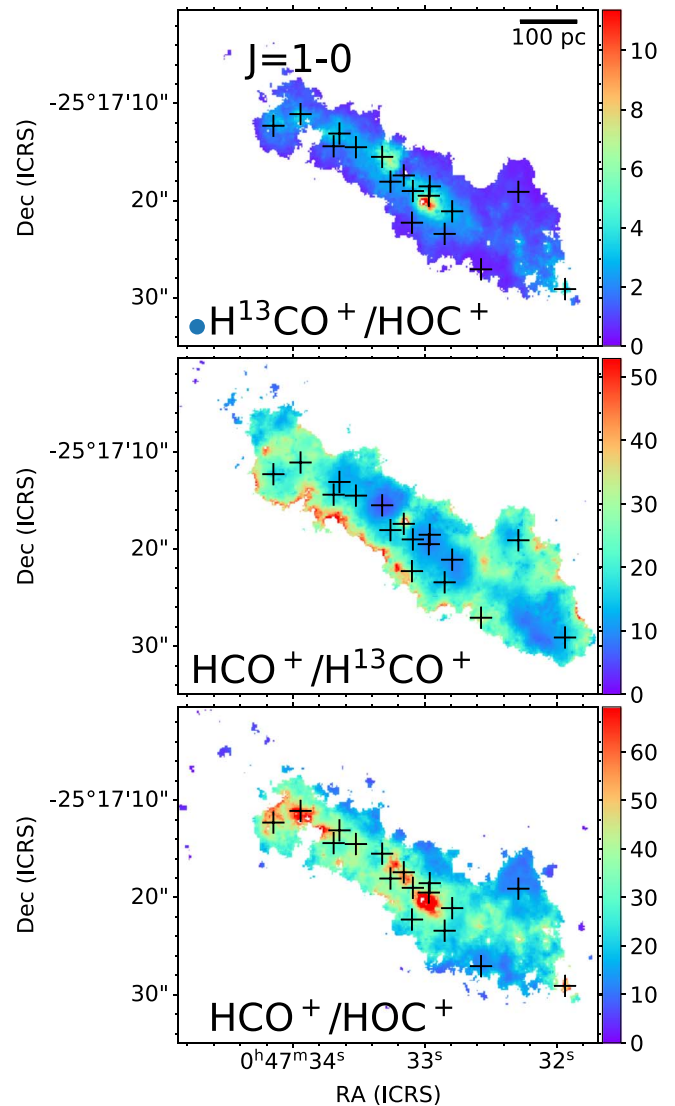

Figure 3. Ratios of velocity-integrated intensity images for the $J = 1–0$ transitions. Gray crosses show the positions M2−10 and A1−8.

straightforward. The HCO⁺/HOC⁺ ratios tend to become lower with higher galactic latitude, which likely has a lower density. The density dependence of the HCO⁺/HOC⁺ ratios is discussed in Section 6.

The HCO⁺/HOC⁺ and H¹³CO⁺/HOC⁺ ratios of two higher-J transitions show different variations compared to $J = 1–0$ transition. In $J = 1–0$ transition, the above ratios are slightly higher in clumps (high column density regions such as positions M4–M8) compared with more extended components. This trend is not seen in $J = 4–3$. The HCO⁺/HOC⁺(4–3) ratio is rather lower in clumps compared with extended regions. This is likely due to blending with SO₂ as we discuss in Section 4.

4. Spectra at Selected Positions

Figures 5 and 6 show the spectra of lines of interest at positions M7 and M6 (next to TH2). Their intensities are taken from a pixel corresponding to the coordinates of these positions and are converted to brightness temperature (e.g., Equation (3.31) in the ALMA Cycle 8 Technical Handbook). Position M7 is the chemically richest among all of the positions, while
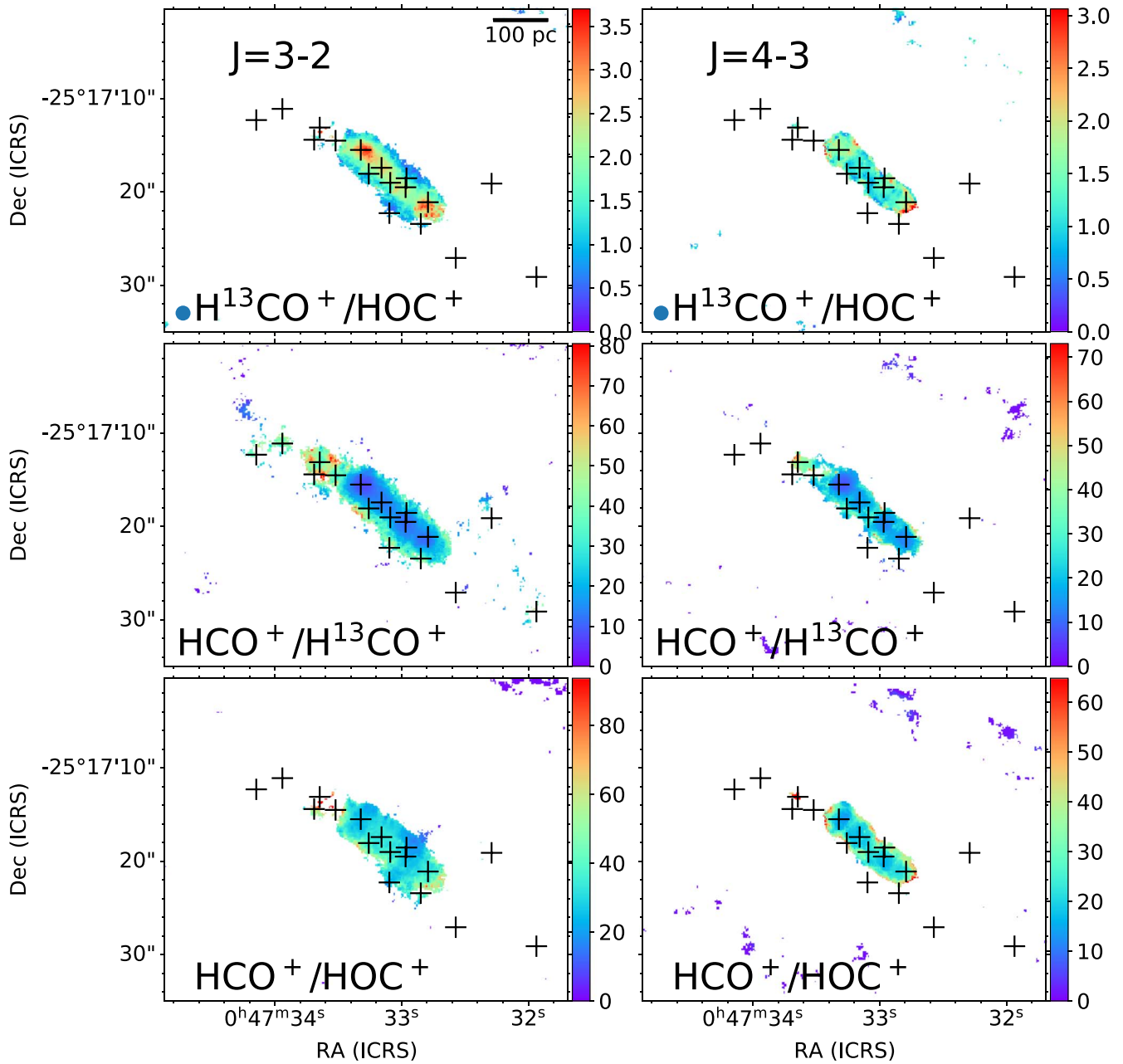
Figure 4. Same as Figure 3, but for $J = 3$–2 and $J = 4$–3 transitions.

position M6 is known to possess absorption in $H^{13}CO^+(1-0)$ and $HCO^+(1-0)$ against the continuum emission from TH2. We observe similar decrements in spectral shapes of $HOC^+(3-2)$ and $(4-3)$, but that in $HOC^+(1-0)$ cannot be confirmed at the current sensitivity. The spectra for other positions are shown in Appendix B.

There are some neighboring and partially blended transitions adjacent to our transitions of interest labeled in Figure 5. However, many of the neighboring transitions and some blended transitions are unlikely to cause problems because we decompose the blended or neighboring lines through a multi-line spectral fitting for our analysis. Based on our spectral fitting analysis in Section 5, we show that contamination does not affect our analysis except for SO_2 transitions blended with $HOC^+(4-3)$. For positions with strong SO_2 emission (positions

M4, M5, and M7), we fit the HOC^+ transitions together with SO_2 transitions. This is possible because there are multiple neighboring SO_2 transitions in addition to the ones blended into the transition of $HOC^+(4-3)$. The decrement in the $HOC^+(4-3)$ line shape may be partly (or mostly) due to the blended lines or multiple velocity components of HOC^+.

We note that some of the spectral features of $H^{13}CO^+ (1-0)$ could appear like the P-Cygni profile (redshifted emission plus blueshifted absorption), but this spectral feature is not likely due to an outflow. The P-Cygni profile is reported as evidence of outflow features in other locations in 28 mas resolution observations by Levy et al. (2021). In our case, the spectra are more affected by the strong contamination by emission surrounding the continuum in our coarser $1\rlap{.}''6$ resolution images.
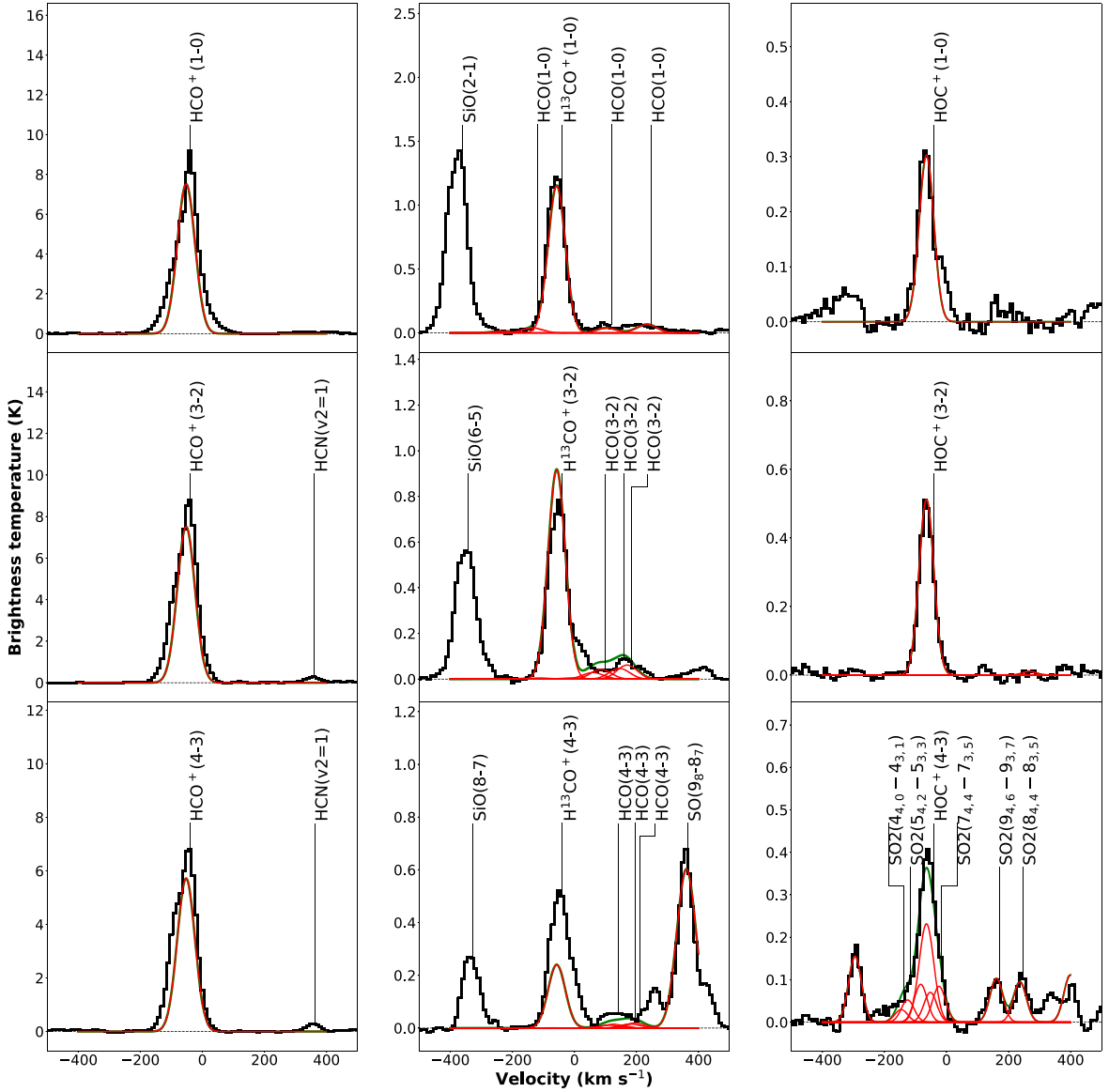
Figure 5. Spectra of lines at the M7 position. Spectra are centered at the systemic velocity $v_{sys,LSRK} = 243$ km s^{-1}. The fit to each molecular transition is shown as a red solid line, while the sums of line intensities at each frequency are shown as a green line.

5. Column Densities and Ratios

We derived column densities toward the positions shown in Figure 2, whose coordinates are listed in Table 3. The derived column densities and excitation temperatures of HOC$^+$, HCO$^+$, H^{13}CO$^+$, and C^{18}O are listed in Table 4. These column densities were derived using MADCUBA (Martín et al. 2019a). MADCUBA determines the column densities and excitation temperatures through spectral fitting under the assumption of local thermodynamic equilibrium with consideration of optical depth in the modeled spectra. In MADCUBA, the continuum-subtracted brightness temperature of the transition T_L is modeled as

$$T_L = [J(T_{ex}) - J(T_c) - J(T_{bg})](1 - e^{-\tau_\nu}) \qquad (1)$$

where J is the intensity in the temperature unit, T_{ex} is the excitation temperature, T_c is the continuum brightness temperature, T_{bg} is the background temperature, and τ_ν is the optical depth at the frequency ν (Equation (6) of Martín et al. 2019a). It is apparent that the intensity is insensitive to an extremely

high optical depth. We assumed a large source size (10″) to simulate emission filling the beam (i.e., no beam dilution) so the line brightness temperature is similar to the synthesized beam temperature. If only one transition was detected, we assume an excitation temperature of 5.0 K for the derivation of column densities of H^{13}CO$^+$ or HOC$^+$. This excitation temperature is similar to that of HCO$^+$ in positions where high-J transitions of HOC$^+$ or H^{13}CO$^+$ are not detected. Note that all three transitions of HCO$^+$ are detected in all of the positions analyzed here. The line widths are in the range of 50–100 km s^{-1} in full-width at half maximum, except for a component in the position A5 with $\sim$150 km s^{-1}.

5.1. HCO$^+$/H^{13}CO$^+$

Table 5 shows the column density ratios of N(HCO$^+$)/N(H^{13}CO$^+$), N(HCO$^+$)/N(HOC$^+$), and N(H^{13}CO$^+$)/N(HOC$^+$). Before presenting HCO$^+$/HOC$^+$ abundance ratios, we discuss the H^{12}CO$^+$/H^{13}CO$^+$ ratio to see if the ^{12}C/^{13}C ratio in HCO$^+$ is
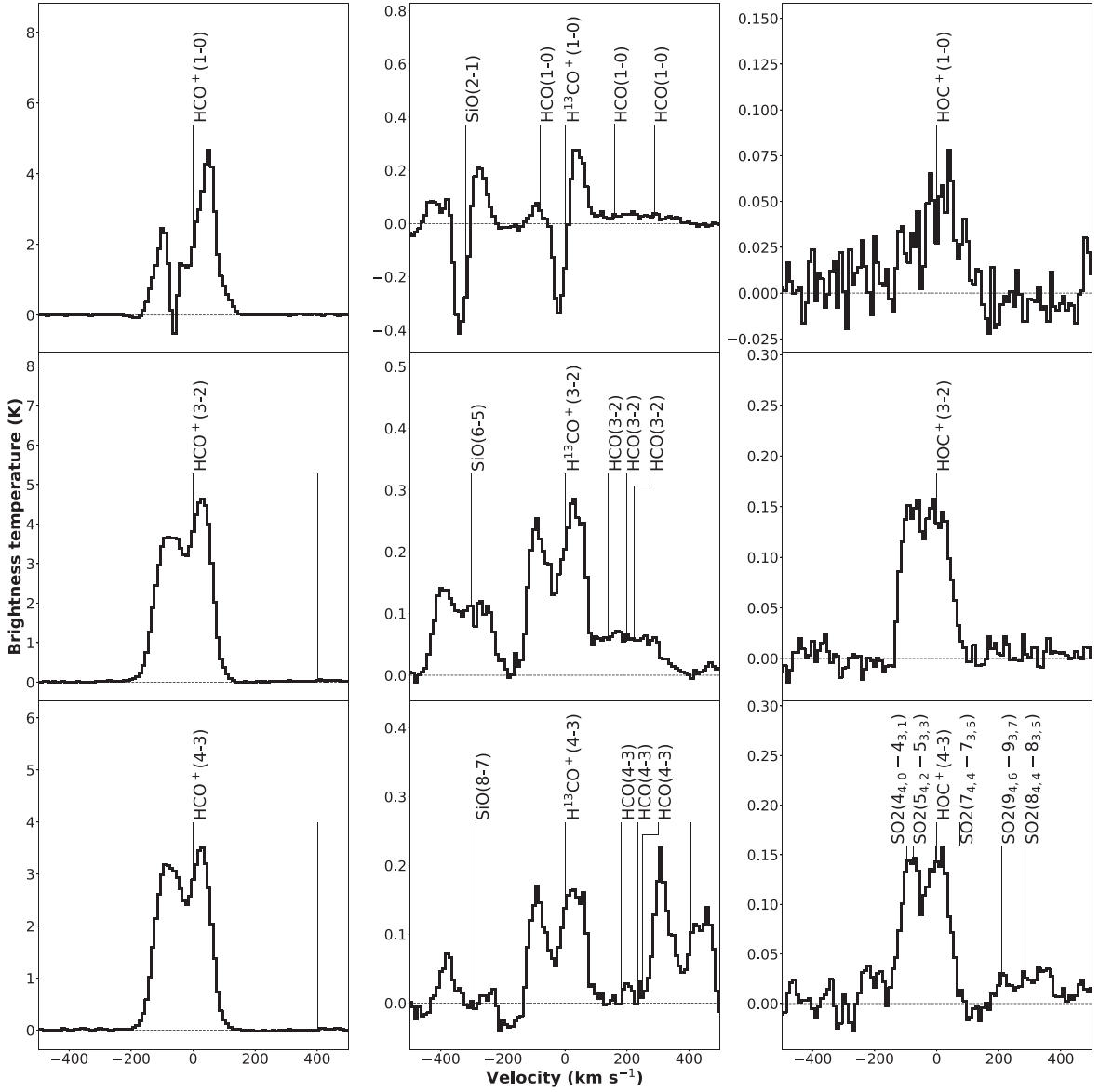
Figure 6. Same as Figure 5, but for the position M6. Because position M6 is not analyzed due to the absorption feature, the fit is not shown.

reasonable compared with the literature values of the carbon isotopic ratio in NGC 253 in order to check if the HCO⁺ transitions are optically thick. As mentioned earlier, this optical depth effect is taken into account in the derivation of column densities in MADCUBA, but it should still be checked in the case of very high optical depths. Values of $N(\text{HCO}^+)/N(\text{H}^{13}\text{CO}^+)$ are relatively low, ~10–30. These values are similar to the intensity ratios of $\text{HCO}^+/\text{H}^{13}\text{CO}^+$ discussed in Section 3. MADCUBA fitting results show that HCO⁺ is optically thick ($\tau > 4$) in a few positions (M4, M5, and M8) of the CMZ, but has $\tau \sim 2-4$ in A6, A8, M7, M9, and M10, and is optically thin in other positions when a transition with the highest optical depth is considered (see Table 4). The $^{12}\text{C}/^{13}\text{C}$ ratios obtained in NGC 253 in the literature are 21 ± 6 (Martín et al. 2019b) from $\text{C}^{18}\text{O}/^{13}\text{C}^{18}\text{O}$, which is close to our obtained values. However, note that the $^{12}\text{C}/^{13}\text{C}$ ratio can also depend on the species because of fractionation (Colzi et al. 2020; Viti et al. 2020).

5.2. HCO⁺/HOC⁺

We derive the abundance ratio of HCO⁺/HOC⁺ using two methods to account for possible effects of line saturation. The first method is to directly use the column density ratios $N(\text{HCO}^+)/N(\text{HOC}^+)$; (Method 1). This method should be a good indicator of HCO⁺/HOC⁺ in optically thin regions, which likely holds for most of the observed regions. The other method is to take the column density ratios of $\text{H}^{13}\text{CO}^+/\text{HOC}^+$ and multiply them by an assumed constant $^{12}\text{C}/^{13}\text{C}$ across the entire region ($\frac{^{12}C}{^{13}C} N(\text{H}^{13}\text{CO}^+)/N(\text{HOC}^+)$, Method 2). This method may shed light on the errors from the optically thick regions, but this method is also dependent on the isotopic ratios of $^{12}\text{C}/^{13}\text{C}$. Here, we assume the carbon isotopic ratio $^{12}\text{C}/^{13}\text{C} = 20 \pm 10$. This value is suggested by our $\text{HCO}^+/\text{H}^{13}\text{CO}^+(1-0)$ intensity ratio (see Section 3.2), and is similar to the value obtained by Martín et al. (2019b). The column density ratios of HCO⁺/HOC⁺ and

Table 4
Observed Column Densities and Excitation Temperatures

Region	$N(HCO^+)$ $(10^{14}\ cm^{-2})$	$T_{ex}(HCO^+)$ (K)	$N(HOC^+)$ $(10^{12}\ cm^{-2})$	$T_{ex}(HOC^+)$ (K)	$N(H^{13}CO^+)$ $(10^{12}\ cm^{-2})$	$T_{ex}(H^{13}CO^+)$ (K)	$N(C^{18}O)$ $(10^{16}\ cm^{-2})$	$T_{ex}(C^{18}O)$ (K)	$\tau(HCO^+, max)$
M2	1.6 ± 0.2	6.4 ± 0.2	14.1 ± 1.9	4.2 ± 0.3	11.3 ± 1.2	4.4 ± 0.3	5.1 ± 0.2	8.0 ± 0.2	0.6
	0.7 ± 0.1	6.5 ± 0.4	5.1 ± 0.8	$5.0 \pm ...$	3.6 ± 0.4	$5.0 \pm ...$	2.1 ± 0.2	7.4 ± 0.5	
M3	3.3 ± 0.1	7.3 ± 0.2	6.7 ± 2.1	4.2 ± 0.8	19.0 ± 1.3	4.8 ± 0.2	5.0 ± 0.3	8.6 ± 0.4	0.7
M4	23.9 ± 3.7	10.5 ± 0.2	25.3 ± 0.7	7.5 ± 0.1	79.2 ± 3.4	7.0 ± 0.2	17.3 ± 0.6	17.5 ± 0.7	9.7
M5	11.0 ± 0.8	13.0 ± 0.3	13.4 ± 0.5	17.8 ± 0.7	71.1 ± 3.9	9.1 ± 0.3	13.9 ± 0.2	25.0 ± 0.9	4.4
	8.0 ± 3.8	5.2 ± 0.3	5.1 ± 0.9	6.1 ± 0.9	15.4 ± 2.5	$5.0 \pm ...$	5.4 ± 0.4	10.2 ± 0.6	
M7	12.8 ± 0.8	13.5 ± 0.3	21.2 ± 0.7	12.3 ± 0.3	105.0 ± 5.1	8.1 ± 0.2	20.6 ± 0.4	23.6 ± 0.9	3.6
M8	13.2 ± 2.3	9.9 ± 0.2	20.7 ± 1.5	4.8 ± 0.3	60.5 ± 2.0	5.3 ± 0.1	12.1 ± 0.4	13.4 ± 0.4	4.3
M9	6.5 ± 0.5	6.6 ± 0.2	6.1 ± 0.6	4.8 ± 0.4	20.6 ± 1.2	4.8 ± 0.2	5.2 ± 0.3	10.2 ± 0.4	2.4
M10	6.3 ± 0.6	6.0 ± 0.1	6.8 ± 0.4	$5.0 \pm ...$	21.7 ± 1.4	4.6 ± 0.2	5.9 ± 0.2	8.7 ± 0.2	2.4
A1	1.0 ± 0.1	5.4 ± 0.2	6.0 ± 0.5	$5.0 \pm ...$	3.7 ± 0.3	$5.0 \pm ...$	3.3 ± 0.2	6.6 ± 0.2	0.4
A2	4.6 ± 0.2	6.9 ± 0.2	10.7 ± 0.8	5.4 ± 0.3	18.8 ± 1.0	4.9 ± 0.2	4.0 ± 0.2	12.1 ± 0.5	1.2
A3	6.9 ± 0.6	9.8 ± 0.3	13.0 ± 0.8	12.1 ± 0.5	39.0 ± 2.0	7.7 ± 0.2	9.2 ± 0.2	19.6 ± 0.6	1.7
	...	...	...	...	...	...	2.7 ± 0.2	9.3 ± 0.6	
A4	4.1 ± 0.2	6.1 ± 0.1	9.3 ± 0.5	6.2 ± 0.2	17.6 ± 1.3	4.5 ± 0.2	3.4 ± 0.1	11.4 ± 0.4	1.2
A5	3.0 ± 1.3	6.4 ± 1.0	8.0 ± 2.8	4.2 ± 0.9	12.4 ± 3.2	4.5 ± 0.9	2.9 ± 0.4	8.2 ± 0.9	1.9
	4.3 ± 0.2	11.7 ± 0.4	6.9 ± 0.4	20.2 ± 1.3	34.5 ± 2.6	8.1 ± 0.3	8.8 ± 0.4	18.9 ± 1.1	
A6	4.6 ± 0.8	8.1 ± 0.3	7.8 ± 0.5	6.6 ± 0.2	16.7 ± 0.9	6.4 ± 0.2	3.1 ± 0.1	10.0 ± 0.3	2.3
	3.0 ± 0.9	5.9 ± 0.5	3.6 ± 0.5	$5.0 \pm ...$	9.8 ± 0.9	5.6 ± 0.3	3.8 ± 0.1	16.6 ± 0.6	
	2.3 ± 0.1	9.9 ± 0.3	4.6 ± 0.4	14.8 ± 0.9	8.8 ± 0.7	8.6 ± 0.4	2.8 ± 0.1	23.8 ± 1.9	
A7	4.2 ± 0.3	8.0 ± 0.2	6.2 ± 0.7	5.1 ± 0.4	24.7 ± 1.2	5.3 ± 0.2	3.1 ± 0.2	11.4 ± 0.5	1.5
	2.4 ± 1.1	6.4 ± 0.5	8.1 ± 0.8	5.3 ± 0.3	6.5 ± 0.8	5.7 ± 0.3	5.7 ± 0.2	14.1 ± 0.5	
A8	7.0 ± 0.6	7.1 ± 0.2	10.2 ± 1.2	5.0 ± 0.4	20.9 ± 1.6	4.8 ± 0.2	5.7 ± 0.2	11.6 ± 0.3	2.2
	0.8 ± 0.1	7.0 ± 0.5	4.4 ± 0.5	$5.0 \pm ...$	11.8 ± 2.7	4.2 ± 0.5	1.7 ± 0.2	13.1 ± 1.2	

Note. As mentioned in Section 5, the excitation temperature was fixed when the species is only detected in one transition. For these cases, the errors of excitation temperature are not shown. Errors shown are only from spectral fitting and do not contain observational errors. These column densities are derived with the consideration of optical depth. The maximum value of the optical depth of HCO^+ is shown in the last column. Only the component with the highest value is shown for each position.

Table 5
Column Density Ratios

Region	$N(HCO^+)/N(H^{13}CO^+)$	$N(HCO^+)/N(HOC^+)$	$N(H^{13}CO^+)/N(HOC^+)$
M2	15.2 ± 2.5	11.9 ± 2.3	0.8 ± 0.1
M3	17.2 ± 1.3	48.5 ± 15.4	2.8 ± 0.9
M4	30.1 ± 4.8	94.5 ± 14.7	3.1 ± 0.2
M5	22.0 ± 5.5	102.8 ± 25.8	4.7 ± 0.5
M7	12.2 ± 1.0	60.3 ± 4.3	5.0 ± 0.3
M8	21.9 ± 3.8	63.8 ± 11.8	2.9 ± 0.2
M9	31.6 ± 3.1	106.0 ± 13.1	3.4 ± 0.4
M10	29.2 ± 3.5	93.8 ± 11.4	3.2 ± 0.3
A1	26.8 ± 2.8	16.8 ± 1.6	0.6 ± 0.1
A2	24.6 ± 1.9	43.4 ± 3.9	1.8 ± 0.2
A3	17.7 ± 1.7	52.9 ± 5.5	3.0 ± 0.2
A4	23.2 ± 1.9	44.1 ± 2.9	1.9 ± 0.2
A5	15.6 ± 3.8	49.1 ± 14.7	3.2 ± 0.8
A6	28.1 ± 5.7	61.9 ± 12.9	2.2 ± 0.2
A7	21.4 ± 4.7	46.6 ± 10.8	2.2 ± 0.3
A8	23.8 ± 3.8	53.5 ± 7.8	2.2 ± 0.4

Note. Errors shown are only from spectral fitting and do not contain observational errors.

$H^{13}CO^+/HOC^+$ are also included in Table 5. Values of HCO^+/HOC^+ abundance ratios estimated from the abovementioned methods are also displayed in Figure 7. As already shown in the ratio map of $HCO^+/HOC^+(1-0)$, the abundance ratio of HCO^+/HOC^+ is low at the position M2. In addition, the position A1 also has a comparably low ratio.

5.3. Fractional Abundances

In addition to column density ratios, we derived fractional abundances defined as the column density of a species over total hydrogen column density (here denoted as X(species)). To obtain fractional abundances, we estimated the molecular hydrogen
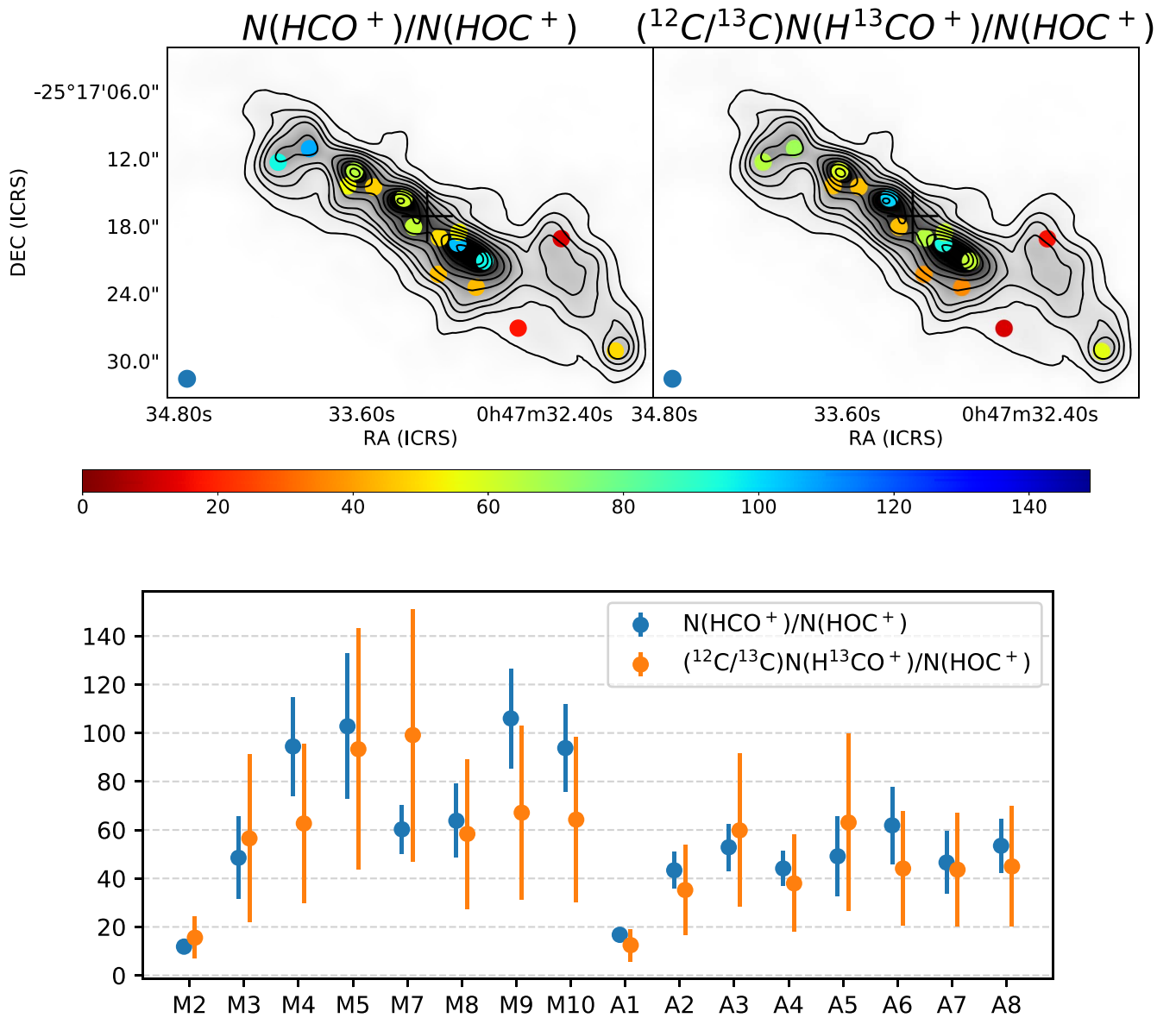
Figure 7. Abundance ratios of HCO^+/HOC^+ plotted as colored dots over HCO^+ moment 0 images (grayscale + contours) using $N(HCO^+)/N(HOC^+)$; (Method 1, top left) and $(^{12}C/^{13}C)N(H^{13}CO^+)/N(HOC^+)$; (Method 2, top right). The HCO^+/HOC^+ abundance ratios estimated from two methods in top panels are shown for individual positions together with error bars (bottom).

column densities from the dust continuum (see continuum images in Appendix D) and $C^{18}O$ column densities (see Appendix E) and assumed $N(H_{total}) = 2N(H_2)$ to obtain total hydrogen column densities. It is common for observational studies to show fractional abundances over molecular hydrogen column densities, not total hydrogen column densities. That said, chemical models often use fractional abundances over total hydrogen column densities. We show fractional abundances of $N(HOC^+)/N(H_{total})$ in Table 6.

Errors associated with quantities shown in Table 6 are as follows. For column densities of HCO^+, $H^{13}CO^+$, and HOC^+, errors from spectral fitting were added to an observational error of 15% (Martín et al. 2021). We used the value of the isotopic ratio with a large error $^{12}C/^{13}C = 20 \pm 10$ to account for the discrepancies between the observed ratios (Tang et al. 2019), although we favor values around 20 from $HCO^+/H^{13}CO^+$ in optically thin regions. For the error of $\log(N(HOC^+)/N(H_{total}))$, we used a conservative error $\log(2.0) = 0.30$ because the total column

densities from dust can easily change with different values of the dust emissivity power-law β or the dust temperature T_d, and because there are some discrepancies among total column densities derived from dust and $C^{18}O$ as discussed in Appendix E.

6. Chemical Modeling

We conducted modeling of chemical abundances in order to interpret our observational results. In particular, we examined the effect of the cosmic-ray ionization rate and the UV photons on molecular abundances. A modified version of the time-dependent, gas-grain code Nautilus (Hersant et al. 2009) was used to model the fractional abundances of the species of interest. This chemical network includes about 500 gas-phase species, and about 200 of them are also considered on the grain surface. The total number of gas-phase, accretion to or desorption from grains, and grain-surface reactions is about 8800. The basic network was taken from Ruaud et al. (2015),

Table 6
Observed HOC$^+$ Fractional Abundances and HCO$^+$/HOC$^+$ Ratios

Region	log(N(HOC$^+$)/N_{tot})	log(N(HCO$^+$)/N(HOC$^+$)) Method 1	log(N(^{12}C/^{13}C)N(H^{13}CO$^+$)/N(HOC$^+$)) Method 2
M2	-9.76 ± 0.30	1.07 ± 0.11	1.19 ± 0.24
M3	-10.20 ± 0.30	1.69 ± 0.15	1.75 ± 0.27
M4	-10.53 ± 0.30	1.98 ± 0.09	1.80 ± 0.23
M5	-10.84 ± 0.30	2.01 ± 0.13	1.97 ± 0.23
M7	-10.75 ± 0.30	1.78 ± 0.07	2.00 ± 0.23
M8	-10.27 ± 0.30	1.80 ± 0.10	1.77 ± 0.23
M9	-10.31 ± 0.30	2.03 ± 0.08	1.83 ± 0.23
M10	-10.31 ± 0.30	1.97 ± 0.08	1.81 ± 0.23
A1	-10.22 ± 0.30	1.22 ± 0.08	1.10 ± 0.23
A2	-10.02 ± 0.30	1.64 ± 0.08	1.55 ± 0.23
A3	-10.69 ± 0.30	1.72 ± 0.08	1.78 ± 0.23
A4	-10.04 ± 0.30	1.64 ± 0.07	1.58 ± 0.23
A5	-10.68 ± 0.30	1.69 ± 0.15	1.80 ± 0.25
A6	-10.53 ± 0.30	1.79 ± 0.11	1.64 ± 0.23
A7	-10.25 ± 0.30	1.67 ± 0.12	1.64 ± 0.23
A8	-10.09 ± 0.30	1.73 ± 0.09	1.65 ± 0.24

Note. Both HCO$^+$/HOC$^+$ and HOC$^+$ fractional abundances and their errors are shown on a logarithmic scale. Observational errors of 15% are taken into account.

but excluded the complexes formed through Eley–Rideal reactions on grain surfaces and other species that are newly added in their work. Those species are not relevant to our work, and our focus in this paper is not complex molecules formed through Eley–Rideal reactions. We use the elemental abundances shown in Table 7. We ran the chemical model in a grid of physical conditions with densities $n_H = 10^3$–10^6 cm^{-3}, where n is the total hydrogen volume density, not H$_2$ density. For the gas and dust temperatures, we used values obtained from the Meudon PDR code[25] (Le Petit et al. 2006), which has a detailed calculation of thermal structure including various heating and cooling mechanisms and radiative transfer. Although the Meudon code also derives chemical abundances including HCO$^+$ and HOC$^+$, we used Nautilus for the calculation of chemical abundances in order to examine the effect of grain-related reactions as well as the time dependence. While this is not a truly consistent treatment because the chemistry is coupled with heating and cooling of the gas, the approximate behavior of chemical compositions in PDRs and cosmic-ray dominated regions (CRDRs) should be reproduced. Overall, comparisons between results from the different chemical models show that the main conclusion of this paper does not change with different models. Further details of the input parameters used for the chemical modeling are included in Appendix C.

6.1. Chemical Reactions Leading to HCO$^+$ and HOC$^+$

In this section, we describe the chemical reactions related to the production and destruction of HCO$^+$ and HOC$^+$. Reactions discussed in this section are also shown schematically in Figure 8. Two main gas-phase chemical reactions leading to formation of HOC$^+$ discussed in Liszt et al. (2004) are
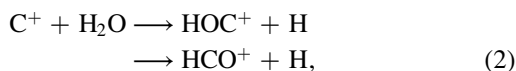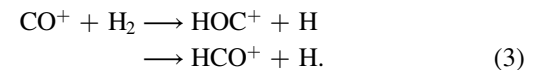
$$\text{C}^+ + \text{H}_2\text{O} \longrightarrow \text{HOC}^+ + \text{H}$$
$$\longrightarrow \text{HCO}^+ + \text{H}, \qquad (2)$$

Table 7
Elemental Abundances Used for Chemical Model

Element	X/H$_{total}$
He	0.14
N	2.14(−05)
O	1.76(−04)
C$^+$	7.3(−05)
S$^+$	8.00(−08)
Si$^+$	8.00(−09)
Fe$^+$	3.00(−09)
Na$^+$	2.00(−09)
Mg$^+$	7.00(−09)
P$^+$	2.00(−10)
Cl$^+$	1.00(−09)
F	6.68(−09)

Note. a(−b) means $a \times 10^b$.

and

$$\text{CO}^+ + \text{H}_2 \longrightarrow \text{HOC}^+ + \text{H}$$
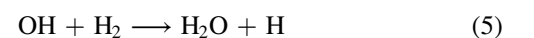$$\longrightarrow \text{HCO}^+ + \text{H}. \qquad (3)$$

As shown above, both of these reactions also produce HCO$^+$. The branching ratios assumed in our model to produce both HCO$^+$ and HOC$^+$ are HCO$^+$:HOC$^+$ = 33%:67% for the former reaction (Jarrold et al. 1986) and HCO$^+$:HOC$^+$ = 50%:50% for the latter reaction. Therefore, there is a relatively high abundance of HOC$^+$ when the region is influenced by UV photons or cosmic rays to enhance fractional abundances of C$^+$ or CO$^+$.

We find that the following channels lead to the production of HOC$^+$. The high gas temperature ($T \gtrsim 300$ K) helps both of the reactions above because of the following reactions with barriers

$$\text{O} + \text{H}_2 \longrightarrow \text{OH} + \text{H} \qquad (4)$$

with an activation barrier of 3160 K, and

$$\text{OH} + \text{H}_2 \longrightarrow \text{H}_2\text{O} + \text{H} \qquad (5)$$

PDR formation routes   **CRDR formation routes**
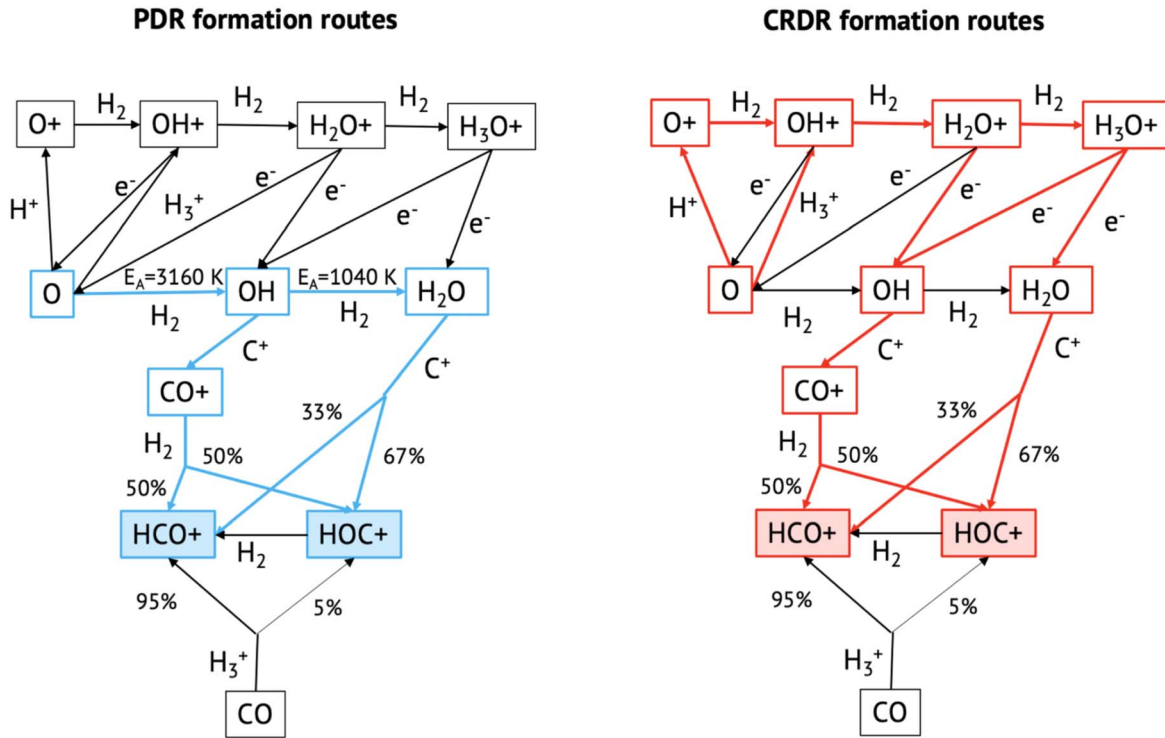

Figure 8. Graphical presentation of formation routes of HCO^+ and HOC^+ in the cases of PDRs and CRDRs. The blue boxes and arrows are species and reactions involved in the formation of HCO^+ and HOC^+ in PDRs, while red boxes and arrows are the ones in CRDRs. The activation barriers in the gas-phase formation of OH and water are indicated as E_A.

with an activation barrier of 1040 K, which produces OH and water efficiently. Thus, a high water abundance makes Reaction (2) faster, while a high OH abundance makes Reaction (3) more efficient because CO^+ is predominantly produced via reaction

$$C^+ + OH \longrightarrow CO^+ + H. \qquad (6)$$
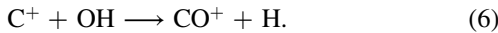
By contrast, the dominant production routes in CRDRs are as follows. At lower temperatures ($T_{gas} \lesssim 300$ K), there are alternative formation routes for OH and H_2O. When the cosmic-ray ionization rates are high, an oxygen atom can be ionized by its reactions with H^+. The ionized oxygen can successively become hydrogenated from reactions with molecular hydrogen,

$$OH_n^+ + H_2 \longrightarrow OH_{n+1}^+ + H \qquad (7)$$
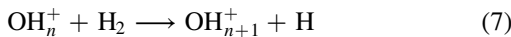
for $n = 0-2$, as described in Neufeld et al. (2010). There is another formation route of OH^+

$$O + H_3^+ \longrightarrow OH^+ + H_2, \qquad (8)$$
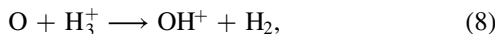
which also becomes efficient at the high cosmic-ray ionization rate due to an enhancement of H_3^+ (e.g., McCall et al. 2003). The ions produced in the reactions above, H_2O^+ and H_3O^+, can recombine with electrons to form water or OH.

Even without strong effects of UV photons or cosmic rays (e.g., $A_V > 10$ or $\zeta < 10^{-17}$ s^{-1}), HOC^+ can still be produced by the reaction $CO + H_3^+$. However, this reaction produces HCO^+ with a much higher branching ratio than HOC^+, with only 5% going to HOC^+ (Woon & Herbst 2009). In addition, high ratios of HCO^+/HOC^+ in quiescent regions (i.e., without strong UV radiation or cosmic-ray flux) are promoted by a

reaction that directly converts HOC^+ to HCO^+:

$$HOC^+ + H_2 \longrightarrow HCO^+ + H_2. \qquad (9)$$
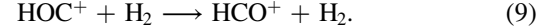
This reaction itself can occur in PDRs or CRDRs, but the HOC^+ production rates in PDRs/CRDRs are comparable to that of Reaction (9), which can maintain low HCO^+/HOC^+.

We employed the rate coefficient of 4×10^{-10} cm^3 s^{-1} for this reaction in our model following the experiments by Smith et al. (2002). This rate is different from the one listed in KIDA 2014 (Wakelam et al. 2015), which is the rate estimated by Herbst & Woon (1996a, 1996b) because we favor experimental rates over the theoretical estimation. For most other reaction rates, we use rates taken from KIDA 2014.

From the formation path via Reaction (3), CO^+ is expected in both PDRs and CRDRs. In our observations, we do detect CO^+, but we do not discuss this species because there is severe blending from neighboring transitions, including unidentified lines.

6.2. The Effects of UV Photons

We examined the effects of UV photons by varying the interstellar radiation field $G_0 = 1-10^5$ in the Habing field (interstellar radiation field, 1.6×10^{-3} erg cm^{-2} s^{-1}). First, we evaluate the average line-of-sight abundances by integrating fractional abundances over visual extinction A_V in the range of 0–5 mag. This maximum visual extinction is the value suggested from Fuente et al. (2008) in the case of the galactic center of the starburst galaxy M82, which has been suggested to act as a giant PDR. The actual maximum A_V may be different from this value, but an increase in the A_V will always lead to higher HCO^+/HOC^+ ratios because an increase in HOC^+ abundance only occurs at low $A_V < 5$, where the effects of UV
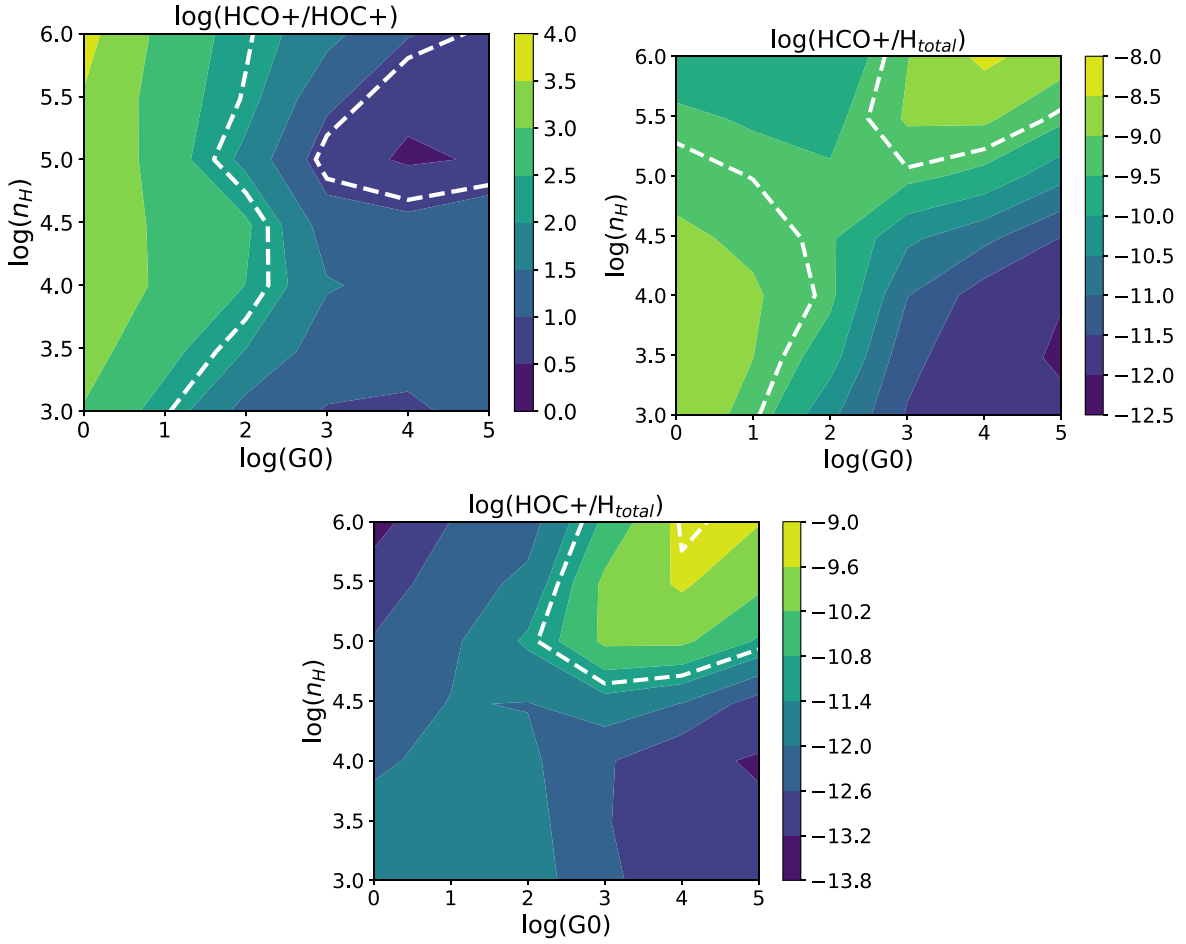
Figure 9. The abundance ratios of HCO^+/HOC^+; fractional abundances of HCO^+ and HOC^+ are shown as functions of density n_H and interstellar radiation field G_0. All of them are shown in the logarithmic scale. The abundances are averaged over $A_{V} = 0$–5 mag. For higher values of $A_{V,\max}$, HCO^+/HOC^+ will be higher and HOC^+/H_{total} will be lower. Observed ranges of $\log(HCO^+/HOC^+)$, $\log(HCO^+/H_{total})$, and $\log(HOC^+/H_{total})$ among all of the analyzed positions are shown with white dashed lines. The observed HCO^+/HOC^+ range shown here is a union of ranges obtained from both Methods 1 and 2 (see Section 5.2 for the description of two methods).

photons are greater. A fiducial value of the cosmic-ray ionization rate $\zeta = 10^{-17}$ s^{-1} was used for models presented in this section. Abundance ratios of HCO^+/HOC^+ are shown as a function of G_0 and n in Figure 9 (top left). These ratios decrease with increasing G_0, and are particularly low at high density ($n_H \gtrsim 10^5$ cm^{-3}), in high-G_0 regions. The fractional abundance of HCO^+ remains relatively high ($\gtrsim 10^{-10}$) for most values of the density and interstellar radiation field, except for extremely high G_0 and low n_H environments. By contrast, HOC^+ has fractional abundances higher than $\sim 10^{-10}$ only at a high density ($n_H \gtrsim 10^5$ cm^{-3}) and a high interstellar radiation field ($G_0 \gtrsim 10^3$).

The A_V dependence of the gas temperature, dust temperature, and fractional abundances of HCO^+ and HOC^+ are shown in Figure 10. In the low-density case shown in the top panels, the fractional abundance of HOC^+ is less than 10^{-11}, failing to produce the observed values. By contrast, higher density models (bottom panels) have high peak fractional abundances at certain A_V. For the case of $G_0 = 10^2$, the range of A_V where HOC^+ is enhanced is narrow, and the integrated fractional abundance ratio of HCO^+/HOC^+ is rather high as shown in Figure 9. Meanwhile, the case of higher $G_0 = 10^4$ shows the HOC^+ enhancement at a wide enough range of A_V, 3×10^{-3} to 0.3, has a significant effect on the HCO^+/HOC^+ ratio even after integrating to $A_V = 5$ mag. Note that the temperature

drops from ~ 2000 K to < 1000 K at $A_V \sim 0.03$, where the HOC^+ enhancement drops. The high fractional abundance of HOC^+ in high-density cases is attributed to the endothermic reactions that produce water and OH, precursors of HOC^+, efficiently at high gas temperatures as discussed in Section 6.1.

Our result shows that it is possible to produce relatively high abundances (10^{-10}) of HOC^+ with a high enough density and interstellar radiation field. This result is consistent with the work by Fuente et al. (2008), who claimed that the source of enhancement of HOC^+ is UV photons in dense gas. Meanwhile, this appears somewhat inconsistent with the result of Spaans & Meijerink (2007), who concluded that PDRs cannot produce observable column densities of CO^+ and HOC^+. Meijerink et al. (2007), upon which the result of Spaans & Meijerink (2007) is based, ran the calculation of a grid of densities and interstellar radiation field values. In all of their PDR models, the HCO^+/HOC^+ ratios are $> 10^4$, failing to produce a high enough enhancement of HOC^+ in comparison with HCO^+. However, these ratios are taken from column densities integrated to a certain maximum visual extinction ($A_V = 160$), defined by their "standard" cloud described in Meijerink et al. (2007). In fact, in these models by Meijerink et al. (2007), there is a certain range of A_V where the HCO^+/HOC^+ ratio is low (~ 10), in particular for high-density and high-G_0 cases.
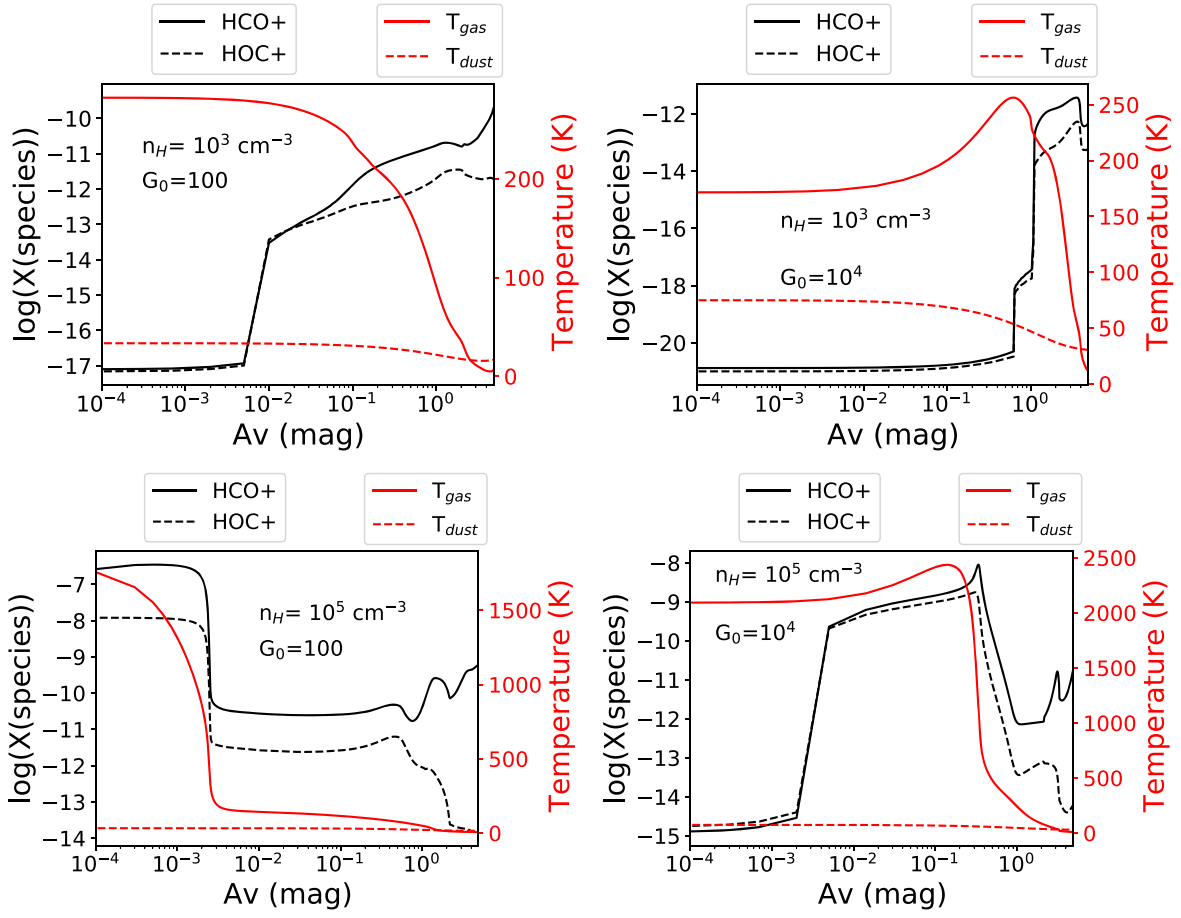
Figure 10. The fractional abundances of HCO^+ (black solid) and HOC^+ (black dotted) and gas temperature (red solid) and dust temperature (red dotted) are shown. The density and interstellar radiation field used for the model is $n_H = 10^3$ cm^{-3} and $G_0 = 10^2$ (top left), $n_H = 10^3$ cm^{-3} and $G_0 = 10^4$ (top right), $n_H = 10^5$ cm^{-3} and $G_0 = 10^2$ (bottom left), and $n_H = 10^5$ cm^{-3} and $G_0 = 10^4$ (bottom right).

The fractional abundance of HOC^+ and the HCO^+/HOC^+ ratio depend on the maximum visual extinction $A_{V,max}$. In chemical models shown above, we only integrate $A_V = 0-5$. Multiband infrared observations with the Very Large Telescope by Fernández-Ontiveros et al. (2009) show that the values of visual extinction are $\lesssim 10$, which is similar to the maximum A_V used in our models. That said, Leroy et al. (2018) and Mangum et al. (2019) have revealed that some clumps have $N(H_2) \sim 10^{24}$ cm^{-2} ($A_V \sim 1000$, assuming $N(H_{total})/A_V = 1.8 \times 10^{21}$ cm^{-2}), which is also consistent with total column densities we obtained for these locations (see Appendix E). This visual extinction suggests that the maximum values of A_V should be ~500 assuming that the star clusters are at the centers of giant molecular clouds (GMCs). Meanwhile, this value of visual extinction may not be used to measure the effect of UV photons. The visual extinction that affects the chemistry is the effective visual extinction, which considers the effect of UV photons averaged in all directions (e.g., Glover et al. 2010). While the effective visual extinction may be lower than the actual visual extinction in a clumpy medium, it is likely that visual extinction in some regions of the CMZ in NGC 253 may be much higher than 5. Therefore, the HCO^+/HOC^+ ratios for each n and G_0 we obtain here with $A_V = 5$ are likely lower than actual values if $A_V > 5$. In order to give a rough estimate of the effect of a higher maximum A_V, we calculated the average fractional abundance over $A_V = 0 - A_{V,max}$, $\bar{X}(A_{V,max})$ via

$$\bar{X}(A_{V,max}) \sim \left(\int_0^5 X(A_V) d(A_V) + X(A_V = 5) \right.$$
$$\left. \times (A_{V,max} - 5)/A_{V,max} \right. \tag{10}$$

where $X(A_V)$ is a fractional abundance as a function of A_V. This estimate is valid under the assumption that effects of UV photons are negligible for $A_V > 5$. When $A_{V,max} = 500$, the observed fractional abundance of HOC^+ cannot be reproduced even with $G_0 = 10^5$, and HOC^+ enhancement due to PDRs can be excluded unless $G_0 > 5$ (Figure 11). For a lower $A_{V,max} = 50$, observations can be reproduced for a higher radiation field of $G_0 = 10^3 - 10^4$, thus yielding higher values than for $A_{V,max} = 5$.

In order to compare the results from chemical modeling and observations, we plotted observed ranges of $\log_{10}(N(HCO^+)/N(HOC^+))$ and $\log_{10}(N(HOC^+)/N(H_{total}))$ against the modeled values as a function of G_0 and n (Figure 12). Because we use two methods to derive HCO^+/HOC^+ as explained in Section 5.2, we compare values derived by both methods with the models. We also examine two different assumptions for $A_{V,max}$. One is simply $A_{V,max} = 5$. The other assumption of $A_{V,max}$ is obtained using half of the total column density as described in Appendix E, and models are approximated with Equation (10). This factor of 2 comes assuming the GMCs are uniform and star clusters are located at the
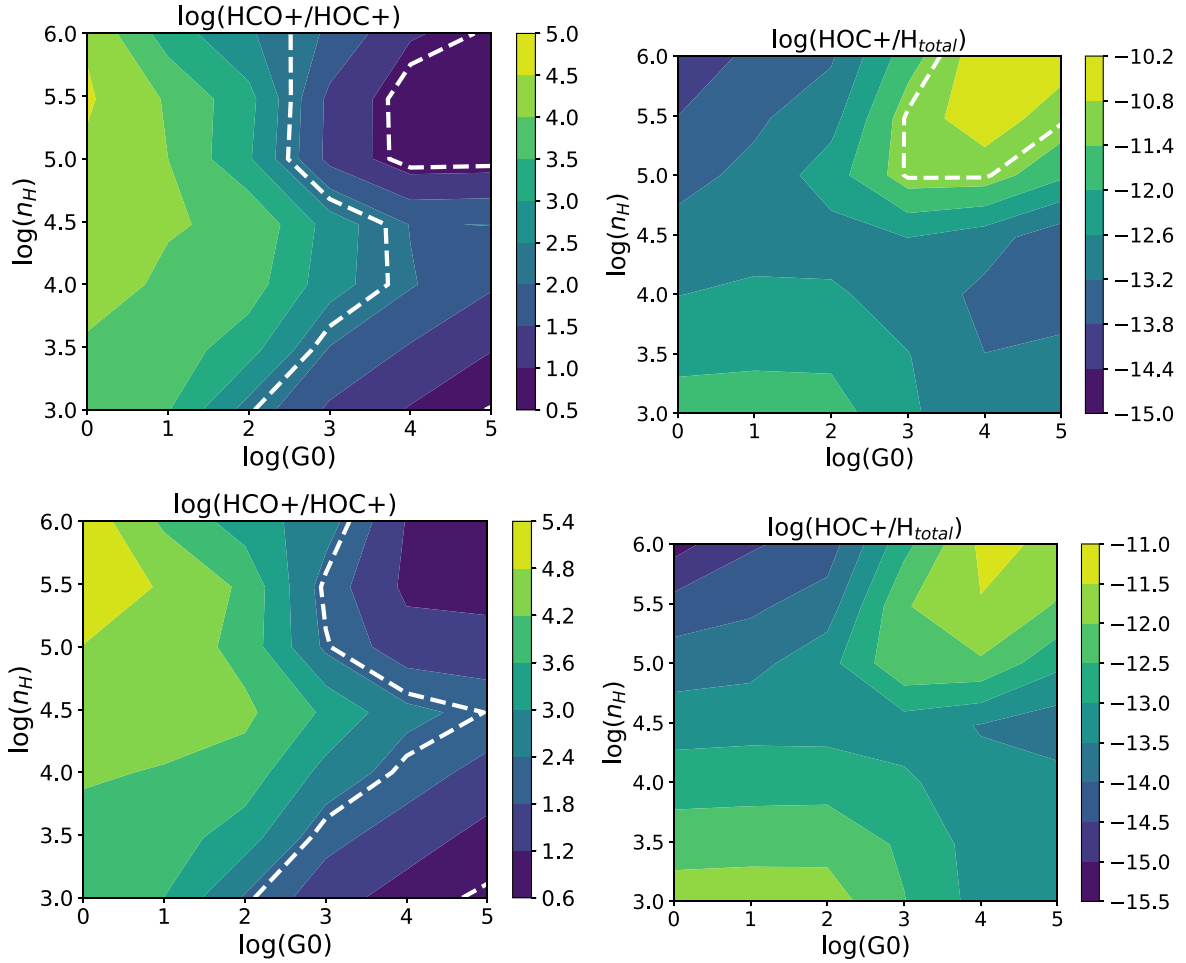
Figure 11. Same as Figure 9, but for $A_{V,\mathrm{max}} = 50$ (top) and 500 (bottom). In the right bottom figure, white dashed lines are not shown because the observed value is out of range.

center. For the positions shown in Figure 12, values of $A_{V,\mathrm{max}}$ found through this assumption are 30, 150, and 330, for positions M2, A6, and M7, respectively. The assumption of $A_{V,\mathrm{max}} = 5$ is likely a lower limit of the actual value, while the $A_{V,\mathrm{max}}$ from the total column density is an upper limit due to the clumpiness and nonuniform distribution of star clusters within our beam.

In Figure 12, the parameter space where agreement between the observation and the models is achieved can be found from the ranges of G_0 and n_H in which $X(\mathrm{HOC^+})$ and $\mathrm{HCO^+/HOC^+}$ overlap. First, we discuss the case where $A_{V,\mathrm{max}} = 5$. A good agreement is achieved for $G_0 \sim 10^{3.5}$ and $n_H \sim 10^5$–10^6 cm^{-3} for the position M2 (Figure 12 top left). The position A1 has to a similar result. The position A6 has the best agreement at a slightly lower radiation field of $G_0 \sim 10^3$, which is similar to the other positions A2, A4, A5, A7, A8, M3, and M8. Although the observed ranges do not overlap for the position M7, if we allow larger errors considering that the chemical models also have uncertainties in rates, the best agreement should be met around $G_0 \sim 10^{2.5}$ and $n_H \sim 10^5$–10^6 cm^{-3}. Positions A3, M4, M5, M6, M9, and M10 have similar results to M7. If $A_{V,\mathrm{max}}$ from total column densities is used, the observed $\mathrm{HCO^+/HOC^+}$ ratio can be reproduced with a higher G_0, but there is difficulty reproducing sufficiently high $\mathrm{HOC^+}$ fractional abundances. Therefore, if the effective visual extinction is equivalent to that obtained from total column

densities, PDRs can be ruled out. Many molecular clumps with names "M" (from Meier et al. 2015) have the best-fit models with low G_0. The low G_0 implied from chemical models in these clumps may be explained by a large visual extinction.

6.3. The Effects of Cosmic Rays

In addition to UV photons, cosmic rays can enhance the abundance of $\mathrm{HOC^+}$, as already reported by Bayet et al. (2011) and Albertsson et al. (2018). This enhancement is because cosmic rays increase the abundances of $\mathrm{C^+}$ and $\mathrm{CO^+}$, which leads to a faster production of $\mathrm{HOC^+}$ through Reactions (2) and (3). The chemistry of CRDRs is known to be similar to that in XDRs although the heating in XDRs is more efficient than in the CRDRs. The enhancement of $\mathrm{HOC^+}$ in XDRs is also shown in the modeling by Spaans & Meijerink (2007). Here, we examine the effect of varying the cosmic-ray ionization rate. The cosmic-ray ionization rate ζ is expressed in terms of the rate per $\mathrm{H_2}$. This is the total ionization rate including the ionization caused by protons and secondary electrons. In the following, we use $G_0 = 1$ and take results from $A_V = 4$, where the effects of PDRs are negligible. Here, we do not integrate over a range of A_V, but we consider the values for this particular A_V. The model also provides an idea of the chemistry in XDRs. We also note that the cosmic-ray ionization rate is dependent on the column densities because the lower-energy cosmic rays
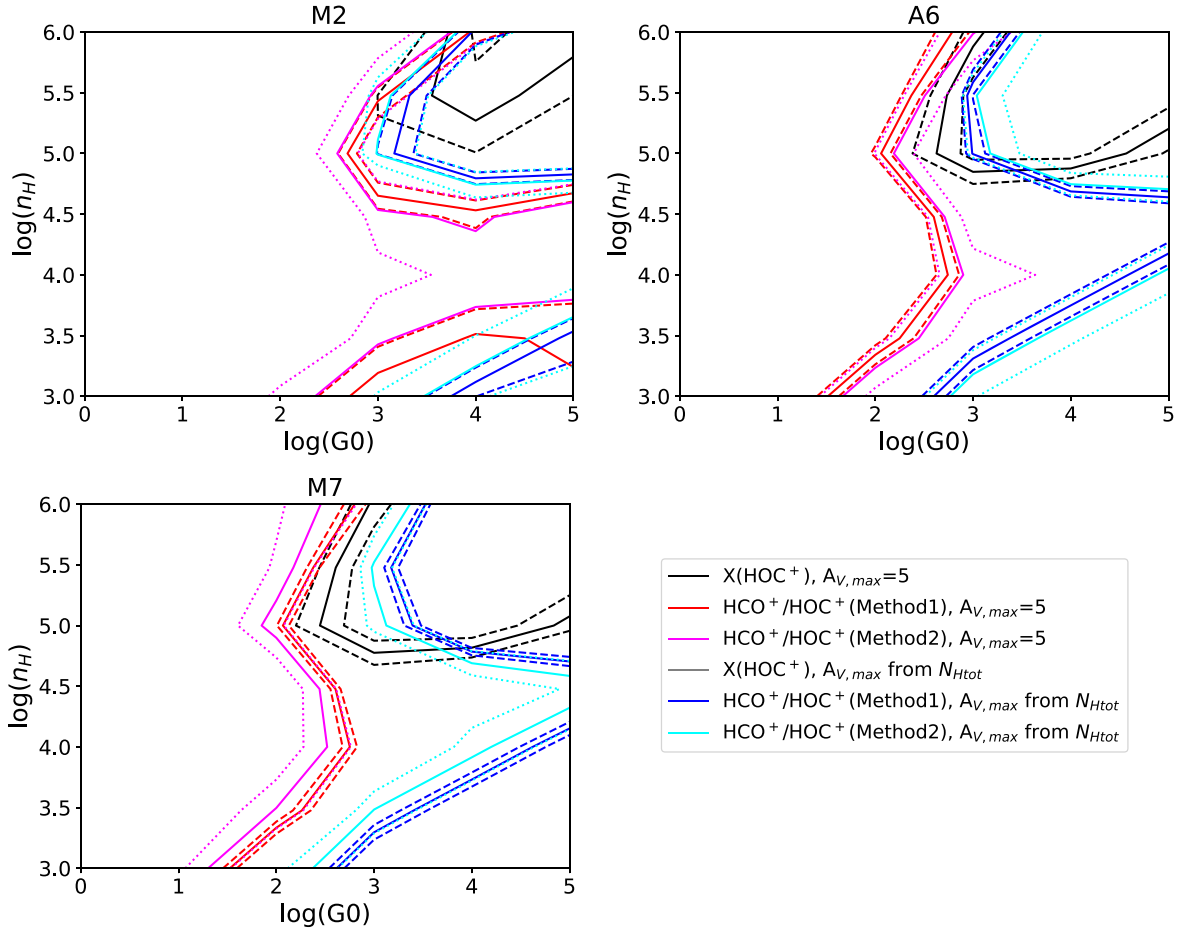
Figure 12. $X(HOC^+)$; (black) and HCO^+/HOC^+ with method 1 (red) and method 2 (magenta) show parameter regions (G_0 and n) where the observed values toward M2 (top left), A6 (top right), and M7 (bottom left) match values in the PDR models for $A_{V,max} = 5$. Solid lines show the observed values while dashed lines (for Method 1) and dotted lines (for Method 2) show the range within errors. Results at positions A3, M4, M5, M6, M9, and M10 resemble that of M7. The same quantities are shown for $X(HOC^+)$; (gray) and HCO^+/HOC^+ with method 1 (blue) and method 2 (cyan) when $A_{V,max}$ is taken from the total column density obtained in Appendix E. Note that none of these positions matches the fractional abundances of HOC^+ with this assumption of visual extinction, and gray lines do not appear in plots.

have a higher ionization cross section, and they become attenuated at lower column densities (e.g., Indriolo et al. 2009; Padovani et al. 2009; Neufeld & Wolfire 2017). However, how exactly the cosmic-ray ionization rate depends on column densities is uncertain in our case where the energy spectrum and the density distribution are uncertain. Therefore, we only show modeled abundances and their ratios as a function of ζ instead of integrating over certain column densities with varying ζ.

Figure 13 (top left) shows the abundance ratios of HCO^+/HOC^+ with varying cosmic-ray ionization rate ζ and density n_H. It is apparent that the abundance ratios vary roughly proportionally to the quantity ζ/n_H, and that the ratio decreases with higher ζ/n_H. The fractional abundance of HCO^+ (Figure 13: top right) peaks when $\zeta/n_H \sim 10^{-20}$–10^{-19} s^{-1} cm^3, although HCO^+ still keeps a moderate fractional abundance $\gtrsim 10^{-9}$ even at lower ζ/n. At high values of $\zeta/n_H \sim 10^{-16}$ s^{-1} cm^3, the medium starts to become atomic, not molecular, and the molecular abundances of almost all of the species tend to decrease. The fractional abundance of HOC^+ peaks when $\zeta/n_H \sim 10^{-17}$ s^{-1} cm^3, at higher ionization rates compared to the peak values of HCO^+ (Figure 13: bottom left). The gas temperature can be as high as >1000 K in low-density, high-ζ environments, but is quite low (<150 K) for

most of the parameter space that we explored. The dust temperature is not shown, as the modeled value was 14.6 K with little variation for all densities and cosmic-ray ionization rates. Unlike PDR regions, the enhancement of HOC^+ in CRDRs does not need a high gas temperature. This is because the formation route of HOC^+ is different from that in PDRs. As discussed in Section 6.1, the high cosmic-ray ionization rate can produce OH and water through the electron recombination of H_3O^+ and H_2O^+. This will lead to HCO^+ and HOC^+ production via Reactions (2) and (3).

Figure 14 shows the same information as in Figure 12, but for CRDR models. In these figures, the observed range of HCO^+/HOC^+ appears very narrow, as this ratio changes drastically near $\zeta/n_H \sim 10^{-19}$–10^{-18} s^{-1} cm^3 in the chemical model while the observational error is only about 20%. At the position M2, observations are reproduced well around $n_H \gtrsim 10^{5.5}$ cm^{-3}, $\zeta \gtrsim 10^{-13}$ s^{-1}. Many positions (A1, A2, A4, A7, A8, M3, M8, M9, and M10) have a good agreement with observations in the same parameter range. Other positions have a good agreement with observations in a similar parameter space as the position M7 (Figure 14 right), when $\zeta/n_H \sim 10^{-18.5}$ s^{-1} cm^3. This includes lower density, lower ζ regions, but does not uniquely constrain the density and cosmic-ray ionization rate. A large velocity gradient (LVG)
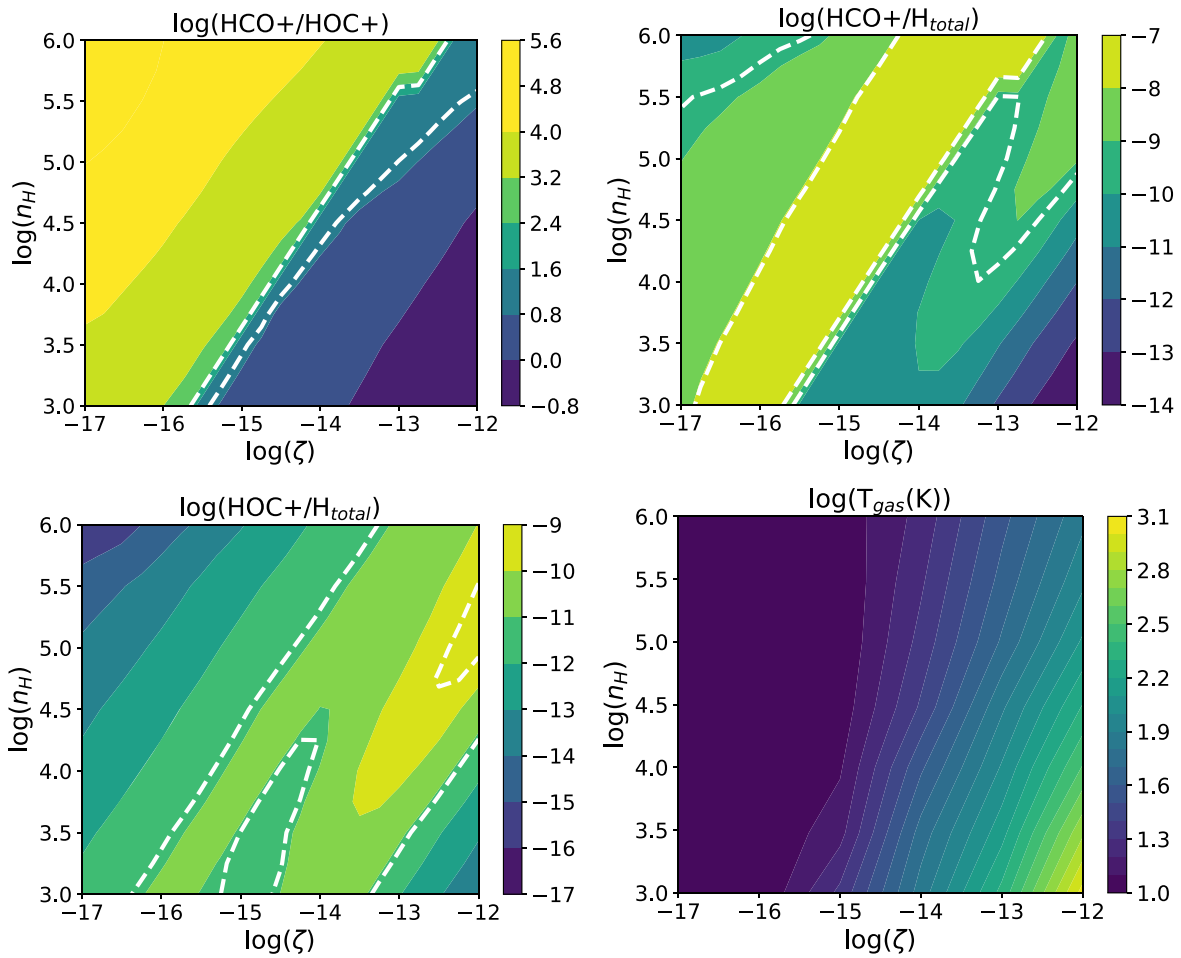
Figure 13. The abundance ratio of HCO$^+$/HOC$^+$ (top left), the fractional abundance of HCO$^+$ (top right), the fractional abundance of HOC$^+$ (bottom left), and the gas kinetic temperature (bottom right). These quantities are shown on a logarithmic scale. The abscissa is the logarithm of cosmic-ray ionization rate ζ s^{-1}, while the ordinate is the logarithm of the density. The ranges of observed values in all analyzed positions are shown as white dashed lines for the HCO$^+$/HOC$^+$ ratio and fractional abundances of HCO$^+$ and HOC$^+$.
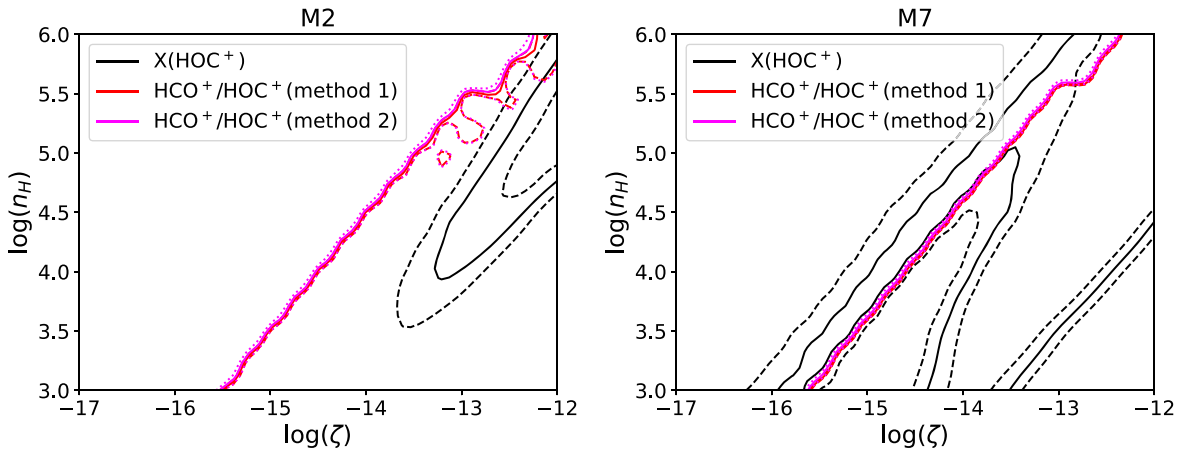
Figure 14. X(HOC$^+$); (black) and HCO$^+$/HOC$^+$ with method 1 (red) and method 2 (magenta) that correspond to the observed values in the CRDR models are shown as a function of ζ and n_H, for positions M2 (left) and M7 (right). Solid lines show the observed values while dashed lines (for Method 1) and dotted lines (for Method 2) show the range within errors.

analysis from our team (Tanaka et al., in preparation) suggests that the density of major molecular clumps (M4–M8) are $\sim 10^5$ cm^{-3}, which suggests $\zeta \sim 10^{-14}$ s^{-1}.

As already discussed, for M2 it appears that the parameters needed to reproduce observations are uniquely constrained to a

high density, high cosmic-ray ionization rate. However, the comparison between the observed X(HOC$^+$), HCO$^+$/HOC$^+$ and the results of the chemical model should be taken with caution. It should be noted that the chemical model has uncertainties related to reaction rates, which are currently not

considered. If larger errors were considered because of these uncertainties, the best-fit parameter could be at a lower density and lower cosmic-ray ionization rate because the HCO^+/HOC^+ ratio varies with ζ/n. Because of the density obtained from the LVG analysis (Tanaka et al. in preparation), it is likely that the cosmic-ray ionization rate is still $\zeta \gtrsim 10^{-14}$ s^{-1}. At the same time, ζ should not be orders of higher than $10^{-14}\,s^{-1}$, due to reasons discussed in Section 7.5.

7. Discussion

7.1. Comparison of Abundance Ratios with Previous Work and Other Sources

Our derived values of $HCO^+/HOC^+ = 10-150$ are overall in agreement with the previous single-dish studies of NGC 253. Martín et al. (2009) derived the HCO^+/HOC^+ ratios of 80 ± 30 and 63 ± 17 for two different velocity components, while Aladro et al. (2015) obtained the HCO^+/HOC^+ ratio of 30. The results of the ALCHEMI survey from ACA data alone (convolved to 15″; Martín et al. 2021) show $HCO^+/HOC^+ = 50$, a result between the two values provided from single-dish observations. Our higher angular resolution study highlights the variation within the region covered by the beam of the single-dish telescope.

As stated in the Introduction, observed values of the HCO^+/HOC^+ ratios are >1000 in quiescent dense clouds, far greater than in NGC 253. Our work suggests similar values to Galactic PDR values ($\sim$100), in diffuse clouds and dense PDRs. The starburst galaxy M82 also has an HCO^+/HOC^+ratio similar to that in NGC 253, showing similarity in the properties of the ISM in these two local starburst galaxies. Despite being another galactic center and having a high cosmic-ray ionization rate ($\zeta \sim 10^{-15}\,s^{-1}$), the range of HCO^+/HOC^+ ratios in the Sgr B2 clouds near the Galactic Center is 300–1500 (Armijos-Abendaño et al. 2020), at least a factor of a few higher than values obtained in NGC 253. Among the ratios obtained in the CMZ of NGC 253, lower ratios are close to that suggested by Aalto et al. (2015) and Aladro et al. (2018) from the intensity ratio of $HCO^+/HOC^+(J = 3–2) \sim 10$ toward the quasars Mrk 231 and Mrk 273. If these lines are optically thin and these species have the same excitation temperatures, the HCO^+/HOC^+ abundance ratios would be 5. Contributing factors to these ratios are discussed in the following subsections.

7.2. Derived Physical Parameters

In Section 6, we have constrained physical parameters such as G_0 and ζ in PDR and CRDR models. We discuss those parameters in comparison with other sources here.

Relatively high values of the interstellar radiation field $G_0 \sim 10^3$ are suggested from models in Section 6.2 for the case of $A_{V,max} = 5$. While this value is higher than the Galactic interstellar radiation field ($G_0 = 1$), it is not high compared with a strong PDR such as the Orion Bar ($G_0 = 3 \times 10^4$; Marconi et al. 1998). It should be noted that our beam size of 27 pc is much larger than the size of the Orion Bar, and extreme PDRs may have a smaller beam filling factor in our beam. That said, as discussed in Section 6.2, $A_{V,max}$ may be much larger than 5, and the actual G_0 may be 10^4–10^5.

The high value of cosmic-ray ionization rate we derived in Section 6.3 is consistent with another work from our team that

concluded that $\zeta > 10^{-14}$ s^{-1} because C_2H is somewhat abundant even in extremely high A_V regions (Holdship et al. 2021). The derived value of the cosmic-ray ionization rate is higher than those usually obtained in our Galaxy. The cosmic-ray ionization rate in the Galactic spiral arm dense clouds was found to be around $(1–5) \times 10^{-17}$ s^{-1} (van der Tak & van Dishoeck 2000), while this value can be an order of magnitude higher for diffuse clouds (Indriolo & McCall 2012). However, in the Galactic Center, an orders of magnitude higher ζ has been inferred. Observational results from diffuse clouds in the Galactic Center using H_3^+ tend to be higher than those from dense clouds, with $\zeta \gtrsim 10^{-14}\,s^{-1}$ (Goto et al. 2014; Oka et al. 2019). The values in dense clouds are $\zeta = (3–10) \times 10^{-16}$ s^{-1} (van der Tak et al. 2016; Bonfand et al. 2019), although a higher value of $\zeta \gtrsim 10^{-15}\,s^{-1}$ is possible within several parsecs of the Galactic Center even in dense clouds (Harada et al. 2015). The high cosmic-ray ionization rate of $\zeta \sim 10^{-15}\,s^{-1}$ is also found in a molecular cloud in the vicinity of the supernova remnant W51C (Ceccarelli et al. 2011). High values of the cosmic-ray ionization rate of $\zeta = 2 \times 10^{-14}$–$3 \times 10^{-15}$ s^{-1} were found in two lines of sight in the $z = 0.89$ molecular absorber toward the quasar PKS1830-211 (Muller et al. 2016). Although it is not possible to compare directly between CMZs of the Milky Way and NGC 253, the higher ζ in NGC 253 is reasonable considering the difference in the star formation rate of a factor of 20 ($0.1\,M_\odot\,yr^{-1}$ in the Milky Way CMZ; Longmore et al. 2013).

In both PDR and CRDR models, our results suggest high densities of $n \sim 10^5$–10^6 cm^{-3}. This is consistent with densities obtained for the central molecular clumps with dust observations by Leroy et al. (2018; $n_H \sim 4 \times 10^5$ cm^{-3}). Although our beam sizes of 1″6 are larger than their 0″2 beam, HCO^+ and HOC^+ emission are likely originating from these dense clumps within our beam.

7.3. Association of HCO⁺/HOC⁺ with Superbubbles

The moment 0 image of $HOC^+(1-0)$ shows differences from $HCO^+(1-0)$ at locations related to some of the superbubbles (Figures 1 and 2). It is not known whether these superbubbles are produced from expanding H II regions or supernovae for most of the sources. The spectral indices of radio observations are often used to distinguish between supernovae emitting synchrotron radiation and H II regions causing free–free emission with the spectral indices of ~-0.7 and ~-0.1, respectively. From the spectral index, it is suggested that a radio source at the superbubble southwest of M2 is produced from a supernova remnant (Figure 2). Although this is a useful measure for young and small superbubbles, the temperature of a bubbles cools down as it ages and expands, making it difficult to observe. Therefore, some superbubbles do not have corresponding radio sources (e.g., the bubbles southeast of M2 and one near A1). Another cause of difficulty in separating H II and supernova remnants is that many different sources are gathered in the CMZ of NGC 253. In crowded regions, there are multiple radio sources close to each other, making it difficult to know which particular radio source is causing the superbubble. This applies to the case of the superbubble right beside M5, where the neighboring radio sources are identified as H II regions or "unknown." The dominant driving force of chemistry depends on the cause of the superbubbles.

Position M2 is the location with one of the lowest HCO^+/HOC^+ ratios (~ 14). It has a superbubble nearby as shown in Figure 2. In a position slightly southwest from M2, there is a supernova remnant (Figure 2 bottom). A position with a similarly low $HCO^+/HOC^+ \sim 15$, A1, also has a shell-like structure likely associated with a superbubble according to higher-resolution observations by Krieger et al. (2019). We are not able to detect this bubble because this bubble is too small and its shell is too thin to be detected by our beam.

Morphologically, $HOC^+(1-0)$ also appears to have an association with the superbubble near the position M5 (Figure 2). At this position, the HCO^+/HOC^+ ratio is around 100. There, HOC^+ also shows the hole-like structure that is seen in the channel map of CO data around $v = 293$ km s^{-1} ($+50$ km s^{-1} from v_{sys}). The position M5 coincides with the hard X-ray source X-2 in Müller-Sánchez et al. (2010) with the luminosity of $L_{2-10 \text{ keV}} \sim 10^{38}$ erg s^{-1}. This area also has emission in soft X-rays, stretched toward the center of the superbubble. M5 is located in the northwestern part of the superbubble shell. This is not the point where the HCO^+/HOC^+ ratio is low in comparison with other positions in NGC 253 CMZ. This may be because multiple unresolved components are included in this position, and the enhancement of HOC^+ around the superbubble does not necessarily show up in the ratio. That said, it is also possible that HOC^+ is not enhanced in this position. The southeast part of this bubble, A4, has a lower ratio of HCO^+/HOC^+ than M5, around 40.

While an enhancement of HOC^+ is suggested near the superbubble from M2 positions, the observed HCO^+/HOC^+ ratio in M5 near the superbubble makes it less conclusive. However, the position M5 may have multiple components in the line of sight, and HOC^+ may be enhanced near the superbubble.

7.4. PDR, CRDR, or XDR?

Our modeling results show that HOC^+ can be enhanced both with PDRs and CRDRs, and that neither scenario can be ruled out simply from the observed values of HCO^+/HOC^+ or the fractional abundances of HOC^+. The chemistry of XDRs is very similar to that of CRDRs, so it is expected that an XDR can also reproduce the observed ratios and abundances. In fact, the HCO^+ fractional abundance in our CRDR model peaks at $\zeta_{CR}/n = 10^{-19}$ s^{-1} cm^3, similar to that in the XDR model by Lepp & Dalgarno (1996).

We note here that PDRs and CRDRs are products of star formation, and both regions are expected to exist in a starburst galaxy like NGC 253. Gong et al. (2017) proposed a following approximation for the relationship between the UV radiation field and cosmic-ray ionization rate: $\zeta = 1.8 \times 10^{-16}\sqrt{G_0}$ s^{-1}. According to this relationship, $\zeta \sim 2 \times 10^{-14}$ s^{-1} if $G_0 = 10^4$. These values of G_0 and ζ are similar to values needed to reproduce our observational results. Therefore, it is likely that the CMZ in NGC 253 is affected by the combination of these levels of the interstellar radiation field and cosmic-ray ionization rates. At the same time, we also expect that there is a deviation from the above relationship by Gong et al. (2017) in our observed regions, because this relationship is derived as a general behavior of the ISM. Depending on the distance from star clusters and supernova remnants, a region may be more affected by UV photons or cosmic rays.

In an attempt to distinguish which scenario might be suitable for the case of the CMZ of NGC 253, we could use constraints from the physical parameters. For example, models by

Meijerink et al. (2007) did not predict very low ratios of HCO^+/HOC^+ in their PDR models, partly because they made some assumptions about standard clouds. For dense clouds, they chose the cloud size to be 1 pc, which corresponds to $N_H = 3 \times 10^{23}$ cm^{-2} ($A_V = 160$ mag) for the density $n_H = 10^5$ cm^{-3}. After integrating to this A_V, the HCO^+/HOC^+ ratio becomes very high, as already discussed in Section 6.2. Therefore, whether PDRs are the major sources of the observed HOC^+ or not highly depends on the effective visual extinction. The value of effective visual extinction is most affected by the lowest visual extinction in all of the directions, and can get significantly lower than the line-of-sight visual extinction when the medium is clumpy or filamentary. We consider the presence of such a clumpy medium is possible and do not exclude PDRs even in the clumps with high column densities ($N_{H_2} \sim 10^{24}$ cm^{-2}).

X-rays can also produce HOC^+. Müller-Sánchez et al. (2010) show three hard X-ray sources in the CMZ of NGC 253 (Figure 2 middle). Of them, X-1 has the highest luminosity ($L_{2-10 \text{ keV}} = 10^{40}$ erg s^{-1}), but this is the position close to TH2, which is excluded from our analysis due to the absorption. Other sources have the luminosities $L_{2-10 \text{ keV}} \sim 10^{38}$ erg s^{-1}, and this level of luminosity can contribute to the X-ray ionization rate $\zeta_X \sim 10^{-15}$ s^{-1}, if we use the approximation formula (Maloney et al. 1996) as follows

$$\zeta_X = 1.4 \times 10^{-15} \frac{L_X}{10^{38} \text{ erg s}^{-1}} \left(\frac{r}{10 \text{ pc}}\right)^{-2}$$

$$\times \left(\frac{N}{10^{22} \text{ cm}^{-2}}\right)^{-1}. \quad (11)$$

Here, L_X is the X-ray luminosity, r is the distance from the X-ray source, and N is the column density from the X-ray source. Note that the observed X-ray luminosity was derived assuming an obscuring column density of $N = 10^{22}$ cm^{-2}. Since our beam size is 27 pc, this level of luminosity can exceed the ionization by cosmic rays locally, but not on a large scale. Therefore, we suggest that X-rays do not significantly contribute to the overall abundance of HOC^+.

One possible way to differentiate PDRs and CRDRs is from excitation. In PDRs, high temperatures are achieved in high-density regions. This high temperature is necessary for the main route to form HOC^+ because the efficient water production plays a key role (Equations (4) and (5)). In such high-temperature and high-density regions, we expect excitation temperatures of molecules to be very high. High kinetic temperatures of ~ 300 K have been derived by Mangum et al. (2019) from the excitation of multiple H_2CO transitions in all of the major molecular clumps, namely, positions M4−8. The density of molecular clumps is also high ($n \gtrsim 10^5$ cm^{-3}), while the density of the extended part of the CMZ is lower ($n_H \sim 10^{4.5}$ cm^{-3}) from the LVG analysis by our team (K. Tanaka, in preparation). Meanwhile, the formation route of HOC^+ in CRDRs does not require a high temperature nor a high density, which means that it can have a low excitation. The high excitation does not exclude CRDRs, but it seems necessary that a low HCO^+/HOC^+ ratio and a high fractional abundance of HOC^+ in PDRs implies a high excitation. In our moment 0 images of HOC^+, there are regions with the detection of only the $J = 1-0$ transition, while there are other regions with detections of all three transitions. This difference

in excitation may have resulted from different chemical scenarios. In fact, the regions where higher-J transitions of HOC$^+$ are detected correspond well to the 3 mm continuum peaks in the image shown in Appendix D. Unfortunately, there are no collisional coefficients available for HOC$^+$ (F. van der Tak 2021, private communication), and we are unable to conduct the quantitative examination of this proposed method of distinguishing scenarios. Once such data are published, radiative transfer calculations from each scenario would be helpful in deciding whether we can indeed use excitation for differentiating scenarios. We note that the difference in excitation is already seen with different excitation temperatures between molecular clumps such as M5 and M7 (15–20 K) and other positions $T_{ex} < 10$ K (Table 4).

7.5. High Cosmic-Ray Ionization Rate and C I/CO Ratio

The extremely high cosmic-ray ionization rates of $\zeta \gtrsim 10^{-14}$ s^{-1} we derived can pose challenges in retaining enough CO. It has been proposed that at high cosmic-ray ionization rates, most of the carbon in the molecular clouds will be in the form of C I instead of CO (Bisbas et al. 2017). This is not the case for NGC 253, as there is still a large amount of CO. The observations of C I in NGC 253 (Krips et al. 2016) show the abundance ratio [C I]/[CO] to be 0.5–1, which means that the CO abundance is equivalent to or larger than that of C I. Here, we shall check our derived value of the cosmic-ray ionization rate is consistent with C I and CO observations. Figure 15 shows the ratio C I/CO with varying ζ and n in our chemical model. The value of $\zeta \sim 10^{-13}$ s^{-1} and $n_H \sim 10^5$ cm^{-3} is in agreement with the observed value of [C I]/[CO] near unity. However, if this high value of ζ is widespread, most of the molecular mass will be in atomic carbon instead of in CO in the lower density regions. Because C I and CO can both be excited relatively easily, it is expected that most of the molecular mass traced by C I and CO has a low density ($n_H \lesssim 10^4$ cm^{-3}). Therefore, if the enhancement of HOC$^+$ is caused by the high value of ζ, we claim that the enhancement of ζ should be relatively localized. Although this is somewhat against the common conception that cosmic rays should penetrate into high column density gas, lower-energy cosmic rays can increase ζ in a relatively localized way due to the higher ionization cross section at lower energy, only affecting low column density regions (e.g., Padovani et al. 2009). In addition, on average, the value of the cosmic-ray ionization rate should not exceed 10^{-14} s^{-1} by orders of magnitude to retain enough CO.

7.6. Outflows: an Alternative Formation Mechanism for HOC$^+$

We have explored the effects of UV photons and cosmic rays on HOC$^+$, but an alternative scenario is also possible. For example, outflows can provide a high abundance of H$_2$O by heating the gas and produce ionization that leads to C$^+$ by creating an outflow cavity that allows the ionization source (cosmic rays or UV photons) to travel further. This may be the case for Mrk 231, where there seems to be an association between a radio jet and an off-nuclear HOC$^+$. It is unlikely that all of the HOC$^+$ emission in our observations is affected by the outflow because HOC$^+$ is detected in molecular clumps as well. However, it is also possible that there is some contribution from outflows as the HCO$^+$/HOC$^+$ratio becomes lower with higher galactic latitude.
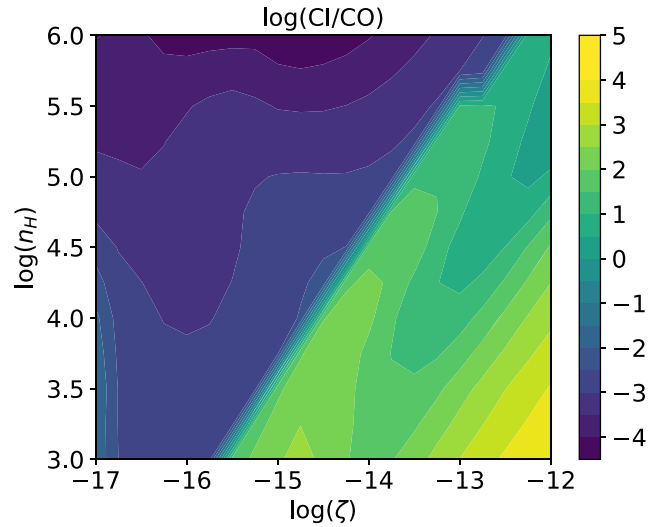

Figure 15. Ratio C I/CO as a function of ζ and n.

8. Summary

We have used the high-sensitivity imaging spectral scan from the ALCHEMI Large Program to investigate the abundance ratios between HCO$^+$ and its metastable isomer HOC$^+$. These measurements have allowed us to study the abundances of HCO$^+$ and HOC$^+$ within the CMZ of NGC 253 and their relationship with photodissociation regions or cosmic rays in the galactic center of this starburst galaxy. Our main findings are as follows.

1. The HOC$^+$(1−0) emission shows significantly different distribution from HCO$^+$ or H^{13}CO$^+$ $J = 1$−0 emission toward a few superbubbles identified in CO data. This association of HOC$^+$ emission with superbubbles has never been observed previously.

2. The observed abundance ratios of HCO$^+$/HOC$^+$ range from ∼10 to 150. This is 1−3 orders of magnitude lower than the ratios seen toward quiescent dense clouds or even some of the PDRs in the Galaxy, indicating physical and chemical processes by energetic photons or cosmic-ray particles enhancing HOC$^+$. The ratio is low near the position of the western superbubble (position M2) and another superbubble in the southwest part of the CMZ (A1). By contrast, the ratios are higher at the centers of molecular clumps (e.g., position M5), which may be due to the higher density or high column density.

3. We derived the fractional abundances of HOC$^+$ to be [HOC$^+$]/[H$_{total}$] = (0.7–30) × 10^{-11} ([HOC$^+$]/[H$_2$] = (1.5–60) × 10^{-11}). This is equivalent to or higher than Galactic PDR values.

4. We ran models of PDRs to see what mechanism is likely producing the observed abundance ratios [HCO$^+$]/[HOC$^+$] and the fractional abundances. The PDR models produce high fractional abundances of HOC$^+$ and a low ratio of HCO$^+$/HOC$^+$ when the density is high ($n_H \gtrsim 10^5$ cm^{-3}) and the interstellar radiation field $G_0 \sim 10^{2.5}$–$10^{3.5}$ if we assume $A_{V,max} = 5$. For a higher $A_{V,max}$, higher values of G_0 reproduce the HCO$^+$/HOC$^+$ratios, but cannot reproduce high enough HOC$^+$ fractional abundances.

5. In addition to PDRs, we also ran models of CRDRs. If HOC$^+$ is enhanced due to cosmic rays, our models suggest the cosmic-ray ionization rate $\zeta \gtrsim 10^{-14}$ s^{-1}. It is about

3–4 orders of magnitude higher than for the Galactic spiral arm dense clouds, and 2 orders of magnitude higher than for the Galactic Center dense cloud values.

6. In our PDR models, the formation of HOC^+ with a high abundance requires a high temperature, high-density environment. By contrast, such conditions are not required in models for cosmic-ray dominated regions. Therefore, we suggest that the region traced by a high luminosity of $HOC^+(1-0)$ is caused by cosmic rays, while regions traced by higher-J transitions of HOC^+ can be caused by either PDRs or CRDRs.

These analyses of HOC^+ have shown that this molecule can be used to study feedback in the starburst ISM.

Appendix A
Estimation of Noise in Velocity-integrated Intensity Images

The rms noise level of our velocity-integrated intensity images (moment 0 images) varies over the image because we masked out the regions in velocity and position space where no significant emission is expected. These noise levels can be estimated by

$$\sigma = \sigma_{1ch}\sqrt{N}\,\Delta v, \qquad (A1)$$

where σ is the rms noise of the velocity-integrated intensity image at a certain pixel, σ_{1ch} is the rms of a single channel, N is the number of channels integrated in the moment 0 image, and Δv is the velocity resolution of a single channel. The resolution of the data in this work is Δv of 10 km s^{-1}. The number of channels used to integrate for each position is shown in Figure 16. From this image, we used $N = 40$ to obtain a typical error of the image to draw contours in Figure 1. Although there are regions with $N \gtrsim 50$, those regions have a high enough S/N, and there is no doubt about the detection there. The rms of a single channel for each image is shown in Section 2.
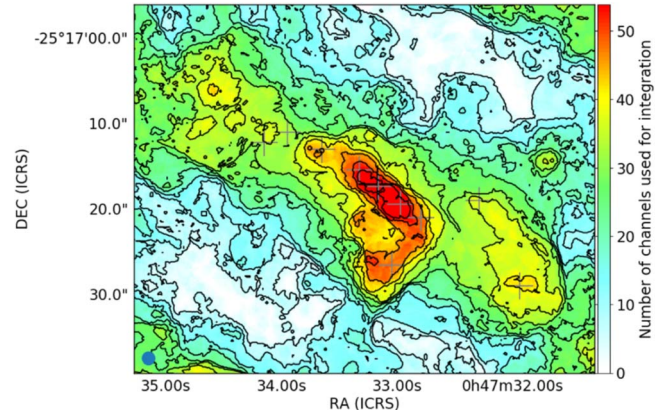

Figure 16. Number of channels used for integration.

Appendix B
Spectra at Selected Positions

In Figures 17–31, spectra of HCO$^+$, H^{13}CO$^+$, and HOC$^+$ at $J = 1$–0, 3–2, and 4–3 transitions are shown for positions that were not shown in Figures 5 or 6.
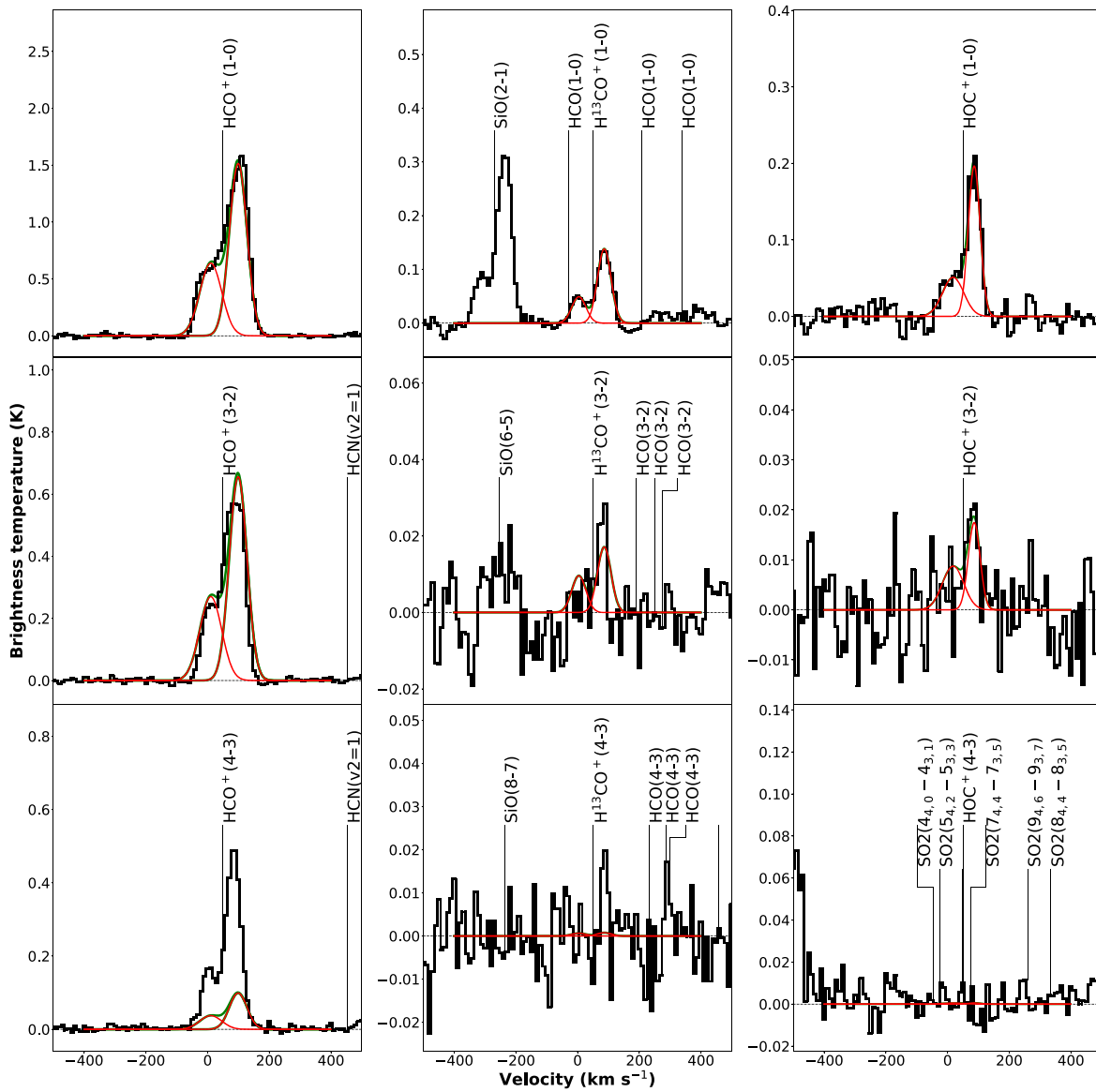

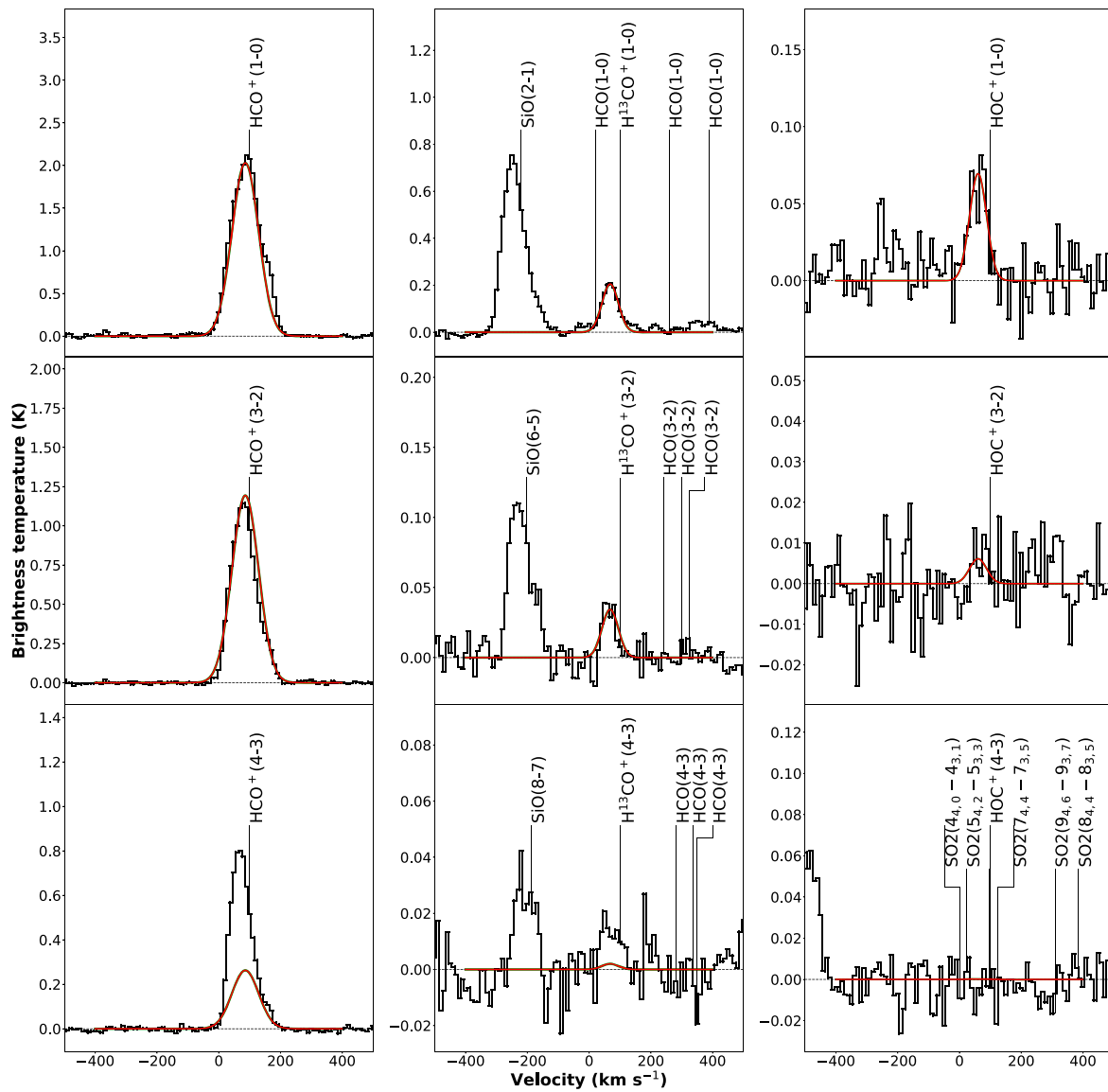**Figure 17.** Spectra at position M2.
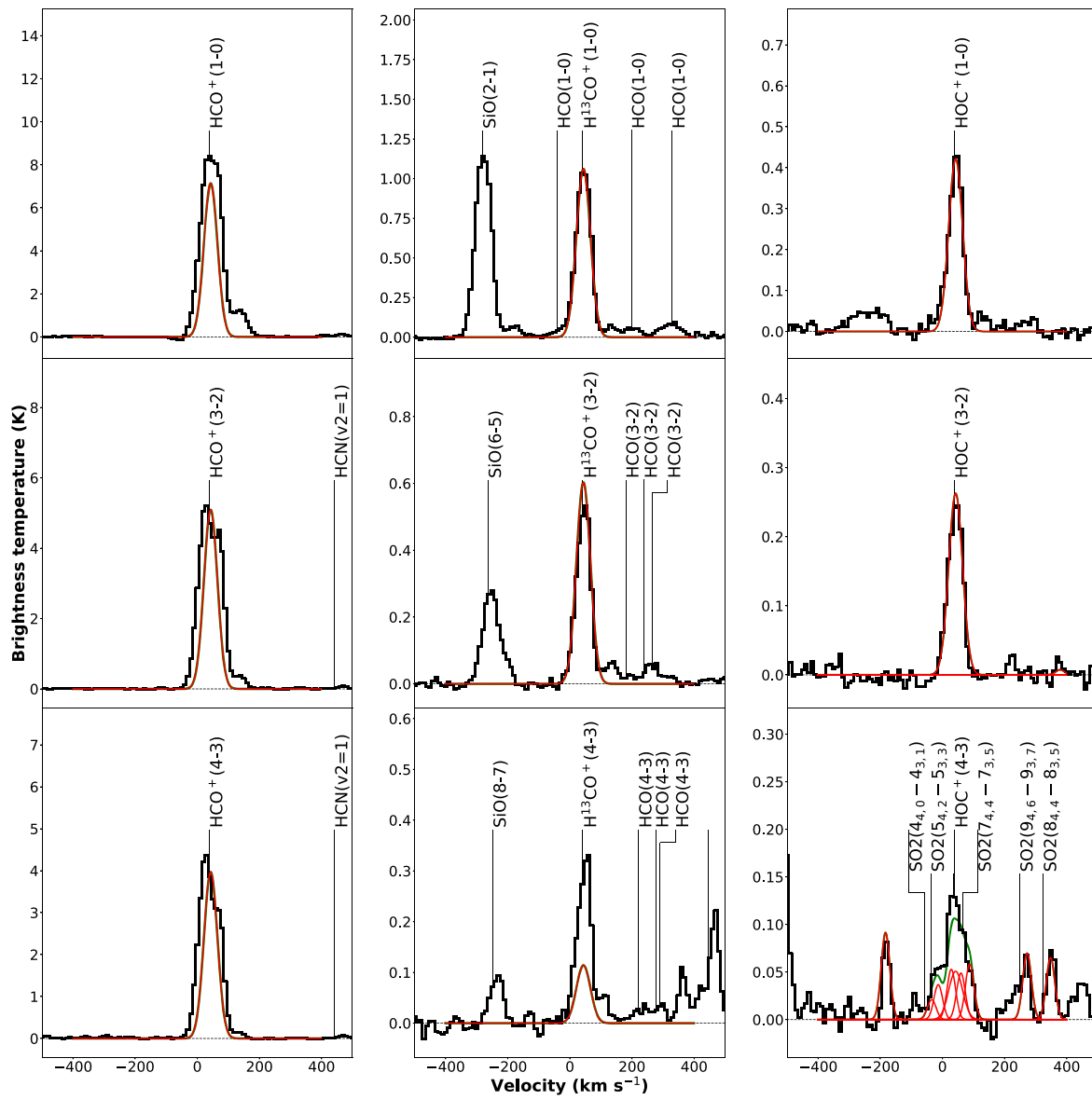
Figure 18. Spectra at position M3.
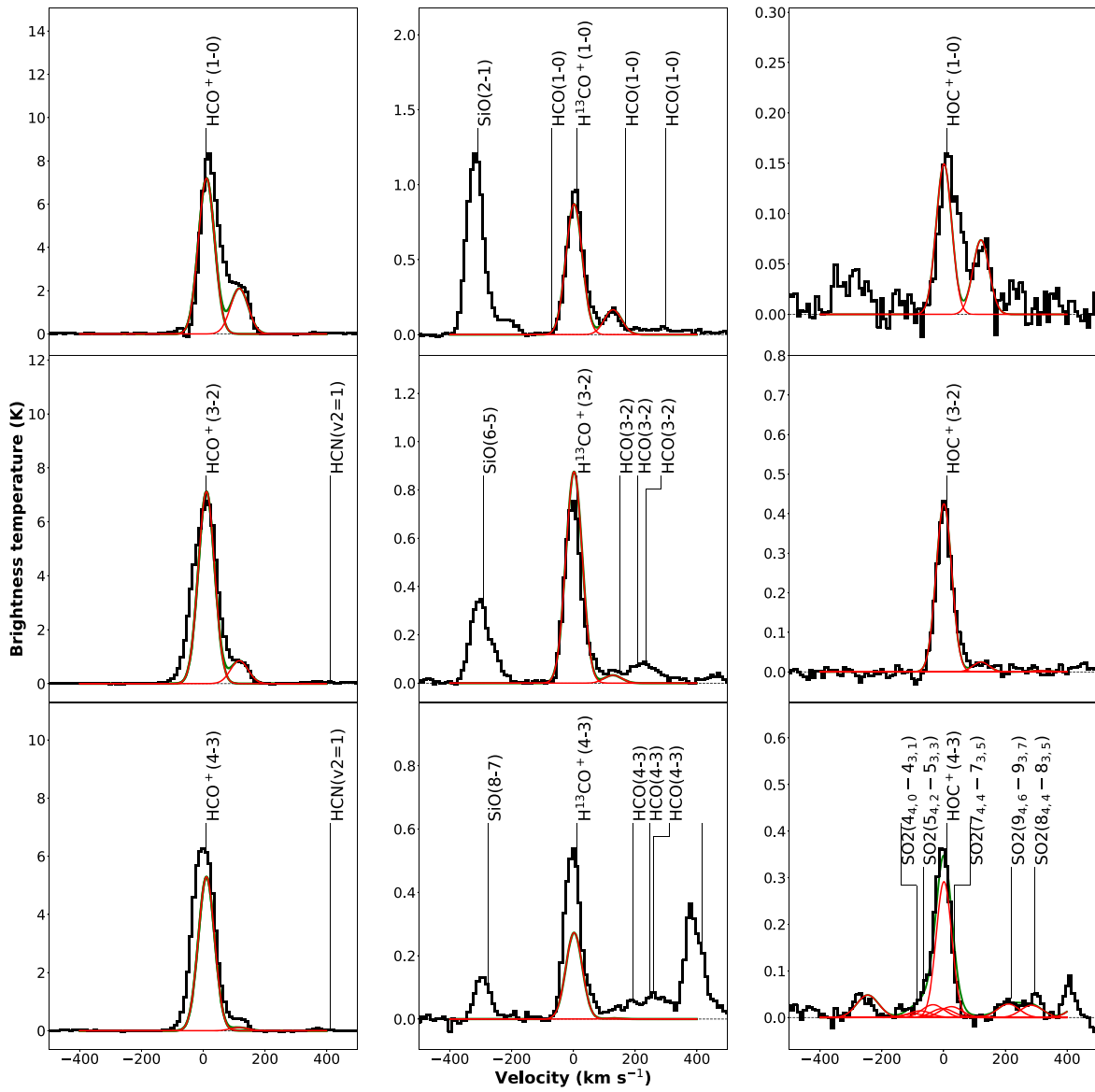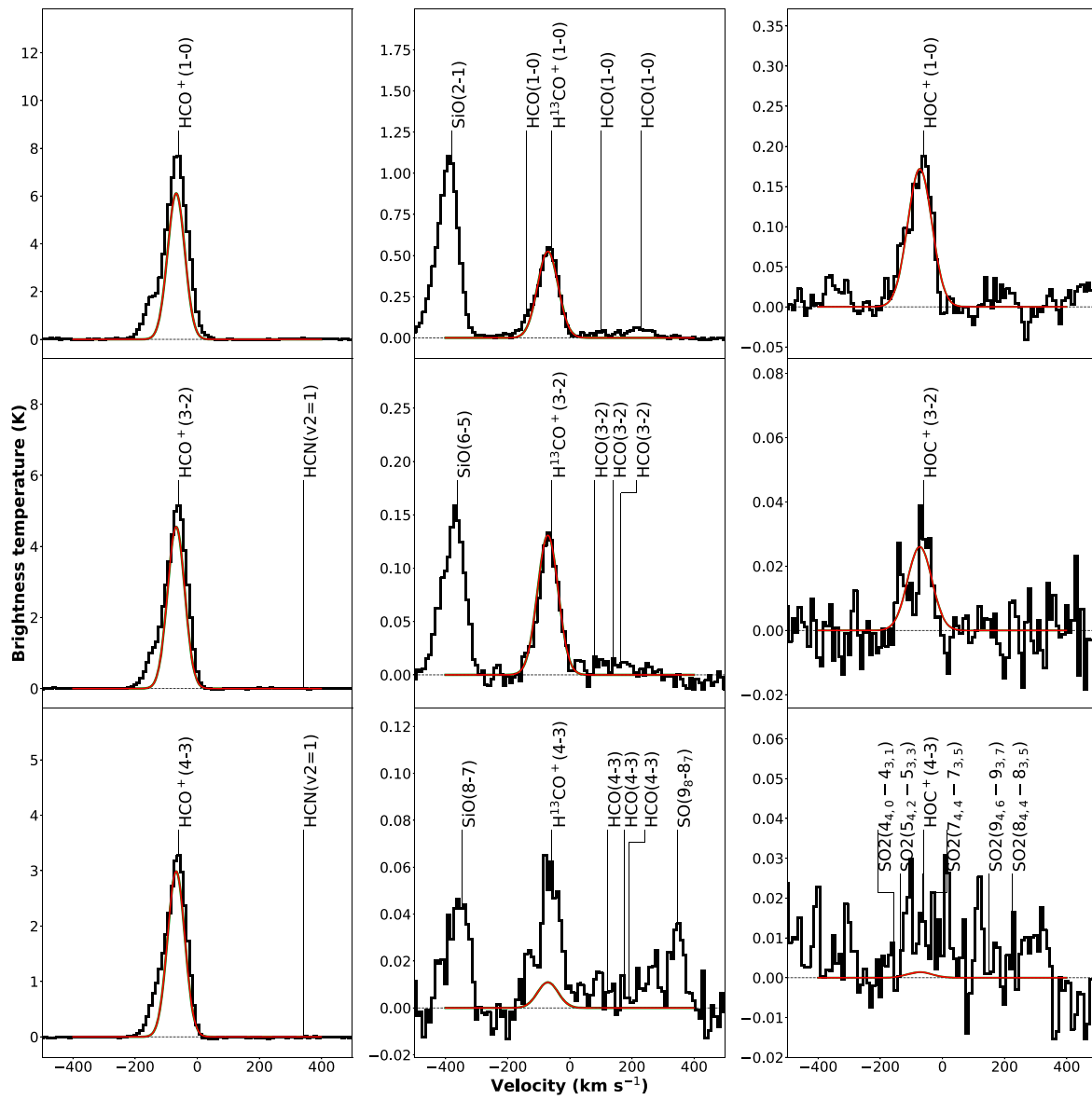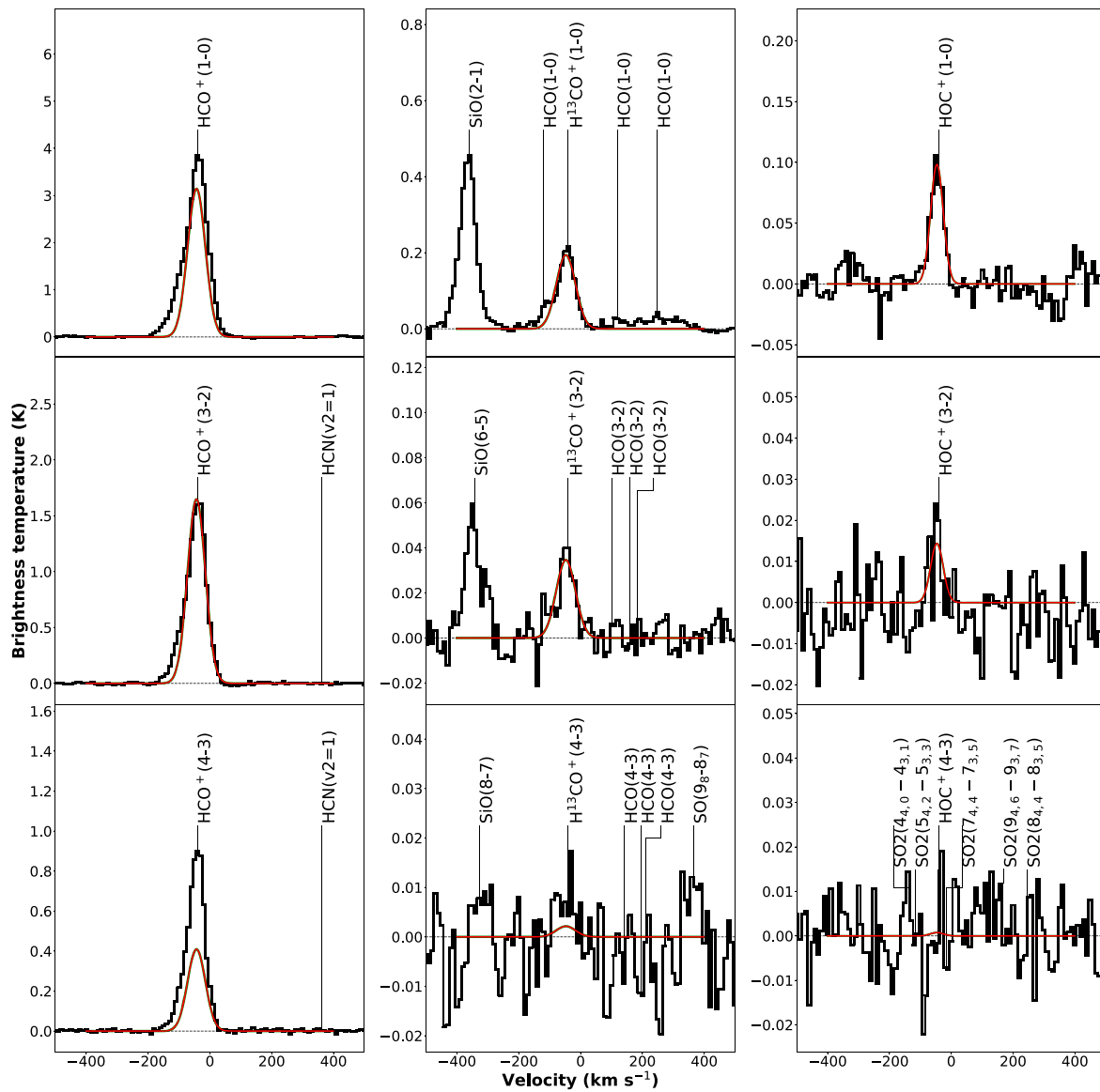
Figure 19. Spectra at position M4.

Figure 20. Spectra at position M5.

Figure 21. Spectra at position M8.

Figure 22. Spectra at position M9.
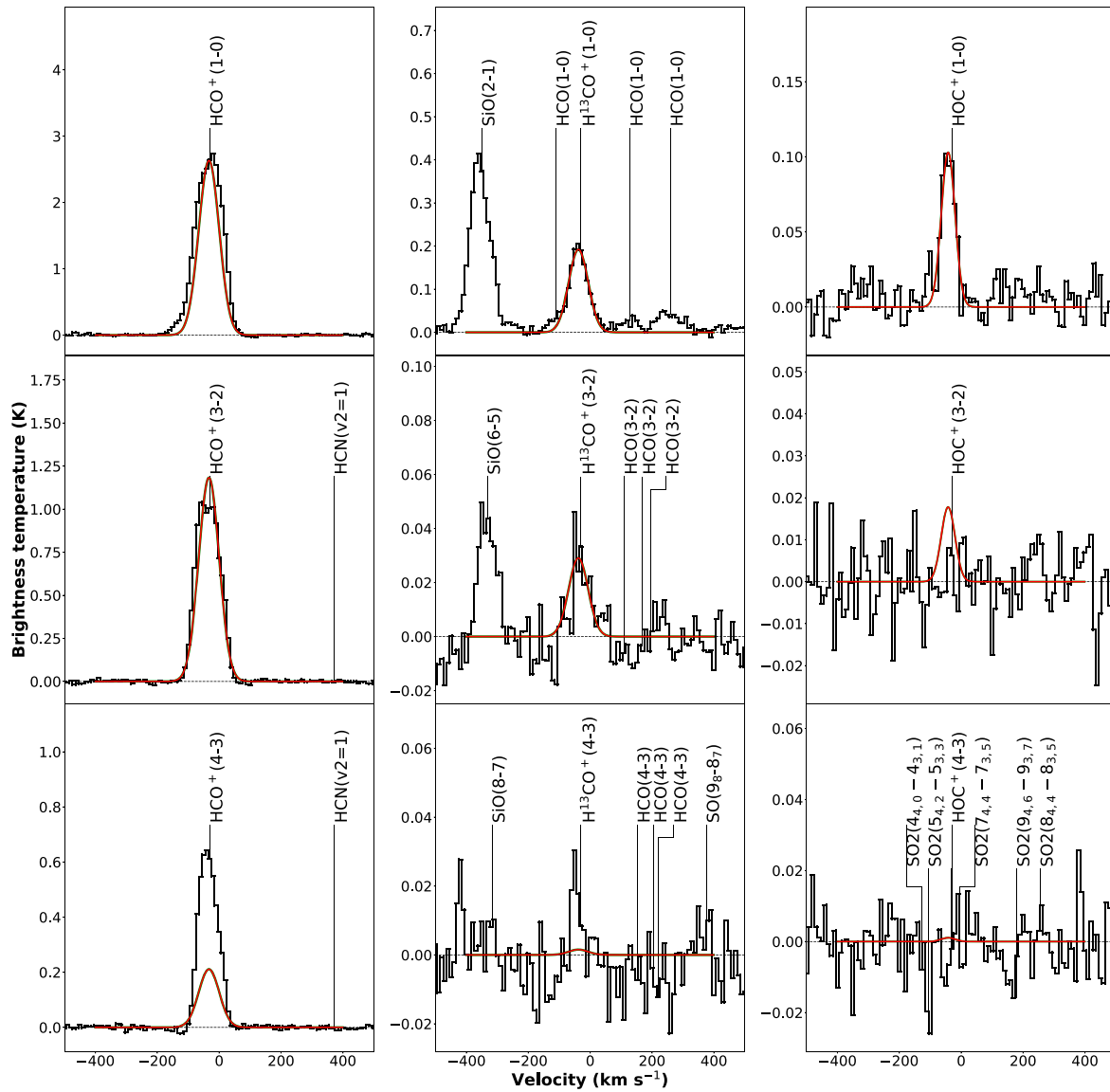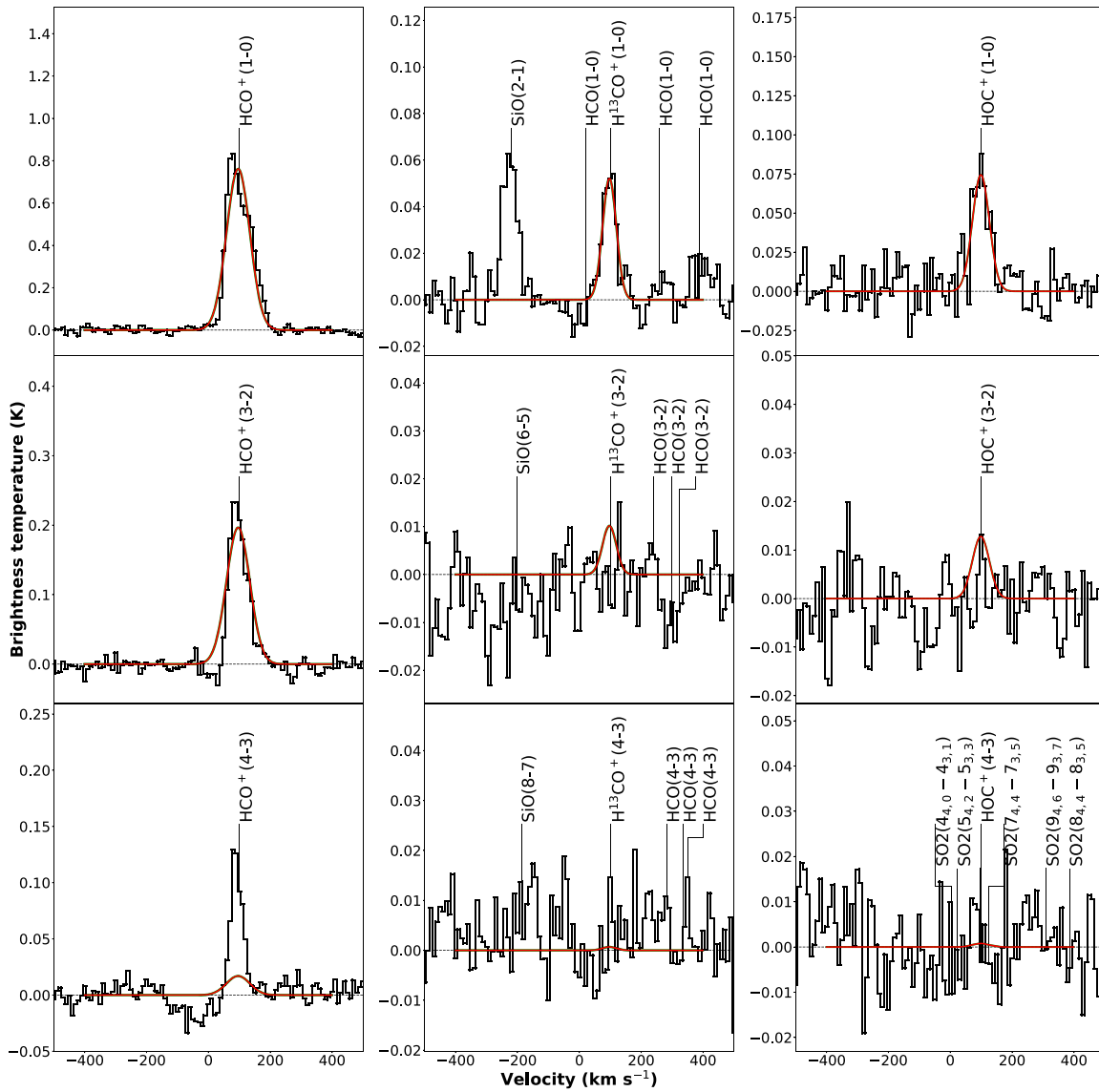
Figure 23. Spectra at position M10.
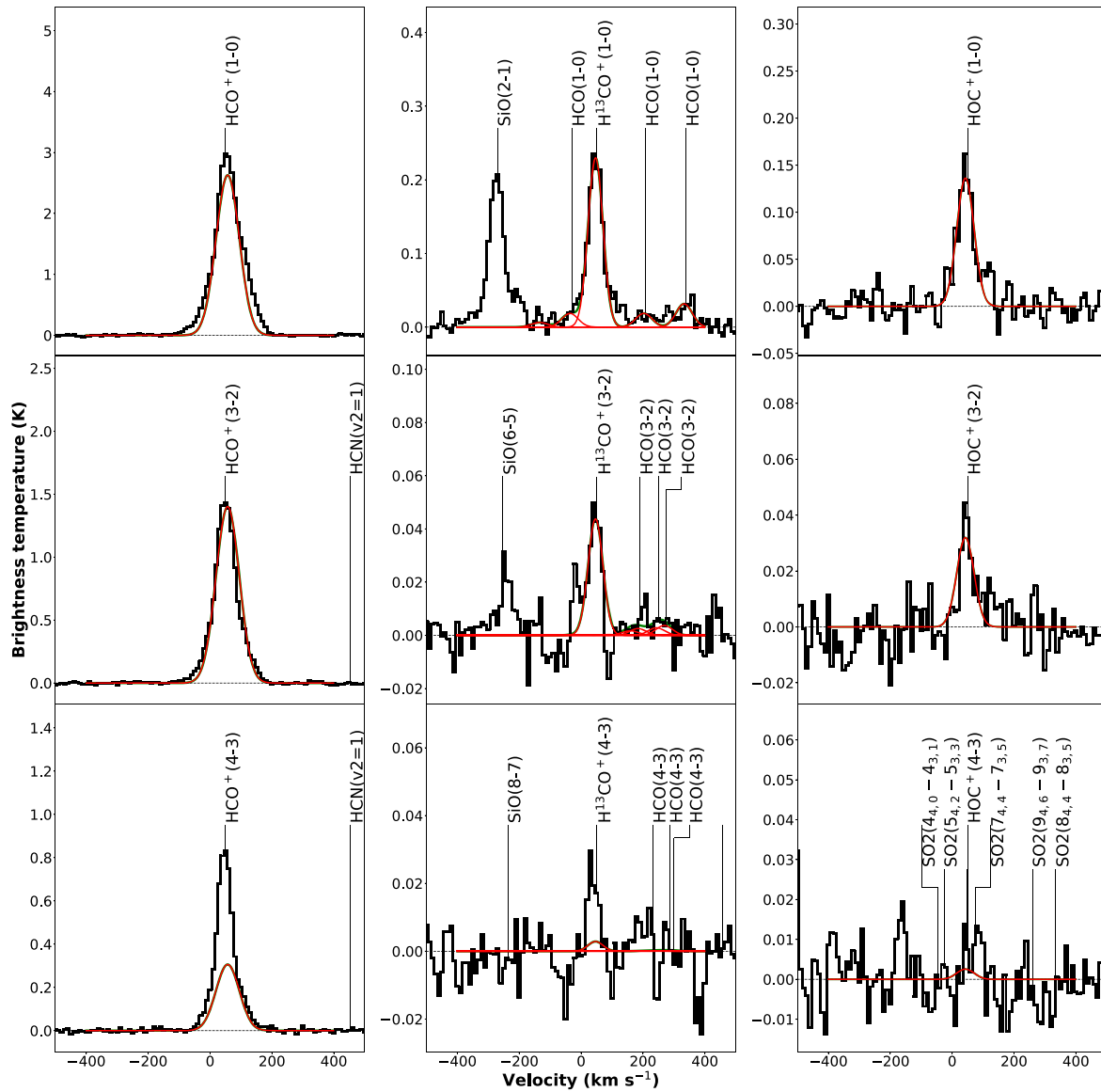
Figure 24. Spectra at position A1.
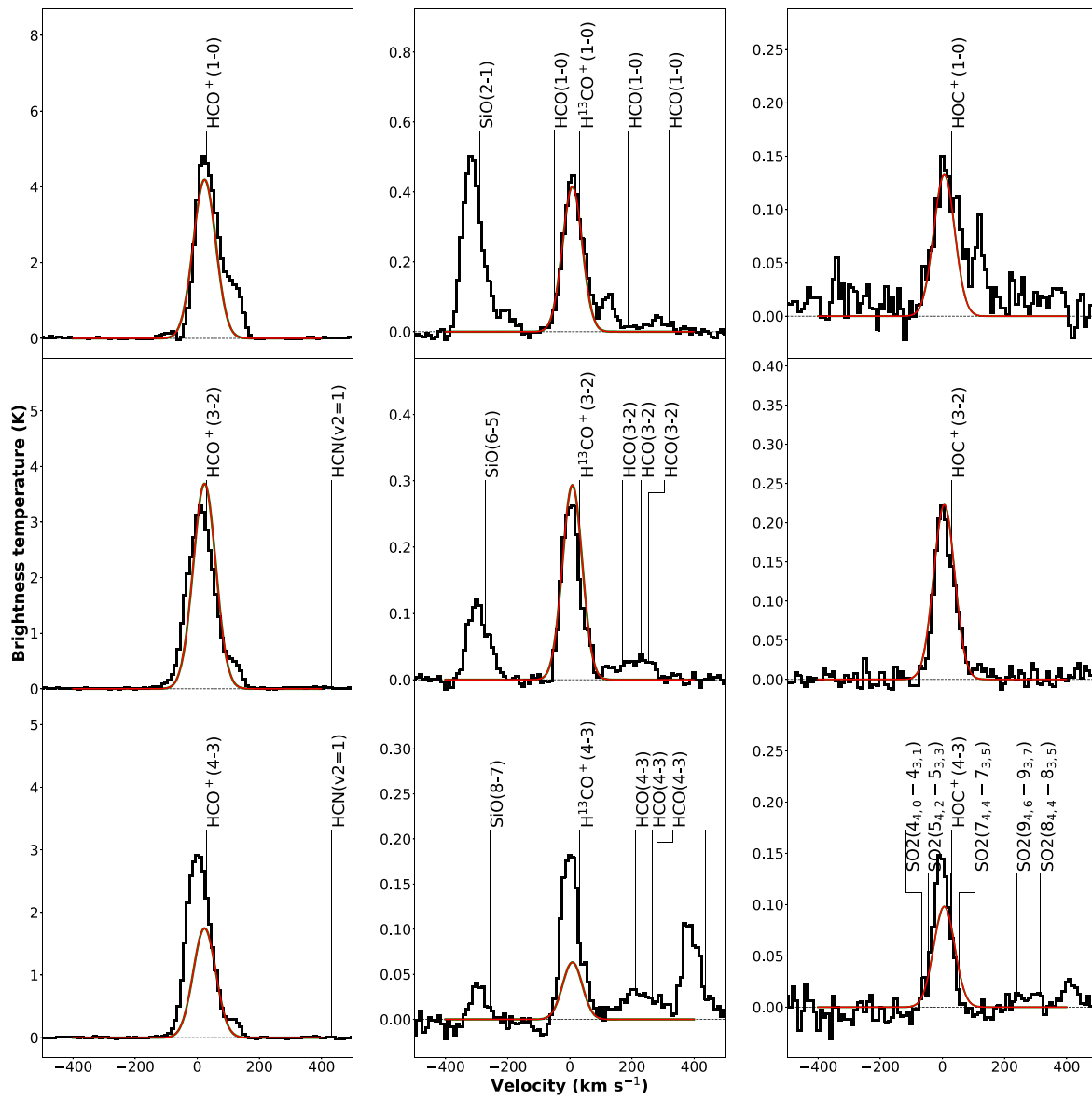
Figure 25. Spectra at position A2.
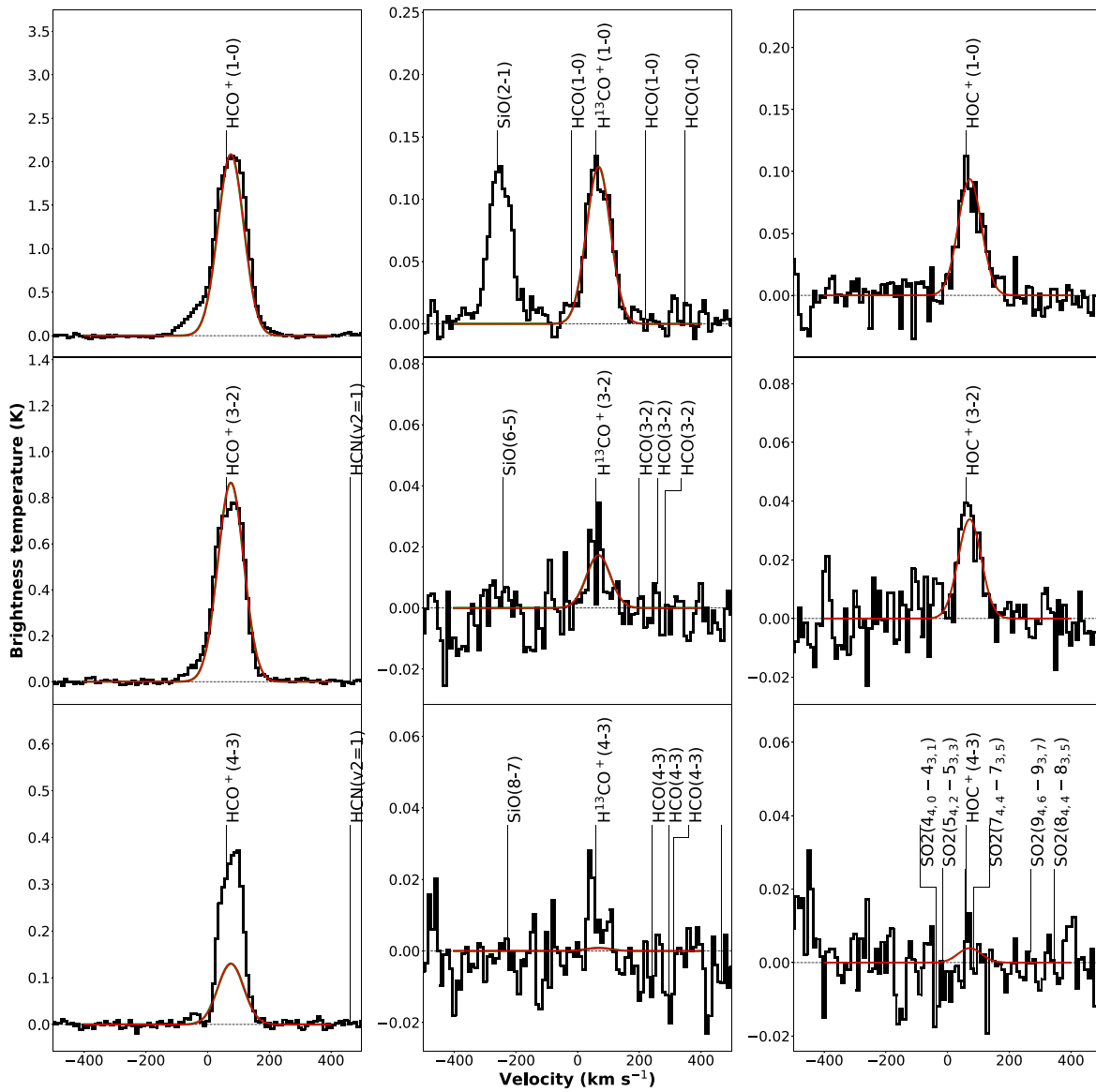
Figure 26. Spectra at position A3.
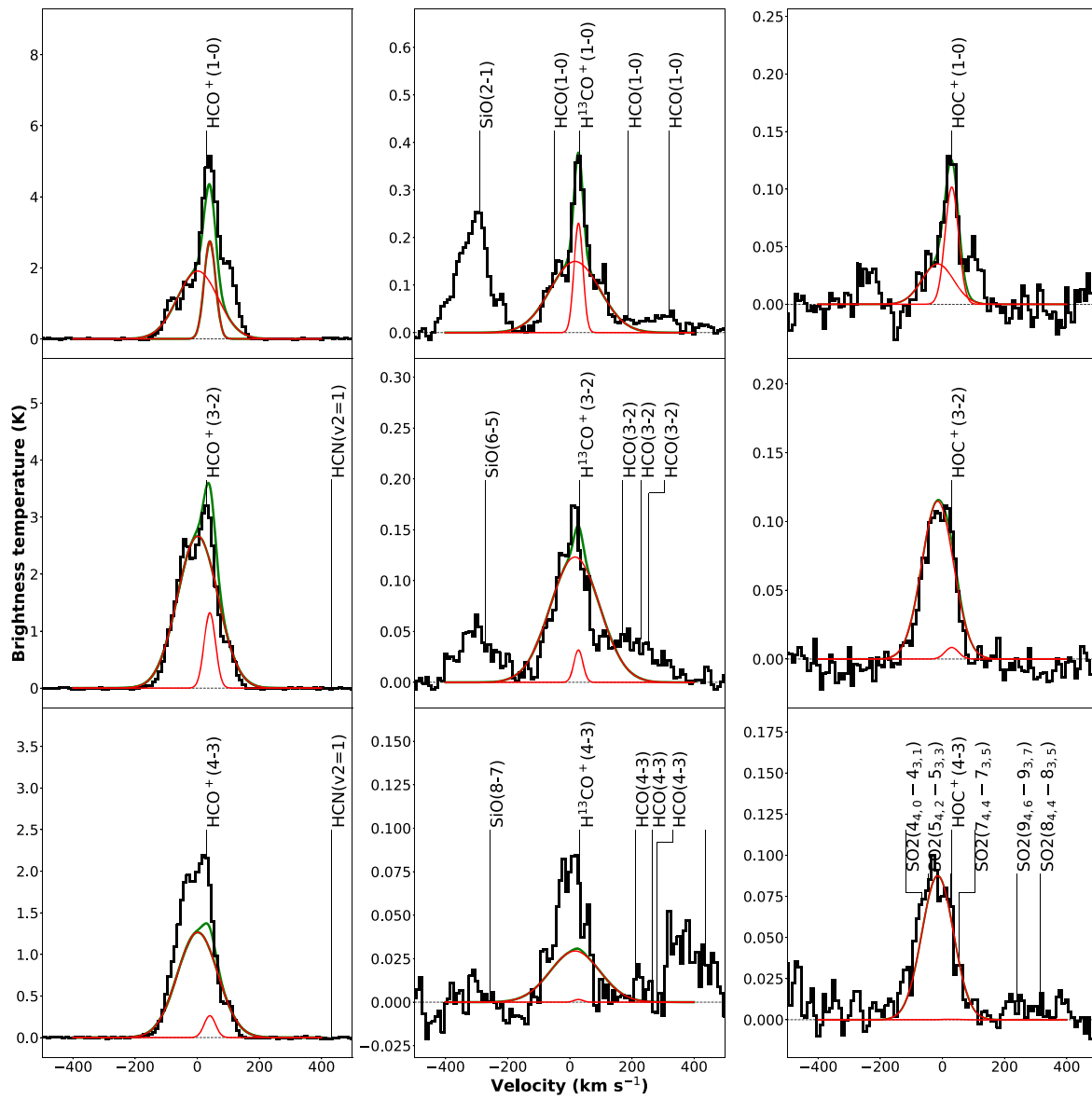
Figure 27. Spectra at position A4.

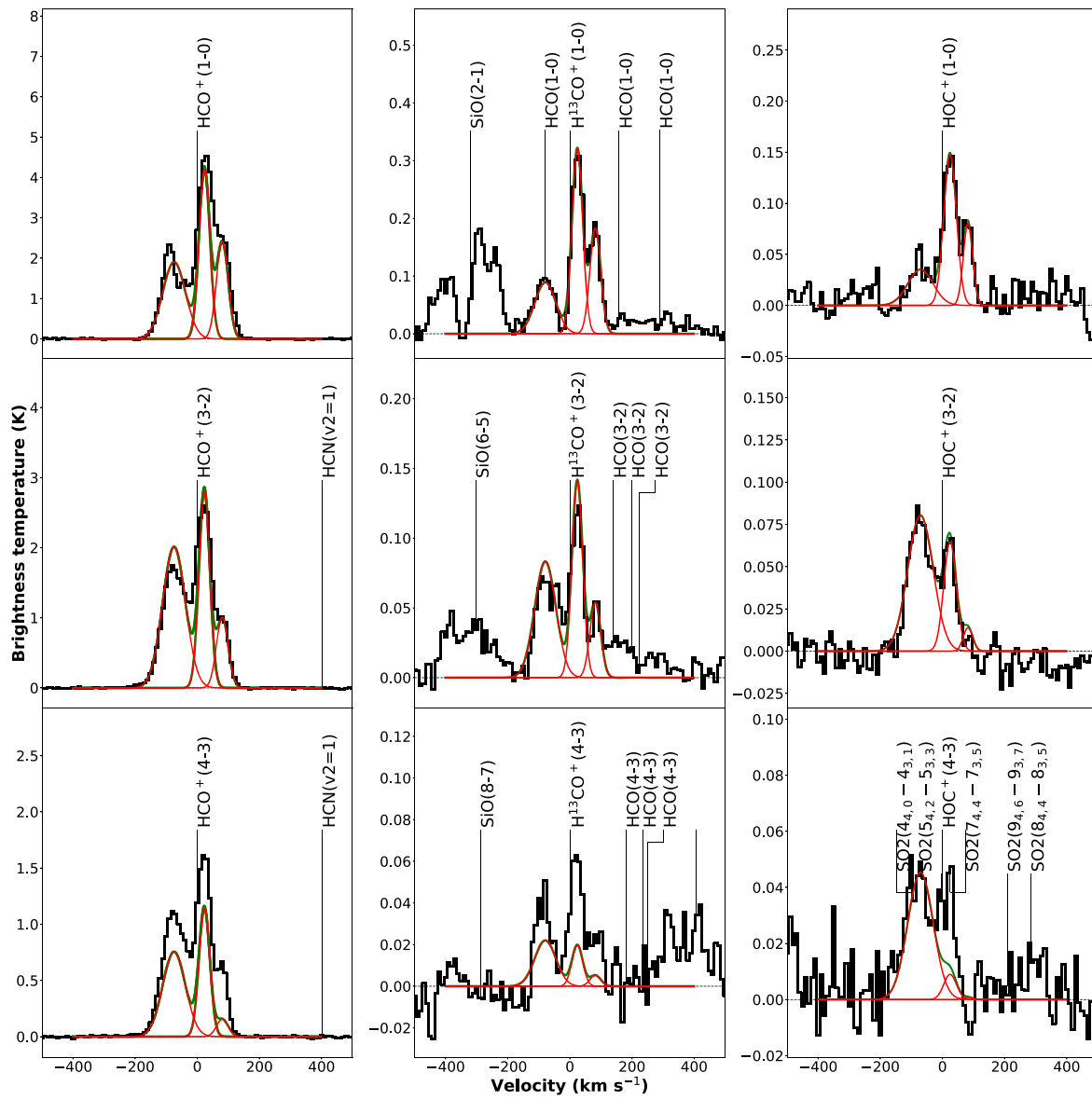**Figure 28.** Spectra at position A5.
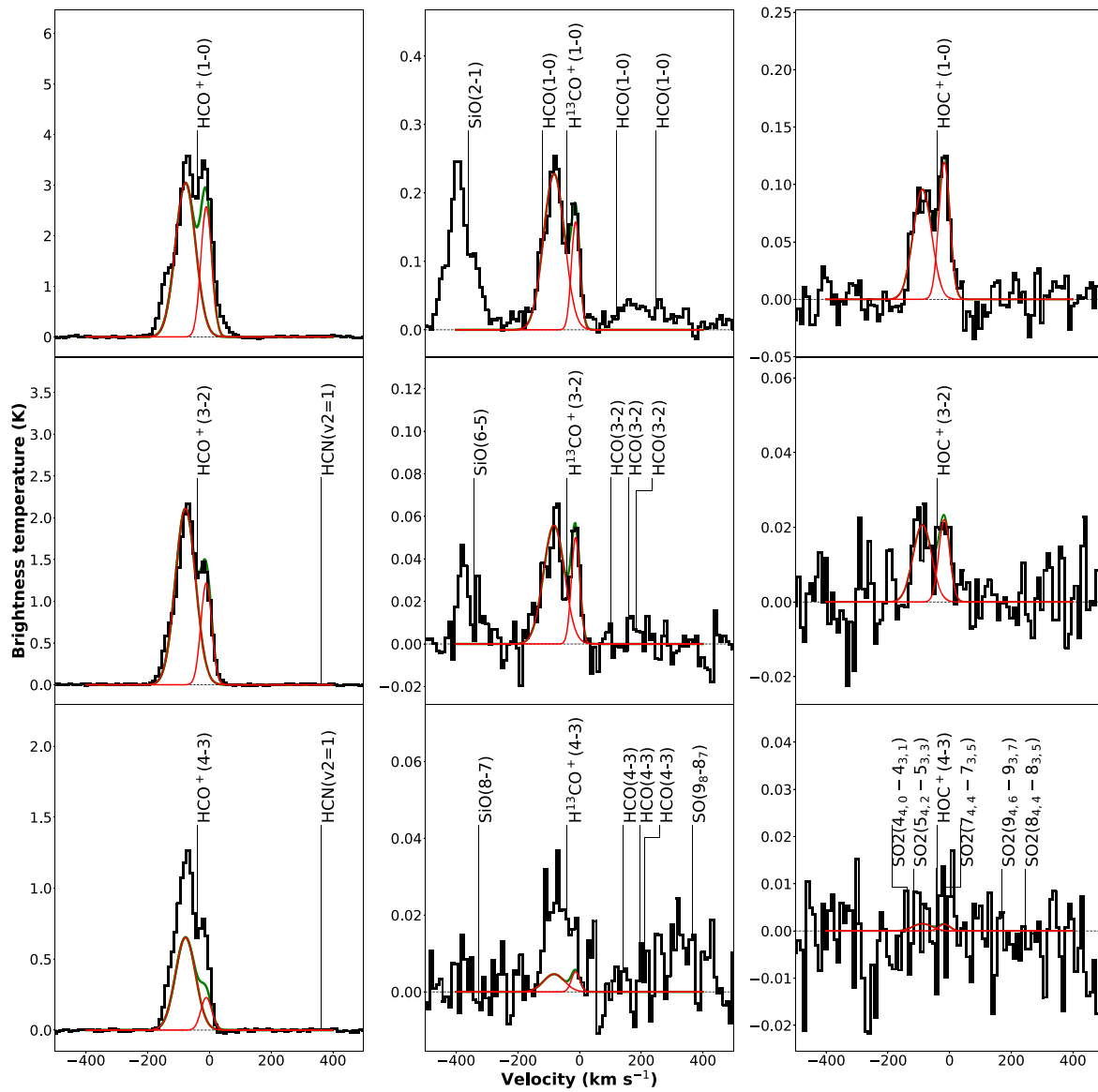
Figure 29. Spectra at position A6.

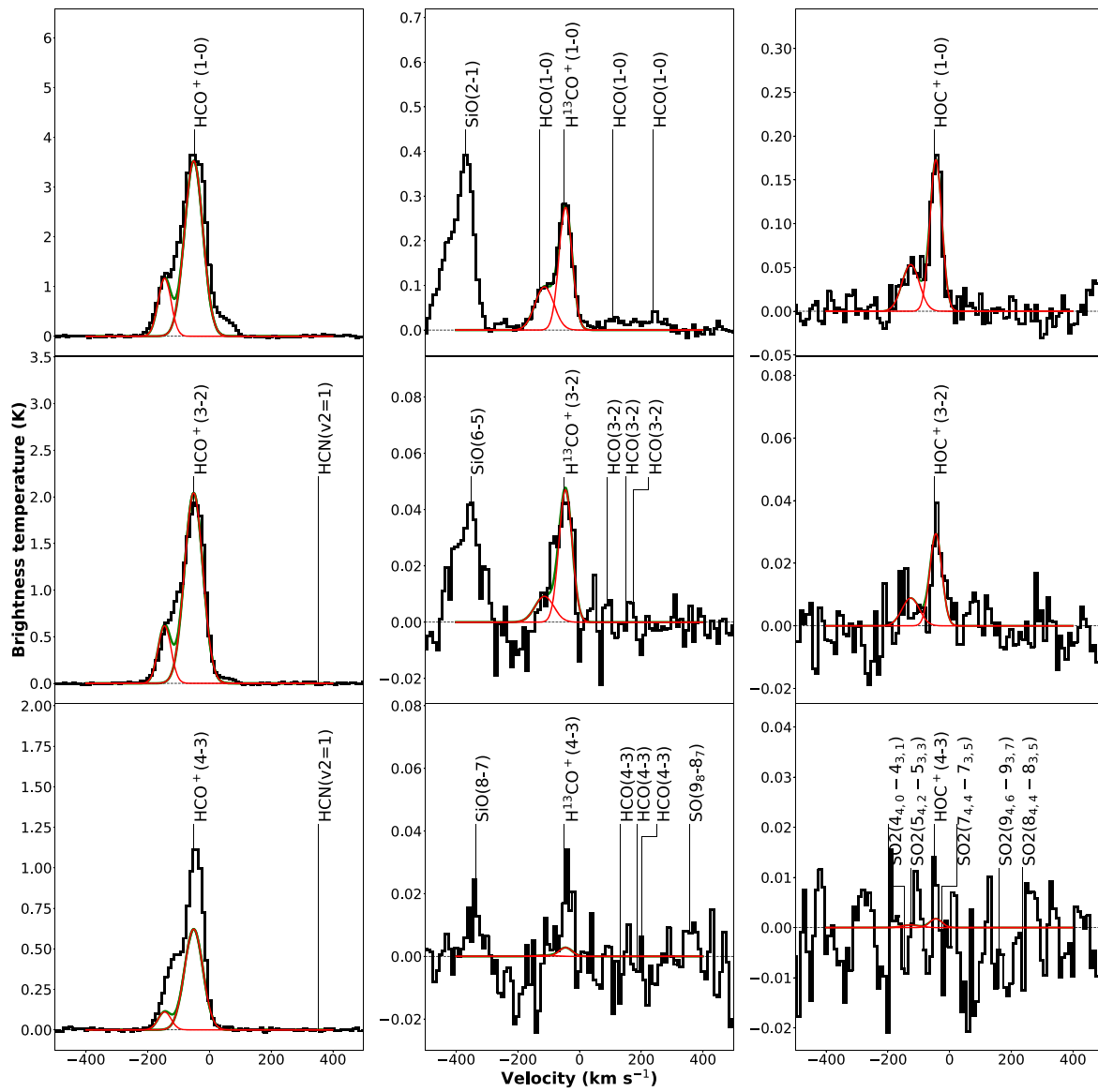**Figure 30.** Spectra at position A7.

Figure 31. Spectra at position A8.

Appendix C
Details of Chemical Models

In this section we explain the detailed parameters used for our chemical models. As noted in Section 6, we ran the Meudon PDR code to obtain the gas and dust temperatures in the PDRs (Le Petit et al. 2006, http://ism.obspm.fr). We also assume $T_{gas} = 10$ K if the calculated temperature is below 10 K because most molecular clouds have higher temperatures than 10 K. We ran the Meudon code with the following parameters: $A_{V,max} = 5$, turbulent velocity $v = 10$ km s^{-1}, maximum and minimum dust sizes of 0.3 μm, and 3 nm with MRN distributions (Mathis et al. 1977). The current version of the Meudon code has several values of dust temperature corresponding to different dust number densities, which also translate to different dust sizes. We used the dust temperature when the dust number density is $n_{dust} = 1.1 \times 10^{-7}$ cm^{-3}.

With the temperature obtained with the Meudon code, we ran the time-dependent gas-grain code based on Nautilus. In this paper we show the results at $t = t_{dyn}$ where $t_{dyn} = 3 \times 10^7 / \sqrt{n/\mathrm{cm}^{-3}}$ yr. We note that species of interest in this paper did not have significant differences between the steady-state abundances and abundances at the dynamical time. We do not include reactions with vibrationally excited molecular hydrogen as its effect on the chemistry we analyzed seems limited in most cases (e.g., Agúndez et al. 2010).

C.1. PDR Models

Because the Meudon PDR code requires radiation on both sides, we set the radiation field of one side to be dominant, and we varied this radiation field strength to be $G_0 = 1$–10^5. For the back side of the plane-parallel slab, we set the radiation field to be negligibly small, with $G_0 = 10^{-3}$.

We modified the H$_2$ formation in the PDR region due to the high grain temperature. The original implementation of H$_2$ formation using the Lanmuir–Hinschelwood mechanism among physisorbed (weakly bound) atoms cannot form molecular hydrogen efficiently when the dust temperature is $\gtrsim$30 K. However, molecular hydrogen has been observed in PDR regions even with the dust temperatures

of 50 K or so. Alternative mechanisms have been proposed to form H$_2$ in warm dust temperatures, such as Eley–Rideal reactions with chemisorbed (strongly bound) atoms. Thi et al. (2020) included chemisorption and the diffusion of chemisorbed atoms for their formula of H$_2$ formation. Their results showed that the formation rate is similar to the standard values in the literature of $R = (1$–$3) \times 10^{-17}$ cm s^{-1} (Jura 1975) where R is the rate of H$_2$ formation, regardless of the dust temperature. Therefore, we used this rate without treating the rate with the Lanmuir–Hinschelwood mechanism among the physisorbed atoms.

C.2. CRDR Models

For CRDR models, we set the interstellar radiation field of the Meudon code to be $G_0 = 1$ and took the temperature at $A_V = 4$, where the effects of the radiation on the temperature become negligible. We note that the Meudon code encounters bistability at certain values of visual extinction ($A_V \sim 2$–3) with a relatively high cosmic-ray ionization rate of $\zeta \sim 10^{-15}$ s^{-1}. This bistability did not affect the parameter range we took results from.

Appendix D
Continuum Images

As described in Martín et al. (2021), the continuum images were obtained from STATCONT. Continuum images at three different frequencies 95, 224, and 362 GHz are shown in Figure 32. The emission in these continuum images is due to a combination of synchrotron, free–free, and dust emission. At 95 GHz, free–free emission is likely to be the dominant source of emission (Figure 5 of Martín et al. 2021), while dust should dominate at higher frequencies. Therefore, we use the 224 and 362 GHz continuum to calculate the H$_2$ column densities. We assume 95 GHz emission as an indicator of star formation in the discussion. However, to obtain the exact contribution from each emission mechanism requires the fit of many frequencies.

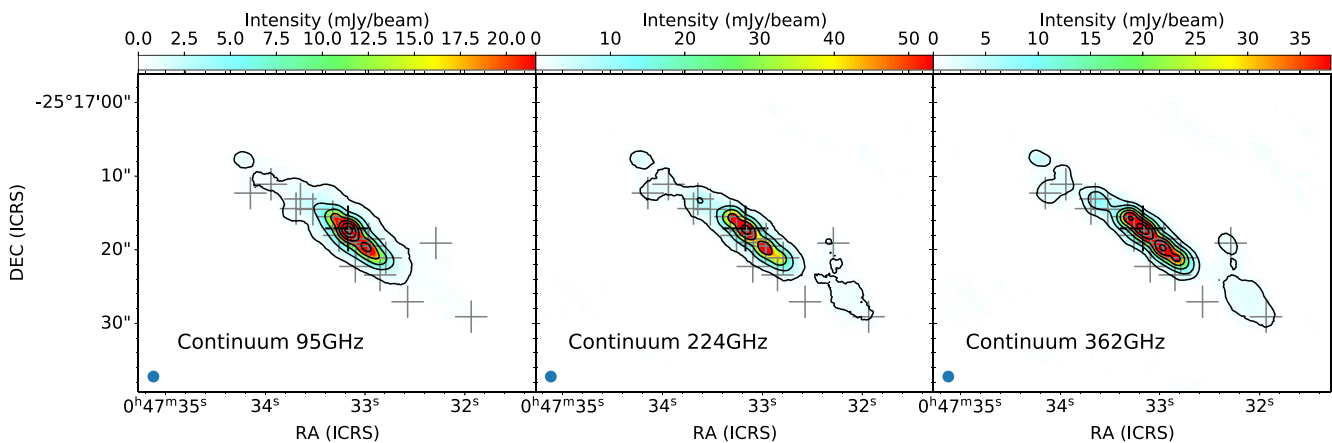**Figure 32.** Continuum images at (left) 95 GHz, (middle) 224 GHz, and (right) 362 GHz. These frequencies were chosen to select spectral windows with large numbers of continuum channels. Contour levels are $5\sigma n^{2.5}$ ($n = 1, 2, 3, 4, ...$) for 95 and 224 GHz, and $5\sigma n^2$ for 362 GHz images. The rms noise levels are 0.1, 0.3, and 1.5 mJy beam^{-1} for 95, 224, and 362 GHz, respectively.

Appendix E
Obtaining Total Hydrogen Column Densities

To obtain the total hydrogen column densities (N_{H2} or N_H), we used two different methods. One is from the dust continuum emission using the method proposed by Hildebrand (1983). Following the notation by Mangum et al. (2019), the molecular hydrogen column densities are estimated to be

$$N(H_2) = 7 \times 10^{22} R_{dg} \left(\frac{\lambda(mm)}{0.4}\right)^{\beta} \left(\frac{T_R}{T_d}\right) (cm^{-2}), \qquad (E2)$$

where R_{dg} is the dust-to-gas mass ratio, λ is the wavelength, β is the dust emissivity power law, T_R is the brightness temperature of the continuum flux, and T_d is the dust temperature. We used $R_{dg} = 150$, $\beta = 1.5$, and $T_d = 30$ K. The values for R_{dg} and β are taken from Mangum et al. (2019), while we use a slightly lower value for the dust temperature, 30 K, than that assumed by Mangum et al. (2019; 35 K). Column densities are calculated using the continuum images around 223 and 361 GHz that are relatively line-free. An alternative method for calculating N_{H_2} utilizes the $C^{18}O$ column densities assuming $CO/H_2 = 10^{-4}$ and $^{16}O/^{18}O = 150$ (Martín et al. 2009). To obtain the column densities of $C^{18}O$, we used a MADCUBA fit to the $C^{18}O$ emission within the ALCHEMI survey, which included the $J = 1$–0, 2−1, and 3−2 transitions. The values obtained from these two methods are consistent with each other in some cases, but not in other cases (see Table 8). The discrepancy can be as large as a factor of 4.

From our H_2 column densities derived from $C^{18}O$ column densities, continuum at 223 GHz, and continuum at 361 GHz, we used

$$\log_{10} N = \frac{1}{2} (\log_{10} N_{max} + \log_{10} N_{min}) \qquad (E3)$$

where N_{max}, N_{min} are maximum and minimum values of column densities among three values.

Table 8
Total Molecular Hydrogen Column Densities

Region	$N(H_2)$ (cont 223 GHz) $10^{22}(cm^{-2})$	$N(H_2)$ (cont 361 GHz) $10^{22}(cm^{-2})$	$N(H_2)$ ($C^{18}O$) $10^{22}(cm^{-2})$
M2	2.76	4.42	10.9
M3	3.74	5.18	7.47
M4	71.2	69.8	25.9
M5	139	109	29.1
M7	114	95.4	31.0
M8	17.6	21.5	18.1
M9	4.96	5.43	7.82
M10	5.29	6.53	8.84
A1	<1.85	< 1.72	4.96
A2	5.02	5.42	6.07
A3	57.6	50.3	17.8
A4	<1.85	<1.72	5.13
A5	73.8	53.2	17.5
A6	49.6	33.4	14.6
A7	12.9	12.0	13.2
A8	7.23	7.62	11.1

Note. The abundance ratio of $C^{18}O/H_2 = 150$ is used to obtain the estimate from $C^{18}O$.

ORCID iDs

Nanase Harada ⓘ https://orcid.org/0000-0002-6824-6627
Sergio Martín ⓘ https://orcid.org/0000-0001-9281-2919
Jeffrey G. Mangum ⓘ https://orcid.org/0000-0003-1183-9293
Kazushi Sakamoto ⓘ https://orcid.org/0000-0001-5187-2288
Sebastien Muller ⓘ https://orcid.org/0000-0002-9931-1313
Kunihiko Tanaka ⓘ https://orcid.org/0000-0001-8153-1986
Kouichiro Nakanishi ⓘ https://orcid.org/0000-0002-6939-0372
Yuki Yoshimura ⓘ https://orcid.org/0000-0002-1413-1963
Stefanie Mühle ⓘ https://orcid.org/0000-0002-4355-6485
Rebeca Aladro ⓘ https://orcid.org/0000-0002-1316-1343
Laura Colzi ⓘ https://orcid.org/0000-0001-8064-6394
Víctor M. Rivilla ⓘ https://orcid.org/0000-0002-2887-5859
Susanne Aalto ⓘ https://orcid.org/0000-0002-5828-7660
Erica Behrens ⓘ https://orcid.org/0000-0002-2333-5474
Christian Henkel ⓘ https://orcid.org/0000-0002-7495-4005
Jonathan Holdship ⓘ https://orcid.org/0000-0003-4025-1552
David S. Meier ⓘ https://orcid.org/0000-0001-9436-9471
Yuri Nishimura ⓘ https://orcid.org/0000-0003-0563-067X
Paul P. van der Werf ⓘ https://orcid.org/0000-0001-5434-5942
Serena Viti ⓘ https://orcid.org/0000-0001-8504-8844

References

Aalto, S., Garcia-Burillo, S., Muller, S., et al. 2015, A&A, 574, A85
Agúndez, M., Goicoechea, J. R., Cernicharo, J., Faure, A., & Roueff, E. 2010, ApJ, 713, 662
Aladro, R., König, S., Aalto, S., et al. 2018, A&A, 617, A20
Aladro, R., Martín, S., Riquelme, D., et al. 2015, A&A, 579, A101
Albertsson, T., Kauffmann, J., & Menten, K. M. 2018, ApJ, 868, 40
Ando, R., Nakanishi, K., Kohno, K., et al. 2017, ApJ, 849, 81
Apponi, A. J., & Ziurys, L. M. 1997, ApJ, 481, 800
Armijos-Abendaño, J., Martín-Pintado, J., López, E., et al. 2020, ApJ, 895, 57
Bayet, E., Williams, D. A., Hartquist, T. W., & Viti, S. 2011, MNRAS, 414, 1583
Bisbas, T. G., van Dishoeck, E. F., Papadopoulos, P. P., et al. 2017, ApJ, 839, 90
Bolatto, A. D., Warren, S. R., Leroy, A. K., et al. 2013, Natur, 499, 450
Bonfand, M., Belloche, A., Garrod, R. T., et al. 2019, A&A, 628, A27
Caselli, P. 2002, P&SS, 50, 1133
Ceccarelli, C., Hily-Blant, P., Montmerle, T., et al. 2011, ApJL, 740, L4
Colzi, L., Sipilä, O., Roueff, E., Caselli, P., & Fontani, F. 2020, A&A, 640, A51
Defrees, D. J., McLean, A. D., & Herbst, E. 1984, ApJ, 279, 322
Fernández-Ontiveros, J. A., Prieto, M. A., & Acosta-Pulido, J. A. 2009, MNRAS, 392, L16
Fluetsch, A., Maiolino, R., Carniani, S., et al. 2019, MNRAS, 483, 4586
Fuente, A., García-Burillo, S., Usero, A., et al. 2008, A&A, 492, 675
Fuente, A., Rodríguez-Franco, A., García-Burillo, S., Martín-Pintado, J., & Black, J. H. 2003, A&A, 406, 899
Glover, S. C. O., Federrath, C., Mac Low, M. M., & Klessen, R. S. 2010, MNRAS, 404, 2
Goicoechea, J. R., Cuadrado, S., Pety, J., et al. 2017, A&A, 601, L9
Goicoechea, J. R., Pety, J., Gerin, M., Hily-Blant, P., & Le Bourlot, J. 2009, A&A, 498, 771
Gong, M., Ostriker, E. C., & Wolfire, M. G. 2017, ApJ, 843, 38
Goto, M., Geballe, T. R., Indriolo, N., et al. 2014, ApJ, 786, 96
Harada, N., Riquelme, D., Viti, S., et al. 2015, A&A, 584, A102
Harada, N., Sakamoto, K., Martín, S., et al. 2018, ApJ, 855, 49
Harada, N., Sakamoto, K., Martín, S., et al. 2019, ApJ, 884, 100
Henkel, C., Mauersberger, R., & Schilke, P. 1988, A&A, 201, L23
Herbst, E., & Woon, D. E. 1996a, ApJL, 463, L113
Herbst, E., & Woon, D. E. 1996b, ApJL, 471, L73
Hersant, F., Wakelam, V., Dutrey, A., Guilloteau, S., & Herbst, E. 2009, A&A, 493, L49
Hildebrand, R. H. 1983, QJRAS, 24, 267
Holdship, J., Viti, S., Martín, S., et al. 2021, A&A, 654, 55
Hopkins, P. F., Quataert, E., & Murray, N. 2012, MNRAS, 421, 3522
Indriolo, N., Fields, B. D., & McCall, B. J. 2009, ApJ, 694, 257
Indriolo, N., & McCall, B. J. 2012, ApJ, 745, 91

Jarrold, M. F., Bowers, M. T., Defrees, D. J., McLean, A. D., & Herbst, E. 1986, ApJ, 303, 392
Jura, M. 1975, ApJ, 197, 575
Kim, C.-G., Ostriker, E. C., & Kim, W.-T. 2013, ApJ, 776, 1
Krieger, N., Bolatto, A. D., Leroy, A. K., et al. 2020, ApJ, 897, 176
Krieger, N., Bolatto, A. D., Walter, F., et al. 2019, ApJ, 881, 43
Krips, M., Martín, S., Sakamoto, K., et al. 2016, A&A, 592, L3
Le Petit, F., Nehmé, C., Le Bourlot, J., & Roueff, E. 2006, ApJS, 164, 506
Lepp, S., & Dalgarno, A. 1996, A&A, 306, L21
Lequeux, J. 2005, The Interstellar Medium (Berlin: Springer)
Leroy, A. K., Bolatto, A. D., Ostriker, E. C., et al. 2015, ApJ, 801, 25
Leroy, A. K., Bolatto, A. D., Ostriker, E. C., et al. 2018, ApJ, 869, 126
Levy, R. C., Bolatto, A. D., Leroy, A. K., et al. 2021, ApJ, 912, 4
Liszt, H., Lucas, R., & Black, J. H. 2004, A&A, 428, 117
Longmore, S. N., Bally, J., Testi, L., et al. 2013, MNRAS, 429, 987
Maloney, P. R., Hollenbach, D. J., & Tielens, A. G. G. M. 1996, ApJ, 466, 561
Mangum, J. G., Ginsburg, A. G., Henkel, C., et al. 2019, ApJ, 871, 170
Marconi, A., Testi, L., Natta, A., & Walmsley, C. M. 1998, A&A, 330, 696
Martín, S., Kohno, K., Izumi, T., et al. 2015, A&A, 573, A116
Martín, S., Martín-Pintado, J., Blanco-Sánchez, C., et al. 2019a, A&A, 631, A159
Martín, S., Martín-Pintado, J., & Viti, S. 2009, ApJ, 706, 1323
Martín, S., Mauersberger, R., Martín-Pintado, J., Henkel, C., & García-Burillo, S. 2006, ApJS, 164, 450
Martín, S., Muller, S., Henkel, C., et al. 2019b, A&A, 624, A125
Martín, S., Mangum, J. G., Harada, N., et al. 2021, A&A, in press
Mathis, J. S., Rumpl, W., & Nordsieck, K. H. 1977, ApJ, 217, 425
Mauersberger, R., & Henkel, C. 1991, A&A, 245, 457
McCall, B. J., Huneycutt, A. J., Saykally, R. J., et al. 2003, Natur, 422, 500
McMullin, J. P., Waters, B., Schiebel, D., Young, W., & Golap, K. 2007, in ASP Conf. Ser. 376, Astronomical Data Analysis Software and Systems XVI, ed. R. A. Shaw, F. Hill, & J. Bell (San Francisco, CA: ASP), 127
Meier, D. S., & Turner, J. L. 2005, ApJ, 618, 259
Meier, D. S., Walter, F., Bolatto, A. D., et al. 2015, ApJ, 801, 63
Meijerink, R., Spaans, M., & Israel, F. P. 2007, A&A, 461, 793
Morris, M., & Serabyn, E. 1996, ARA&A, 34, 645
Müller, H. S. P., Schlöder, F., Stutzki, J., & Winnewisser, G. 2005, JMoSt, 742, 215
Müller, H. S. P., Thorwirth, S., Roth, D. A., & Winnewisser, G. 2001, A&A, 370, L49
Muller, S., Beelen, A., Guélin, M., et al. 2011, A&A, 535, A103
Muller, S., Müller, H. S. P., Black, J. H., et al. 2016, A&A, 595, A128
Müller-Sánchez, F., González-Martín, O., Fernández-Ontiveros, J. A., Acosta-Pulido, J. A., & Prieto, M. A. 2010, ApJ, 716, 1166
Nakajima, T., Takano, S., Kohno, K., et al. 2015, PASJ, 67, 8
Neufeld, D. A., Goicoechea, J. R., Sonnentrucker, P., et al. 2010, A&A, 521, L10
Neufeld, D. A., & Wolfire, M. G. 2017, ApJ, 845, 163
Oka, T., Geballe, T. R., Goto, M., et al. 2019, ApJ, 883, 54
Padovani, M., Galli, D., & Glassgold, A. E. 2009, A&A, 501, 619
Rekola, R., Richer, M. G., McCall, M. L., et al. 2005, MNRAS, 361, 330
Rico-Villas, F., Martín-Pintado, J., González-Alfonso, E., Martín, S., & Rivilla, V. M. 2020, MNRAS, 491, 4573
Robitaille, T. 2019, APLpy v2.0: The Astronomical Plotting Library in Python, Zenodo, doi:10.5281/zenodo.2567476
Robitaille, T., & Bressert, E. 2012, APLpy: Astronomical Plotting Library in Python, Astrophysics Source Code Library, ascl:1208.017
Ruaud, M., Loison, J. C., Hickson, K. M., et al. 2015, MNRAS, 447, 4004
Sakamoto, K., Ho, P. T. P., Iono, D., et al. 2006, ApJ, 636, 685
Sakamoto, K., Mao, R.-Q., Matsushita, S., et al. 2011, ApJ, 735, 19
Sánchez-Monge, Á., Schilke, P., Ginsburg, A., Cesaroni, R., & Schmiedeke, A. 2018, A&A, 609, A101
Smith, M. A., Schlemmer, S., von Richthofen, J., & Gerlich, D. 2002, ApJL, 578, L87
Spaans, M., & Meijerink, R. 2007, ApJL, 664, L23
Strickland, D. K., Heckman, T. M., Weaver, K. A., & Dahlem, M. 2000, AJ, 120, 2965
Strickland, D. K., Heckman, T. M., Weaver, K. A., Hoopes, C. G., & Dahlem, M. 2002, ApJ, 568, 689
Takano, S., Nakajima, T., Kohno, K., et al. 2014, PASJ, 66, 75
Tang, X. D., Henkel, C., Menten, K. M., et al. 2019, A&A, 629, A6
Thi, W. F., Hocuk, S., Kamp, I., et al. 2020, A&A, 634, A42
Tielens, A. G. G. M., & Hollenbach, D. 1985, ApJ, 291, 722
Turner, B. E. 1985, ApJ, 299, 312
Turner, J. L., & Ho, P. T. P. 1985, ApJL, 299, L77
Ulvestad, J. S., & Antonucci, R. R. J. 1997, ApJ, 488, 621
Usero, A., García-Burillo, S., Fuente, A., Martín-Pintado, J., & Rodríguez-Fernández, N. J. 2004, A&A, 419, 897
van der Tak, F. F. S., & van Dishoeck, E. F. 2000, A&A, 358, L79
van der Tak, F. F. S., Weiß, A., Liu, L., & Güsten, R. 2016, A&A, 593, A43
Viti, S., Fontani, F., & Jiménez-Serra, I. 2020, MNRAS, 497, 4333
Viti, S., García-Burillo, S., Fuente, A., et al. 2014, A&A, 570, A28
Wakelam, V., Loison, J. C., Herbst, E., et al. 2015, ApJS, 217, 20
Walter, F., Bolatto, A. D., Leroy, A. K., et al. 2017, ApJ, 835, 265
Watson, A. M., Gallagher, J. S. I., Holtzman, J. A., et al. 1996, AJ, 112, 534
Westmoquette, M. S., Smith, L. J., & Gallagher, J. S. 2011, MNRAS, 414, 3719
Woon, D. E., & Herbst, E. 2009, ApJS, 185, 273